2017

# Novel Design and Synthesis of Nanostructured Electrode Materials for Advanced Lithium Ion Batteries

Zhiqiang Xie
*Louisiana State University and Agricultural and Mechanical College*

# NOVEL DESIGN AND SYNTHESIS OF NANOSTRUCTURED ELECTRODE MATERIALS FOR ADVANCED LITHIUM ION BATTERIES

A Thesis

Submitted to the Graduate Faculty of the
Louisiana State University and
Agricultural and Mechanical College
in partial fulfillment of the
requirements for the degree of
Master of Science

in

The Department of Mechanical & Industrial Engineering

By
Zhiqiang Xie
B.S., Kunming University of Science and Technology, 2011
M.S., University of Dayton, 2013
May 2017

## ACKNOWLEDGMENTS

I am grateful to my advisor, Prof. Ying Wang, whose consistent guidance, encouragement, advice and generous support made it possible for me to work on a research topic that was of great interest to me. It is a great opportunity for me to join her research group and work under her supervision and instruction. I also would like to sincerely thank Prof. Wenjin Meng, Prof. Dorel Moldovan and Prof. Leszek Czarnecki for being willing to serve on my master committee.

I am very thankful to my collaborators, Dr. Jianqing Zhao at Soochow University in China; Hilary Eikhuemelo, Wangwang Xu, Xiaodan Cui and Sarah Ellis at Louisiana State University (LSU); Ziyang He at Iowa State University; Zheng Liu at Nanyang Technological University; Xuhui Feng, Prof. Moises A Carreon at Colorado School of Mines; Chengmin Jiang, Prof. Angel A. Martí at Rice University; Jiuhong Zhang at Kent State University; Dr. Yujie Zhang, Prof. Aiguo Wu at Ningbo Institute of Industrial Technology, Chinese Academy of Sciences.

I would like to acknowledge all the financial support from Research Enhancement Award (REA) and the Research Awards Program (RAP) sponsored by LaSPACE, Graduate Student Travel Award (LSU), LSU Economic Development Assistantship, ECS Travel Grant Award from the Battery Division in The Electrochemical Society

Last but not least, I really appreciate my parents, old brother and young sister in China for their great support and love. I also would like to sincerely thank all my friends at LSU for their support and understanding in dealing with the challenges I have faced.

**TABLE OF CONTENTS**

## LIST OF TABLES

## LIST OF FIGURES

## LIST OF ABBREVIATIONS

| | |
|---|---|
| CV | Cyclic Voltammetry |
| EIS | Electrochemical impedance spectroscopy |
| EDS | Energy dispersive spectroscopy |
| FESEM | Field emission scanning electron microscopy |
| HRTEM | High-resolution transmission electron microscopy |
| LMNCO | $Li[Li_{0.2}Mn_{0.54}Ni_{0.13}Co_{0.13}]O_2$ |
| PVDF | Polyvinylidene fluoride |
| SAED | Select area electron diffraction |
| SEI | Solid-electrolyte interphase |
| SEM | Scanning electron microscope |
| TEM | Transmission electron microscopy |
| XPS | X-ray photoelectron spectroscopy |
| XRD | X-ray diffraction |

## ABSTRACT

Nowadays, rechargeable lithium-ion batteries (LIBs) have been widely used as energy storage devices for portable electronic devices. The increasing demand for their emerging applications in hybrid electric vehicles (HEVs) and electric vehicles (EVs) requires us to develop LIBs with higher energy density and power density. However, both the commercial cathode material ($LiCoO_2$) and anode material (graphite) exhibit low specific capacity and poor rate capability, which severely hinder the practical application of lithium-ion batteries for transportation. This thesis mainly includes four research works on novel design and synthesis of nanostructured electrode materials for advanced lithium-ion batteries. To improve the electrochemical performances of cathode materials $Li_4Mn_5O_{12}$, dual doping of Ni and Fe has been applied. It is found that the facile doping strategy can effectively improve both the operating voltage and reversible specific capacity of $Li_4Mn_5O_{12}$, demonstrating as a promising high-voltage cathode material for high-energy high-power LIBs. Li-rich transition metal oxides display very high theoretical capacity but suffer from poor cycling stability and rate capability due to its large initial capacity loss and inferior structural stability upon cycling. To solve these problems, we have designed and synthesized a L@S core–shell structure (Li-rich layered-spinel core–shell heterostructure) *via* evaporation-induced self-assembly (EISA) of ultrafine $Li_4Mn_{4.5}Ni_{0.5}O_{12}$ nanoparticles onto the surface of Li-rich layered $Li[Li_{0.2}Mn_{0.54}Ni_{0.13}Co_{0.13}]O_2$ (LMNCO), which demonstrates significantly improved specific capacity, cycling performance and rate capability for application as a cathode in new-generation LIBs compared to pristine LMNCO.

In addition to cathode materials, we have synthesized two types of high-performance anode materials for LIBs. A novel structure with Sn nanoparticles well-dispersed in the microspheres of manganese-nickel-cobalt carbonate $MNCCO_3$ ($Sn@MNCCO_3$) has been prepared by using a facile one-step solvothermal process. We also synthesized sandwich-like,

porous nitrogen-doped carbons by using zeolitic imidazolate framework (ZIF-8) as a template and carbon precursor.

# CHAPTER 1. INTRODUCTION

## 1.1 Background

Energy issues have become the top priority among a series of global issues for the next 50 years. Currently, fossil fuels are the dominant source to satisfy the energy needs of humanity, however, these resources are depleted fast and usually lead to some environmental problems, such as air pollution and global warming owing to the emissions of nitrous oxide, methane, carbon dioxide and other gases containing volatile organic compounds [1,2]. Therefore, much progress has been made to overcome the above-mentioned challenges by developing new energy technologies, including rechargeable batteries, fuel cells, supercapacitors and so forth. The ever-increasing market of electrical vehicles motivates the development of high-energy and high-power energy storage devices as new power sources [3-5].

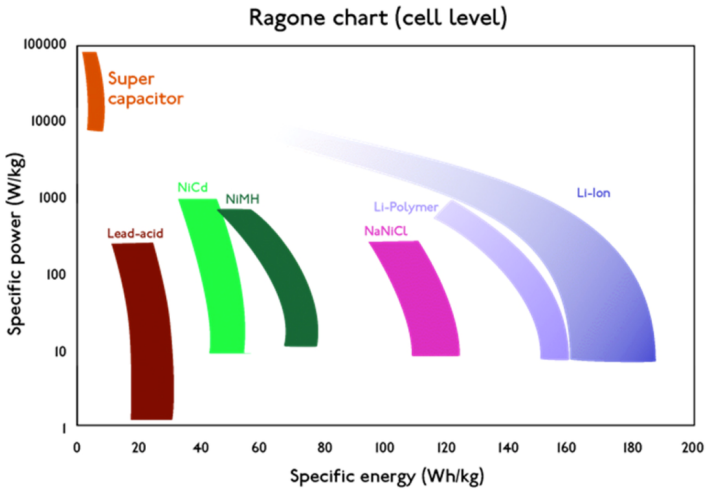


Figure 1.1 Ragone plot of electrochemical energy storage systems.[9]

In the past several decades, electrochemical energy storage/conversion systems have been used widely as power supplies for many portable electronic devices, hybrid electric vehicles (HEVs) or electric vehicles (EVs) [6-8]. The Ragone plot in Figure 1.1 shows various current electrochemical energy storage techniques, such as supercapacitors, lead-acid

batteries and lithium ion batteries [9]. Among them, lithium ion batteries exhibit relatively higher energy density and power density than the others. Nowadays, lithium ion batteries have become the popular power supply not only for various portable electronics, but also for electric vehicles, owing to their many advantages such as relatively high energy and high power density, environmental benignity, long lifetime, as well as no memory effects [10-12]. Currently, the commercial cathode materials in a lithium ion battery include $LiCoO_2$, $LiMn_2O_4$ and $LiFePO_4$. Figure 1.2 shows the crystal structures of these cathode mateirals with different $Li^+$ transport channels [13]. The main drawbacks of these commercial cathode materials are their low delivery capacity of ~100-170 mAh $g^{-1}$ and poor rate capability, which have hindered their application in plug-in hybrid electric vehicles (PHEV) or electric vehicles (EV).

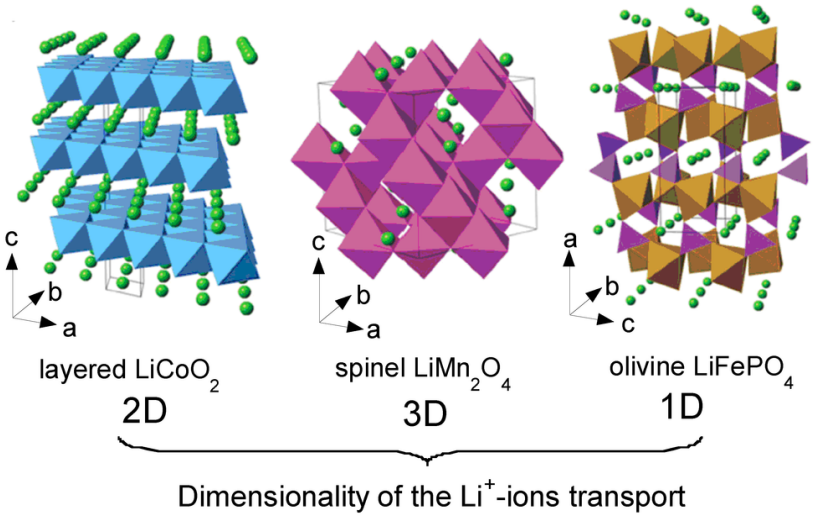


Figure 1.2 Crystal structures of three classes of cathode mateirals with different $Li^+$ transport channels.[13]

In LIBs, pioneering work used metallic lithium as anode for LIBs, due to its very high theoretical capacity of ~ 3840 mAh $g^{-1}$ and the lowest reduction potential (-3.04 V *vs.* S.H.E.) [14]. However, the growth of dendrites during the repeated battery charge/discharge

processes will lead to a short circuit within the LIBs, thereby resulting in some safety issues. Thus, graphite has replaced the metallic lithium as anode for commercial LIBs, due to its low cost and better safety, although it has a much lower theoretical capacity of 372 mAh $g^{-1}$. The graphite anode can store charges by an insertion mechanism, in which lithium ions are reversibly inserted into the layered graphite [15, 16]. However, the practical capacity and the cycle life of graphite anode are usually compromised due to an unavoidable blockage of insertion sites in the graphite. In this regard, various new anode materials with high theoretical capacities have been developed to improve the specific capacity, rate capability and cycling stability of LIBs, including silicon, tin, metal alloys, metal oxides and so forth [17-19].

**1.2 The Working Mechanism of Lithium-ion Battery**

Figure 1.3 shows the schematic illustration of a rechargeable lithium ion battery. As we can see that there are three main components in a lithium ion battery: cathode, anode and electrolyte. The cathode and anode are separated by an electronic insulator but $Li^+$ conducting electrolyte [20]. When the battery is powering an electronic, it undergoes the discharging process, in which the lithium ions are extracted out of the anode material (graphite) and inserted into the cathode material (cathode) and vice versa in the charging process. The energy density and power density of a lithium ion battery are mainly dependent on electrochemical properties of both cathode and anode materials [21].

Generally speaking, the electrode materials should possess the following characteristics to achieve the goal of high-energy and high-power lithium ion batteries: (*i*) a high theoretical capacity; (*ii*) an excellent electrical conductivity, which can ensure the fast charge transport within the electrodes and thus can enhance the rate capability of a lithium ion battery; (*iii*) a superior structural stability during repeated charge/discharge processes, which plays a key in role in cycling performance; (*iv*) highly reversible electrochemical

reactions at electrodes, which can maintain the specific capacity for long-term charge/discharge cycles; (*v*) a high cell voltage, which is determined by the standard redox potential of the cathode and anode during the respective electrode redox reactions.

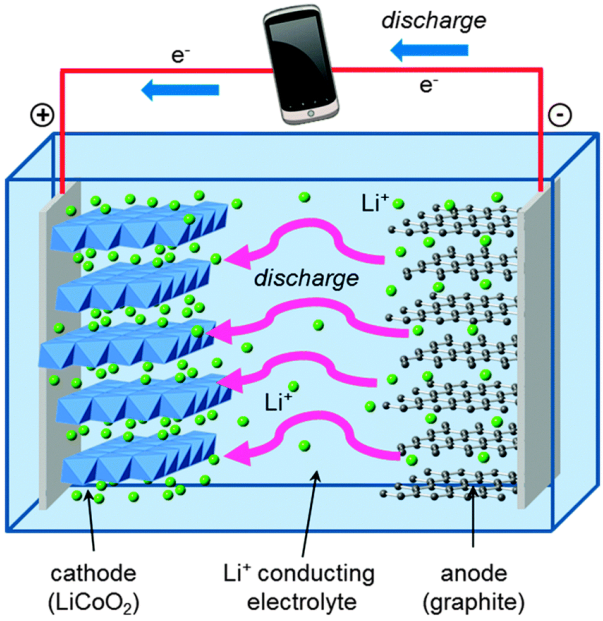


Figure 1.3 Schematic illustration of a lithium-ion battery in discharging process.[20]

Until now, the current electrode materials of lithium ion batteries still cannot satisfy all the above-mentioned requirements and thus suffer from unsatisfactory cycling stability and intrinsically poor rate capability [22-25]. Thus, it is highly desirable to develop high-performance cathode and anode materials with a high specific capacity, superior rate capability and excellent cycling stability over hundreds or even thousands of charge/discharge cycles.

### 1.3 Motivation and Goals

This master thesis mainly includes four projects on development of high-performance cathode and anode materials for advanced lithium ion batteries. In chapter 2, dual Fe and Ni doping of $Li_4Mn_5O_{12}$ cathode material is introduced. Spinel $Li_4Mn_5O_{12}$ has attracted great interest due to its high theoretical capacity of 163 mAh/g in the 3 V region, three dimensional

(3D) Li-ion transport pathway, and a good reversibility resulted from the stability of its crystal structure wherein all the manganese ions have a valence state of +4 [26]. However, the application of spinel $Li_4Mn_5O_{12}$ as promising cathode materials in high-energy high-power LIBs is hindered by its low working potential of ~3 V. To address this issue, the discharge plateau of $Li_4Mn_5O_{12}$ can be improved by partial substitution of Mn using other transition metal ions with high potential couples （$Cr^{3+/4+}$, $Co^{3+/4+}$, etc. Among various dopants, Ni and Fe can be promising dopants due to their high redox couple potentials (4.7 and 4.9 V, respectively)，low cost, abundant resource and environmental friendliness [27, 28]. Therefore, in this work, Ni and Fe dual-doped $Li_4Mn_{5-x-y}Ni_xFe_yO_{12}$ has been successfully prepared using a facile sol-gel method combined with post-heat treatment. As a result, it is found that the dual doping of Ni and Fe can effectively improve both the operating voltage and reversible specific capacity of $Li_4Mn_5O_{12}$, demonstrating as a promising high-voltage cathode material for high-energy high-power LIBs.

Chapter 3 presents the preparation of core-shell structured cathode materials for high-performance lithium ion batteries. Nowadays, $Li[Li_{0.2}Mn_{0.54}Ni_{0.13}Co_{0.13}]O_2$, as one of the Li-rich cathode materials, has attracted extensive attention due to its extremely high theoretical capacity of 321 mA h $g^{-1}$, better cycling stability and rate capability than other Li-rich analogs [29]. Unfortunately, these materials still suffer from unsatisfactory cycling stability and intrinsically poor rate capability. Moreover, it has been reported that Li-rich layered oxides suffer from surface vulnerability at high voltage and erosion from electrolytes [30]. In order to address these challenges, we have developed a simple and facile one-pot preparation of L@S core–shell structure (Li-rich layered-spinel core–shell heterostructure) *via* evaporation-induced self-assembly (EISA) of ultrafine $Li_4Mn_{4.5}Ni_{0.5}O_{12}$ nanoparticles onto the surface of Li-rich layered $Li[Li_{0.2}Mn_{0.54}Ni_{0.13}Co_{0.13}]O_2$ (LMNCO) without using any surfactant during the coating process. As a result, the as-prepared L@S core–shell material

demonstrates significantly improved specific capacity, cycling performance and rate capability for application as a cathode in new-generation LIBs compared to pristine LMNCO.

Chapter 4 focuses on development of a novel structure with Sn nanoparticles well-dispersed in the microspheres of manganese-nickel-cobalt carbonate $MNCCO_3$ ($Sn@MNCCO_3$) using a facile one-step solvothermal process. Tin (Sn) with high theoretical specific capacity has suffered from poor cycling stability due to its huge volume changes during charging/discharging processes [31]. Ternary manganese-nickel-cobalt carbonate displays a relatively better cycling stability but poor rate capability due to its low electrical conductivity. To combine the merits of Sn and carbonate, we have designed and synthesized $Sn@MNCCO_3$ composites. It is expected that the well-dispersed Sn nanoparticles will enhance the electronic conductivity of the overall electrode, while $MNCCO_3$ serves as a matrix to buffer against the huge volume changes of Sn nanoparticles in the composite. Sn content has been optimized for maximized battery performance. It is found that $Sn@MNCCO_3$ composite with 10 wt% of Sn shows a highly reversible specific capacity, excellent cycling stability and significantly improved rate capability profiting from the synergic effect of the components in the composite.

Chapter 5 introduces sandwich-like, porous nitrogen-doped carbons as new anode materials for lithium ion batteries. Although various new carbon-based anode materials have been developed in recent years, most carbonaceous materials have low electrical conductivity and poor structural stability when cycled at high charge/discharge rates as well as limited active sites for effective Li-ion storage [32-35]. Therefore, the lithium storage capability and rate performance of carbonaceous anodes still need further improvement. In this project, zeolitic imidazolate framework (ZIF-8) has been selected as a suitable carbon precursor to yield in situ N-doped porous carbon due to its high N content, large porosity and high specific surface area. The resultant carbons have been evaluated as anode material in lithium

ion batteries, exhibiting remarkable capacities, outstanding rate capability, and cycling performances that are some of the best results among carbonaceous electrode materials.

### 1.4 References


1. M. Z. Jacobson, Review of solutions to global warming, air pollution, and energy security. Energy Environ. Sci. 2009, 2, 148-173.

2. Z. Q. Xie, W. W. Xu, X. D. Cui, Y. Wang, Recent progress in metal–organic frameworks and their derived nanostructures for energy and environmental applications, ChemSusChem, 2017, DOI: 10.1002/cssc.201601855.

3. M. M. Thackeray, C. Wolverton, E. D. Isaacs, Electrical energy storage for transportation—approaching the limits of, and going beyond, lithium-ion batteries. Energy Environ. Sci, 2012, 5, 7854-7863.

4. V. Etacheri, R. Marom, R. Elazari, G. Salitra, D. Aurbach, Challenges in the development of advanced Li-ion batteries: a review. Energy Environ. Sci, 2011, 4, 3243-3262.

5. T. H. Kim, J. S. Park, S. K. Chang, S. Choi, J. H. Ryu, H. K. Song, The current move of lithium ion batteries towards the next phase. Adv. Energy Mater, 2012, 2, 860-872.

6. N. A. Kaskhedikar, J. Maier, Lithium storage in carbon nanostructures. Adv. Mater. 2009, 21, 2664-2680.

7. S. Chu, A. Majumdar, Opportunities and challenges for a sustainable energy future. Nature, 2012, 488, 294−303.

8. W. W. Xu, Z. Q. Xie, Z. Wang, G. Dietrich, Y. Wang, Interwoven heterostructural $Co_3O_4$–carbon@FeOOH hollow polyhedrons with improved electrochemical performance. J. Mater. Chem. A, 2016, 4, 19011-19018.

9. N. Omar, M. Daowd, O. Hegazy, G. Mulder, J.M., Coosemans, T. Timmermans, P. Van den Bossche, J. Van Mierlo, Standardization work for BEV and HEV applications: critical appraisal of recent traction battery documents. Energies, 2012, 5, 138-156.

10. B. Wang, X. L Li, X. F. Zhang, B. Luo, M. H. Jin, M. H. Liang, Shadi A. Dayeh, S. T. Picraux, L. J. Zhi, Adaptable silicon–carbon nanocables sandwiched between reduced graphene oxide sheets as lithium ion battery anodes. ACS Nano, 2013, 7, 1437-1445.

11. C. N. He, S. Wu, N. Q. Zhao, C. S. Shi, E. Z. Liu, J. J. Li, Carbon-encapsulated $Fe_3O_4$ nanoparticles as a high-rate lithium ion battery anode material. ACS Nano, 2013, 7, 4459-4469.

12. M. Winter, J. O. Besenhard, Electrochemical lithiation of tin and tin-based intermetallics and composites. Electrochim. Acta, 1999, 45, 31-50.

13. C. M. Julien, A. Mauger, K. Zaghib, H. Groult, Comparative issues of cathode materials for Li-ion batteries. Inorganics, 2014, 2, 132-154.

14. A. C. Kozen, C. F. Lin, A. J. Pearse, M. A. Schroeder, X. G. Han, L. B. Hu, S. B. Lee, G. W. Rubloff, M. Noked, Next-generation lithium metal anode engineering via atomic layer deposition. ACS Nano, 2015, 9, 5884 -5892.

15. Y. Wang, G. Z. Cao, Next-generation lithium metal anode engineering via atomic layer deposition. Adv. Mater., 2008, 20, 2251-2269.

16. Y. Wang, G. Z. Cao, Synthesis and enhanced intercalation properties of nanostructured vanadium oxides. Chem. Mater., 2006, 18, 2787-2804.

17. X. X. Zuo, J. Zhu, P. M. Buschbaum, Y. J. Cheng, Silicon based lithium-ion battery anodes: a chronicle perspective review, Nano Energy 2017, 31, 113-143.

18. S. Goriparti, E. Miele, F. D. Angelis, E. D. Fabrizio, R. P. Zaccaria, C. Capiglia. Review on recent progress of nanostructured anode materials for Li-ion batteries." J. Power Sources 2014, 257, 421-443.

19. Y. Wang, M. Wu, Z. Jiao, J. Y. Lee, Sn@CNT and Sn@C@CNT nanostructures for superior reversible lithium ion storage. Chem. Mat., 2009, 21, 3210-3215.

20. M. S. Islam, C. A. J. Fisher, Lithium and sodium battery cathode materials: computational insights into voltage, diffusion and nanostructural properties. Chem. Soc. Rev., 2014, 43, 185-204.

21. L. Wang, Y. Han, X. Feng, J. Zhou, P. Qi, B. Wang, Metal–organic frameworks for energy storage: Batteries and supercapacitors. Coord. Chem. Rev. 2016, 307, 361-381.

22. A. R. Kamali, D. J. Fray, Tin-based materials as advanced anode materials for lithium ion batteries: a review. Rev. Adv. Mater.Sci., 2011, 27, 14-24.

23. J. S. Chen, X. W. Lou, $SnO_2$ and $TiO_2$ nanosheets for lithium-ion batteries. Mater. Today, 2012, 15, 246-254.

24. M. Gu, A. Genc, I. Belharouak, D. Wang, K. Amine, S. Thevuthasan, D. R. Baer, J. G. Zhang, N. D. Browning, J. Liu, C. Wang, Nanoscale phase separation, cation ordering, and surface chemistry in pristine $Li_{1.2}Ni_{0.2}Mn_{0.6}O_2$ for Li-ion batteries. Chem. Mater., 2013, 25, 2319-2326.

25. A. R. Armstrong, M. Holzapfel, P. Novak, C. S. Johnson, S. H. Kang, M. M. Thackeray, P. G. Bruce, Demonstrating oxygen loss and associated structural reorganization in the lithium battery cathode $Li[Ni_{0.2}Li_{0.2}Mn_{0.6}]O_2$. J. Am. Chem. Soc., 2006, 128, 8694-8698.

26. Y. Fu, H. Jiang, Y. Hu, L. Zhang, C. Li, Hierarchical porous $Li_4Mn_5O_{12}$ nano/micro structure as superior cathode materials for Li-ion batteries. J. Power Sources, 2014, 261, 306-310.

27. M. A. Kebede, N. Kunjuzwa, C. J. Jafta, M. K. Mathe, K. I. Ozoemena, Solution-combustion synthesized nickel-substituted spinel cathode materials ($LiNi_xMn_{2-x}O_4$; $0 \leq x \leq 0.2$) for lithium ion battery: enhancing energy storage, capacity retention, and lithium ion transport. Electrochim. Acta, 2014, 128, 172-177.

28. B. Ebin, S. Gurmen, C. Arslan, G. Lindbergh, Electrochemical properties of nanocrystalline $LiFe_xMn_{2-x}O_4$ (x= 0.2–1.0) cathode particles prepared by ultrasonic spray pyrolysis method. Electrochim. Acta, 2012, 76, 368-374.

29. J. Q. Zhao, R. M. Huang, W. P. Gao, J. M. Zuo, X. F. Zhang, S. T. Misture, Y. Chen, J. Lockard, B. L. Zhang, S. M. Guo, M. R. Khoshi, K. Dooley, H. X. He, Y. Wang, Ion-exchange promoted phase transition in Li-excess layered cathode material for high-performance lithium ion batteries", Adv. Energy Mater., 2015, 1401937.

30. D. Wang, I. Belharouak, G. Zhou, K. Amine, Nanoarchitecture multi-structural cathode materials for high capacity lithium batteries. Adv. Funct. Mater., 2012, 23, 1070-1075.
31. Y. Wang, J. Y. Lee, T. C. Deivaraj, Tin nanoparticle loaded graphite anodes for Li-ion battery applications. J. Electrochem. Soc., 2004, 151, 1804-1809.

32. K. T. Lee, J. C. Lytle, N. S. Ergang, S. M. Oh, A. Stein, Synthesis and rate performance of monolithic macroporous carbon electrodes for lithium-ion secondary batteries. Adv. Funct. Mater. 2005, 15, 547-556.

33. F. D. Han, Y. J. Bai, R. Liu, B. Yao, Y. X. Qi, N. J. Lun, X. Zhang, Template-free synthesis of interconnected hollow carbon nanospheres for high-performance anode material in lithium-ion batteries. Adv. Energy Mater. 2011, 1, 798-801.

34. Li, C.; Yin, X.; Chen, L.; Li, Q.; Wang, T. Porous Carbon Nanofibers Derived from Conducting Polymer: Synthesis and Application in Lithium-Ion Batteries with High-Rate Capability. J. Phys. Chem. C. 2009, 113, 13438-13442.

35. H. Wang, T. Abe, S. Maruyama, Y. Iriyama, Z. Ogumi, K. Yoshikawa, Graphitized carbon nanobeads with an onion texture as a lithium-ion battery negative electrode for high-rate use. Adv. Mater. 2005, 17, 2857-2860.

# CHAPTER 2. NI AND FE DUAL-DOPED $Li_4Mn_5O_{12}$ SPINELS AS CATHODE MATERIALS FOR HIGH-VOLTAGE LI-ION BATTERIES [*]

## 2.1 Introduction

Nowadays, extensive research efforts have been focused on the application of Lithium ion batteries (LIBs) on plug-in hybrid electric vehicles (PHEV) or electric vehicles (EV) [1-3], which require higher operating voltage, higher energy density, longer cycle life, high safety and low cost [4-5]. In this regard, lithium manganese oxides (LMO) as promising cathode materials for LIBs have been widely studied over the past decade [6-12]. Among this family, the 4V spinel $LiMn_2O_4$ has drawn wide attention due to its high operating voltage and good rate capability resulted from its 3D lithium ion diffusion in the spinel lattice [13,14], but one of the major drawbacks is that $LiMn_2O_4$ suffers from fast capacity fading during cycling due to the manganese dissolution through a disproportionation reaction ($Mn^{3+} \rightarrow Mn^{2+} + Mn^{4+}$) and structural change caused by the Jahn-Teller distortion of $Mn^{3+}$ [15-18]. Recent studies have shown that these limitations can be restrained by increasing the average valence of Mn in $LiMn_2O_4$ via doping some transition metal ions, such as Ni [19-21], Co [22], Fe [23], Cr [24], Mg [25] Zn [26] etc. Among its variants, $LiMn_{1.5}Ni_{0.5}O_4$ has been widely reported to have a high operating voltage (~4.7 V) and improved cycling performance due to the presence of all Mn as $Mn^{4+}$ and Ni as $Ni^{2+}$ [27, 28]. However, electrochemical performance of $LiMn_{1.5}Ni_{0.5}O_4$ is still unsatisfactory due to the formation of $Li_xNi_{1-x}O$ impurity phase [29] and three cubic phases with large lattice parameter difference during charging/discharge process [30].

[*] This chapter previously appeared as Zhiqiang Xie, Hilary Eikhuemelo, Jianqing Zhao, Carrington Cain, Wangwang Xu and Ying Wang, "Ni and Fe dual doped $Li_4Mn_5O_{12}$ spinels as cathode materials for high-voltage Li-ion batteries", Journal of The Electrochemical Society, 2015, 162, A1523-A1529. It is reprinted by permission of ECS-The Electrochemical Society.

Recently, spinel $Li_4Mn_5O_{12}$ has attracted great interest due to its high theoretical capacity of 163 mAh/g in the 3 V region, three dimensional (3D) Li-ion transport pathway, and a good reversibility resulted from the stability of its crystal structure wherein all the manganese ions have a valence state of +4 [31,32]. Recently, Fu et al. reported that porous $Li_4Mn_5O_{12}$ nano/micro structure demonstrated a high specific capacity of 161 mAh/g in the 3 V region with excellent cycling stability and good rate capability [31]. However, the application of spinel $Li_4Mn_5O_{12}$ as promising cathode materials in high-energy high-power LIBs is hindered by its low working potential of ~3 V. To address this issue, the discharge plateau of $Li_4Mn_5O_{12}$ can be improved by partial substitution of Mn using other transition metal ions with high potential couples （$Cr^{3+/4+}$, $Co^{3+/4+}$, etc）. Among various dopants, Ni and Fe can be promising dopants due to their high redox couple potentials (4.7 and 4.9 V, respectively) [33,34], low cost, abundant resource and environmental friendliness. Therefore, in this work, Ni and Fe dual-doped $Li_4Mn_{5-x-y}Ni_xFe_yO_{12}$ has been successfully prepared using a facile sol-gel method combined with post-heat treatment. The effects of dual-cations doping on the crystal structure, morphology and electrochemical properties of the spinel cathode are investigated by XRD, SEM and galvanostatic charge/discharge analysis. As a result, $Li_4Mn_4Ni_{0.5}Fe_{0.5}O_{12}$ demonstrates the highest reversible specific capacity of 133 mAh/g at a specific current of 25 mA/g after 100 cycles and exhibits a high-voltage performance with a corresponding capacity of ~80 mAh/g at an average voltage of 4.7 V *vs*. $Li/Li^+$ and ~122 mAh/g at above 4.0 V, which is realized for the first time, to the best of our knowledge. These results indicate that the dual doping of Ni and Fe can effectively improve both the operating voltage and reversible specific capacity of $Li_4Mn_5O_{12}$, demonstrating as a promising high-voltage cathode material for high-energy high-power LIBs

## 2.2 Experimental Section

The pristine $Li_4Mn_5O_{12}$ and doped spinel $Li_4Mn_{5-x-y}Ni_xFe_yO_{12}$ samples (namely, $Li_4Mn_{4.5}Ni_{0.5}O_{12}$, $Li_4Mn_4NiO_{12}$, $Li_4Mn_{4.5}Ni_{0.25}Fe_{0.25}O_{12}$, $Li_4Mn_4Ni_{0.5}Fe_{0.5}O_{12}$ and $Li_4Mn_{3.75}Ni_{0.5}Fe_{0.75}O_{12}$) were synthesized via a facile sol-gel method combined with post-heat treatment. Briefly, 20 mmol stoichiometric manganese (II) acetate tetrahydrate, nickel (II) acetate tetrahydrate and Iron (III) nitrate nonahydrate with a molar ratio of $Mn^{2+}$: $Ni^{2+}$: $Fe^{3+}$ = 5-x-y: x: y were separately dissolved in 50 mL distilled water, and 16 mmol lithium hydroxide was dissolved in 15 mL distilled water. Afterwards, the transition metal precursor solution was added dropwise into the lithium precursor solution under continuous stirring. Subsequently, the mixed solution was aged in air at 40˚C until the solvent was completely evaporated. To improve the crystallinity of the collected powders, sintering was performed at 900˚C for 3 h using a heating/cooling rate of 1˚C/min. After the furnace was cooled down to room temperature, the as-prepared doped spinel powders were obtained. For comparison purpose, the pristine $Li_4Mn_5O_{12}$ was also synthesized by the same method without adding the doping materials.

The crystal structure of the obtained powders was investigated by x-ray diffraction (XRD) using a Rigaku MiniFlex X-ray diffractometer with Cu Kα radiation. XRD Data was collected in the range of $10^\circ \leq 2\theta \leq 80^\circ$ at a scan rate of $2^o$/min at room temperature. The Morphology and elemental analysis of the samples were observed using field emission scanning electron microscopy (FE-SEM) on a FEI Quanta 3D FEG FIB/SEM dual beam system, which is equipped with energy-dispersive X-ray spectroscopy (EDS).

Electrochemical properties of the synthesized $Li_4Mn_{5-x-y}Ni_xFe_yO_{12}$ ($0.5 \leq x+y \leq 1.25$) spinel cathode materials were evaluated using 2032-type coin cells. Typically, the cathodes were prepared by uniformly coating a homogeneous slurry of 80 wt % active material powders, 10 wt % acetylene black (conductive carbon, Alfa Aesar, 99.5%), and 10 wt %

polyvinylidene fluoride (PVDF, Alfa Aesar) binder in 1-methyl-3-pyrrolidone (NMP) solvent on aluminum foils and then dried in vacuum at 120˚C for 24 h. Coin cells were assembled in an argon-filled glove box. The electrolyte was 1 M $LiPF_6$ dissolved in ethylene carbonate (EG), dimethyl carbonate (DMC) and diethyl carbonate (DEC) at a volumetric ratio of 1:1:1. The electrochemical performance was tested at various C-rate regimes in the voltage range of 3.2-5.0 V by using an 8-channel battery analyzer (MTI Corporation). 1C rate was defined as 250 mAh/g. Cyclic voltammetric (CV) measurement was carried out on a CHI605C electrochemical analyzer at a scanning rate of 0.1 mV/s between 3.2 V and 5.0 V vs. $Li/Li^+$. All electrochemical measurements were performed at room temperature.

**2.3 Results and Discussion**

Figure 2.1 shows the powder XRD patterns of the as-prepared $Li_4Mn_5O_{12}$ and doped samples. The examination of diffraction patterns of all the samples confirms that all the strong peaks including (111), (311), (222), (400), (331), (511), (440), (531), (444) and (551) can be readily indexed to $Li_4Mn_5O_{12}$ with spinel phase of face-centered cubic structure (ICDD: 46-0810). These high-intensity peaks also suggest the highly crystalline nature of the as-synthesized pristine $Li_4Mn_5O_{12}$ and doped $Li_4Mn_{5-x-y}Ni_xFe_yO_{12}$ powders. However, it is found that several weak peaks (marked as * in Figure 2.1) are consistent with the layered $Li_2MnO_3$ phase with C2/m symmetry (ICDD: 84-1634), which might be ascribed to the decomposition of $Li_4Mn_5O_{12}$ spinel phase during post-heat treatment at 900°C. As reported in literature, this secondary layered phase contributes to a high capacity and meanwhile stabilizes the spinel phase when cycled in a broad voltage range [42, 43]. Detailed comparison of peak shift can be found in the selective patterns in the range of 18-19.5$^o$ and 35-50$^o$. Compared to pristine $Li_4Mn_5O_{12}$, the main (111), (311), (222) and (400) peaks obviously shift to higher angles in the single-element Ni-doping cases of $Li_4Mn_{4.5}Ni_{0.5}O_{12}$ and $Li_4Mn_4NiO_{12}$, while the diffraction peaks of (Ni, Fe)-doped $Li_4Mn_{4.5}Ni_{0.25}Fe_{0.25}O_{12}$,

$Li_4Mn_4Ni_{0.5}Fe_{0.5}O_{12}$ and $Li_4Mn_{3.75}Ni_{0.5}Fe_{0.75}O_{12}$ are found to shift back gradually with the increased Fe doping amount. As for $Li_4Mn_4Ni_{0.5}Fe_{0.5}O_{12}$, its diffraction peaks barely change in comparison with those of pristine sample, suggesting that appropriate doping amount of Fe can effectively counterbalance the Ni-doped spinel structure via further substituting Mn ions with larger sized Fe ions. However, it is observed that diffraction peaks from $Li_4Mn_4Ni_{0.5}Fe_{0.75}O_{12}$ start shifting towards the lower angles.

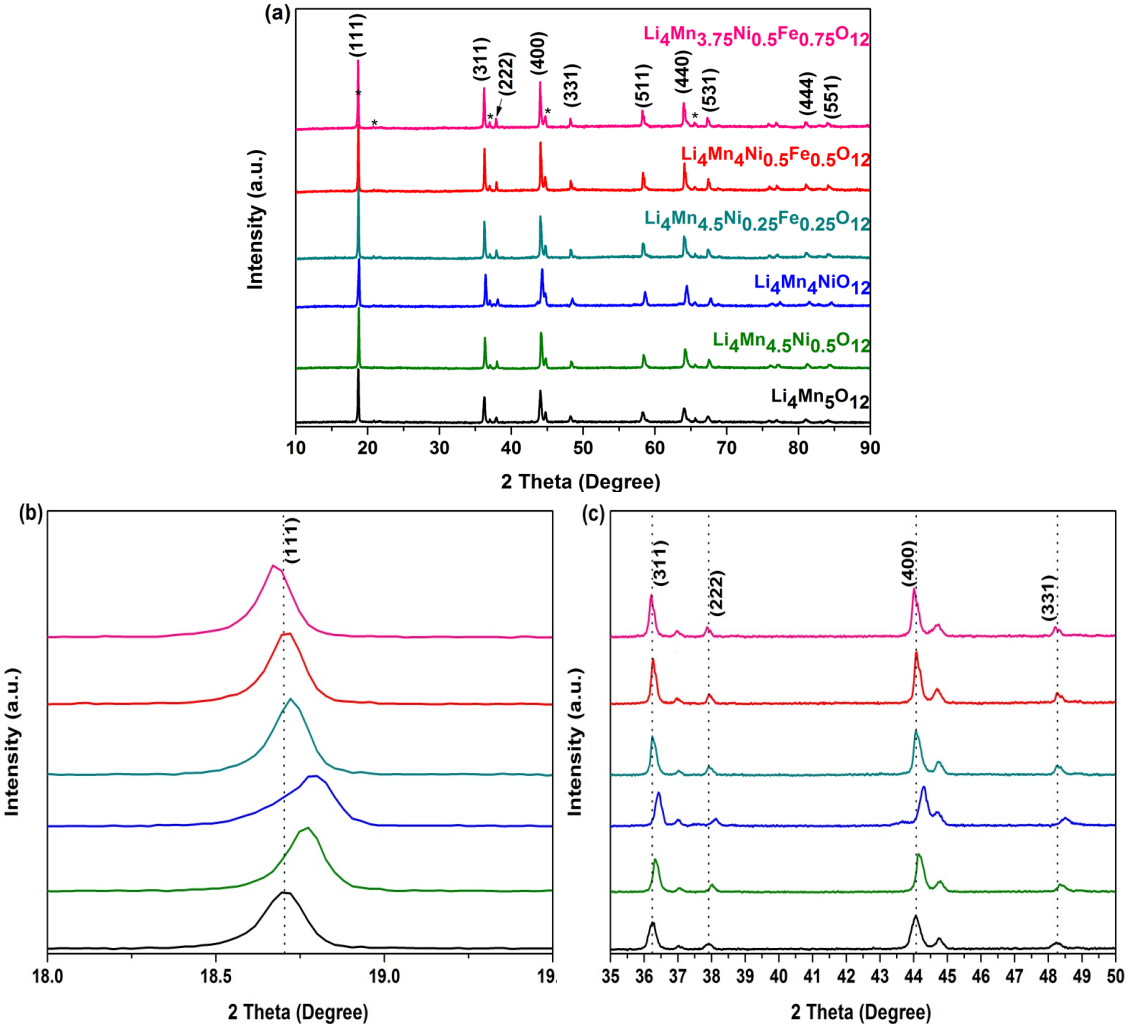


Figure 2.1 Powder XRD patterns of pristine $Li_4Mn_5O_{12}$ and doped $Li_4Mn_{5-x-y}$ $Ni_xFe_yO_{12}$ cathode materials with various doping amounts.

The variation in lattice parameter (a) and the corresponding unit cell volume (V) of the samples are calculated from the XRD data, as presented in Table 1. For pure $Li_4Mn_5O_{12}$, its lattice parameter and unit cell volume are a=8.2110 Å and V=553.602 $Å^3$. Regarding

single-element Ni-doped $Li_4Mn_{4.5}Ni_{0.5}O_{12}$ and $Li_4Mn_4NiO_{12}$, their lattice parameters decrease gradually with the increase in the amount of Ni from 0 to 1.0, revealing that their crystal structures are contracted with the substitution of Ni ion for Mn ion in Ni-doped $Li_4Mn_5O_{12}$, which may be ascribed to the shorter bond length of Mn(Ni)-O than that of Mn-O. Such phenomenon has also been reported for Ni-doped $LiMn_2O_4$ spinel cathode materials [33, 35, 36]. J. Shu et al. discovered that the shortening of Mn(Ni)-O bond length can increase the mean chemical bond energy, thereby improving the structural stability of $LiNi_{0.5}Mn_{1.5}O_4$ during electrochemical cycling [35]. Y. J. Wei et al. also confirmed that contraction of the crystal structure can stabilize the spinel structure during charge/discharge processes [36]. Therefore, single-element Ni-doped samples are expected to deliver a better cycling stability compared to bare $Li_4Mn_5O_{12}$. For Ni and Fe dual doped samples, their lattice parameters are slightly larger than single-element Ni-doped sample, which may be attributed to substitution of Mn ions with larger size of Fe ions. When the molar ratio of Fe is increased to 0.75, the calculated lattice parameter and unit cell volume indicate a slight volume expansion for $Li_4Mn_{3.75}Ni_{0.5}Fe_{0.75}O_{12}$. Therefore, doping of Ni is expected to improve cycling stability of $Li_4Mn_5O_{12}$ due to contraction of the crystal structure. In contrast, doping of Fe may lead to structural instability due to the slight volume expansion.

Table 2.1 Crystal structure parameters of pristine $Li_4Mn_5O_{12}$ and doped $Li_4Mn_{5-x-y}Ni_xFe_yO_{12}$ cathodes.

| Samples | $d_{111}$/Å | a/Å | Cell volume V/(Å$^3$) |
|---|---|---|---|
| $Li_4Mn_5O_{12}$ | 4.7408 | 8.2110 | 553.602 |
| $Li_4Mn_{4.5}Ni_{0.5}O_{12}$ | 4.7210 | 8.1768 | 546.695 |
| $Li_4Mn_4NiO_{12}$ | 4.7144 | 8.1653 | 544.400 |
| $Li_4Mn_{4.5}Ni_{0.25}Fe_{0.25}O_{12}$ | 4.7341 | 8.1994 | 551.255 |

| | | | |
|---|---|---|---|
| $Li_4Mn_4Ni_{0.5}Fe_{0.5}O_{12}$ | 4.7341 | 8.1994 | 551.255 |
| $Li_4Mn_{3.75}Ni_{0.5}Fe_{0.75}O_{12}$ | 4.7475 | 8.2227 | 555.960 |

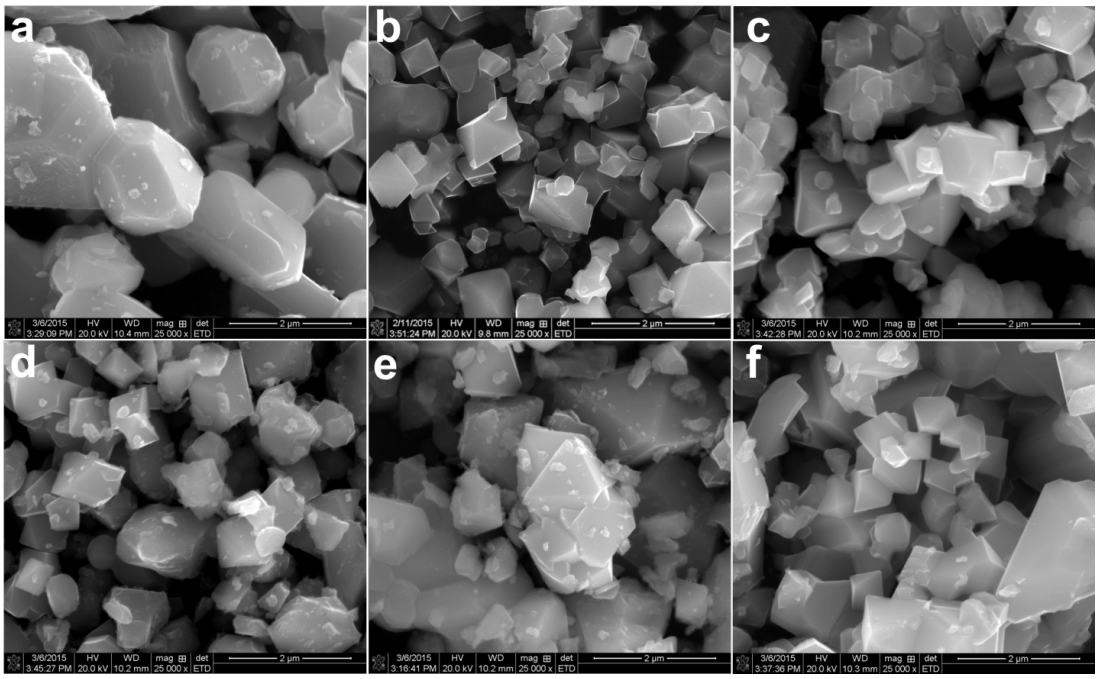


Figure 2.2 SEM images of (a) pristine $Li_4Mn_5O_{12}$, (b) $Li_4Mn_{4.5}Ni_{0.5}O_{12}$, (c) $Li_4Mn_4NiO_{12}$, (d) $Li_4Mn_{4.5}Ni_{0.25}Fe_{0.25}O_{12}$, (e) $Li_4Mn_4Ni_{0.5}Fe_{0.5}O_{12}$, and (f) $Li_4Mn_{3.75}Ni_{0.5}Fe_{0.75}O_{12}$ particles.

Figure 2.2 compares surface morphology and particle size of pristine $Li_4Mn_5O_{12}$ as well as Ni and Fe-doped samples. It can be seen that morphologies of these spinel powders become quite different after doping of Ni and Fe. The pristine $Li_4Mn_5O_{12}$ exhibits highly crystallized particles ranging from 2 to 5 um with smooth polyhedral facets. Compared to pristine $Li_4Mn_5O_{12}$, single-element doping of Ni apparently reduces the mean particle size of both $Li_4Mn_{4.5}Ni_{0.5}O_{12}$ and $Li_4Mn_4NiO_{12}$ powders into sub-micron scale. For all the (Ni, Fe)-doped samples, a unique nano/micro structure is observed as shown in Figure 2.2 d-f. The nano-sized particles tend to be embedded on the surface of the micro-sized, suggesting that doping of Fe can further reduce the particle size of the spinel into nano-scale.

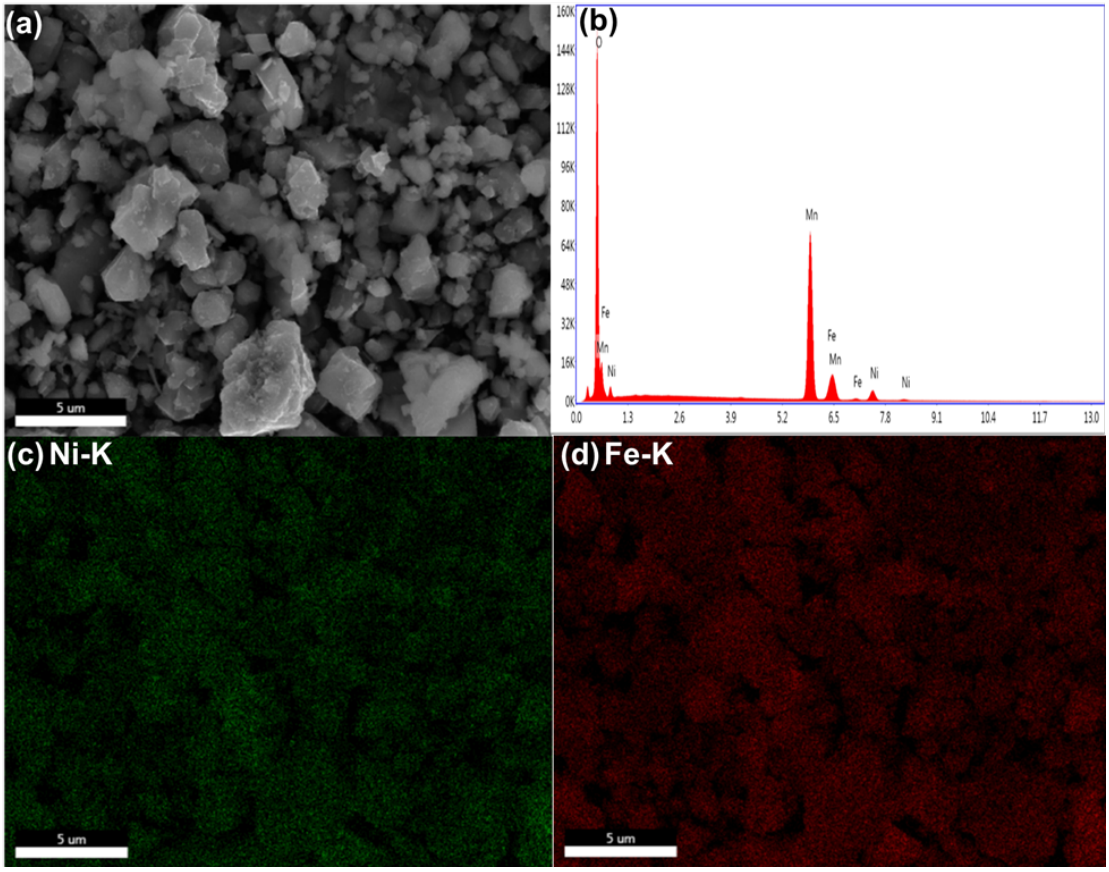


Figure 2.3 (a) SEM image of $Li_4Mn_4Ni_{0.5}Fe_{0.5}O_{12}$, (b) Energy-dispersive spectrum (EDS) of $Li_4Mn_4Ni_{0.5}Fe_{0.5}O_{12}$, (c) and (d) Elemental maps of Ni and Fe in $Li_4Mn_4Ni_{0.5}Fe_{0.5}O_{12}$, respectively.

EDS mapping analysis is also carried out to further identify Ni and Fe dopants in $Li_4Mn_4Ni_{0.5}Fe_{0.5}O_{12}$. Figure 2.3a shows the secondary electron microscope image of $Li_4Mn_4Ni_{0.5}Fe_{0.5}O_{12}$. The existence of Ni and Fe dopants is confirmed by EDS spectrum in Figure 2.3b. Moreover, as shown in the EDS mapping in Figure 2.3c-d with the green and red dots representing Ni and Fe element respectively, it is clear that Ni and Fe dopants are distributed homogeneously in the sample, suggesting the well-prepared dual-doped cathode material via a facile sol-gel method combined with post-heat treatment. In addition, as detected by SEM-EDS using spot analysis, Figure 2.4 shows a comparison of different small regions in an as-prepared $Li_4Mn_4Ni_{0.5}Fe_{0.5}O_{12}$ sample to investigate the possible

compositional changes between micro-sized particles and nanoparticles. As a result, the relative content of Mn: Ni: Fe has almost no change in four regions, and the obtained values of relative composition of each transition metal are consistent with the aimed design $Li_4Mn_4Ni_{0.5}Fe_{0.5}O_{12}$.

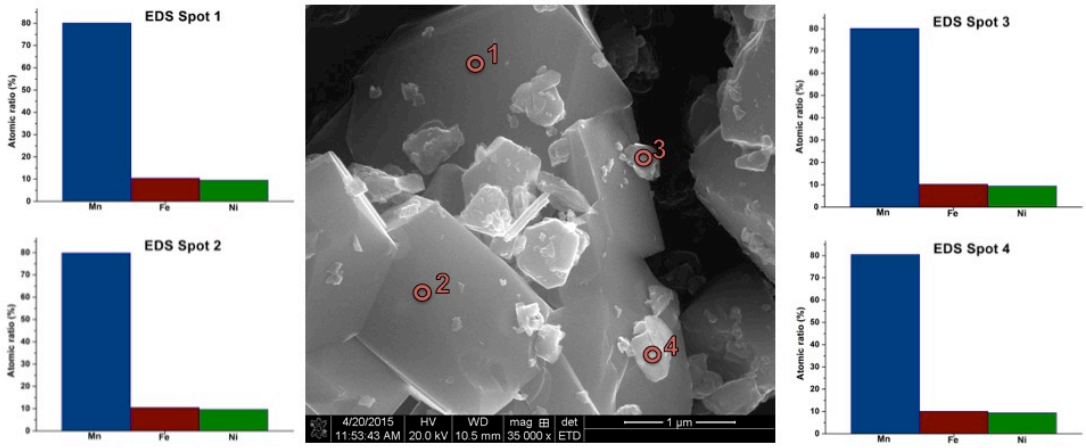


Figure 2.4 SEM image of $Li_4Mn_4Ni_{0.5}Fe_{0.5}O_{12}$ along with 4-spots EDS analysis results with respect to Mn, Ni, and Fe represented by atomic ratios among them.

Figure 2.5 presents discharge curves of various cathode materials, namely, pristine $Li_4Mn_5O_{12}$, $Li_4Mn_{4.5}Ni_{0.5}O_{12}$, $Li_4Mn_4NiO_{12}$, $Li_4Mn_{4.5}Ni_{0.25}Fe_{0.25}O_{12}$, $Li_4Mn_4Ni_{0.5}Fe_{0.5}O_{12}$ and $Li_4Mn_{3.75}Ni_{0.5}Fe_{0.75}O_{12}$, when cycled in a voltage range of 3.2 - 5.0 V *vs.* $Li/Li^+$. At a specific current of 25 mA/g (0.1 *C*), pristine $Li_4Mn_5O_{12}$ delivers a discharge capacity of 90 mAh/g in the $100^{th}$ cycle with predominant discharge voltage plateau around 4.0 V *vs.* $Li/Li^+$. It is found that all the Ni- and (Ni, Fe)-doped cathode materials demonstrate considerably increased operating voltage and discharge capacity. For example, $Li_4Mn_4Ni_{0.5}Fe_{0.5}O_{12}$ cathode delivers the highest discharge capacity of ~122 mAh/g at above 4.0 V and ~80 mAh/g at an average voltage of 4.7 V *vs.* $Li/Li^+$, which is attributed to the redox couples $Ni^{2+/3+/4+}$ and $Fe^{3+/4+}$ of doping ions. $Li_4Mn_{3.75}Ni_{0.5}Fe_{0.75}O_{12}$ shows a similar high operating voltage plateau to $Li_4Mn_4Ni_{0.5}Fe_{0.5}O_{12}$, but its discharge capacity is much lower than that of

$Li_4Mn_4Ni_{0.5}Fe_{0.5}O_{12}$, suggesting that a Fe doping ratio higher than 0.5 possibly causes instability of Ni-doped spinel structure and consequent capacity loss upon cycling. This finding is consistent with XRD and SEM results. It is important to note that discharge profiles of Ni-doped and (Ni, Fe)-doped cathodes at the 50$^{th}$ and 100$^{th}$ cycles are almost identical, showing no noticeable decrease of the high-voltage plateau during long-term cycling, which proves excellent cycling stability of cubic spinel structure.

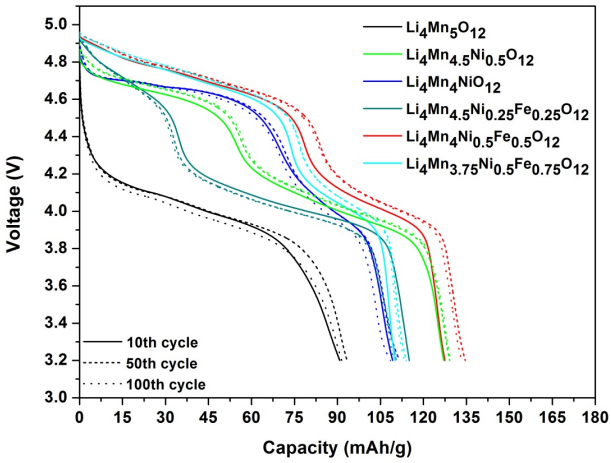


Figure 2.5 Discharge curves of pristine $Li_4Mn_5O_{12}$ and doped $Li_4Mn_{5-x-y}Ni_xFe_yO_{12}$ cathodes when cycled between 3.2 and 5.0 V *vs*. $Li/Li^+$ at 25 mA/g (0.1 *C*).

Figure 2.6a compares cycling performances of pristine $Li_4Mn_5O_{12}$ and doped $Li_4Mn_{5-x-y}Ni_xFe_yO_{12}$ cathode materials at 0.1 *C* rate. It is observed that all the samples exhibit outstanding cycling performances with a remarkable capacity retention of ~96% after 100 electrochemical cycles, which can be ascribed to intrinsic structural stability of the spinel cubic structure and the stabilizing effect from the secondary phase of layered $Li_2MnO_3$ as confirmed by XRD results earlier. Pristine $Li_4Mn_5O_{12}$ can deliver a discharge capacity of ~90 mAh/g after 100 electrochemical cycles in a voltage range of 3.2 - 5.0 V *vs.* $Li/Li^+$. Compared to pristine $Li_4Mn_5O_{12}$, all the doped $Li_4Mn_{5-x-y}Ni_xFe_yO_{12}$ samples display significantly increased discharge capacity. After 100 cycles, $Li_4Mn_{4.5}Ni_{0.5}O_{12}$, $Li_4Mn_4NiO_{12}$,

$Li_4Mn_{4.5}Ni_{0.25}Fe_{0.25}O_{12}$, $Li_4Mn_4Ni_{0.5}Fe_{0.5}O_{12}$ and $Li_4Mn_{3.75}Ni_{0.5}Fe_{0.75}O_{12}$ deliver a discharge capacity of 130, 109, 110, 133 and 115 mAh/g, respectively. Therefore, $Li_4Mn_4Ni_{0.5}Fe_{0.5}O_{12}$ exhibits the best electrochemical performance, since it provides a combination of high capacity and high operating voltage as well as excellent cycleability among various compositions investigated in this work. Fig. 2.6b presents the electrochemical impedance spectra (EIS) of pristine $Li_4Mn_5O_{12}$ and $Li_4Mn_4Ni_{0.5}Fe_{0.5}O_{12}$ (the sample with optimized composition), showing the plots composed of high and low frequency regions. The high-frequency semicircle is resulted from the charge-transfer process and the intercept of the semicircle with the Z real axis is related to the charge transfer resistance ($R_{ct}$), while the straight line in the low frequency is attributed to the Warburg diffusion of lithium ions in the electrode material. It can be seen the optimized $Li_4Mn_4Ni_{0.5}Fe_{0.5}O_{12}$ shows a lower charge transfer resistance of 76.1 Ω than that of the pristine $Li_4Mn_5O_{12}$ (92.6 Ω), indicating that Ni and Fe dual doping enhances electron transport and facilitates kinetics of the electrode material. In addition, the slope of the optimized $Li_4Mn_4Ni_{0.5}Fe_{0.5}O_{12}$ is apparently larger than that of pristine $Li_4Mn_5O_{12}$, suggesting much faster Li-ion diffusion process in $Li_4Mn_4Ni_{0.5}Fe_{0.5}O_{12}$.

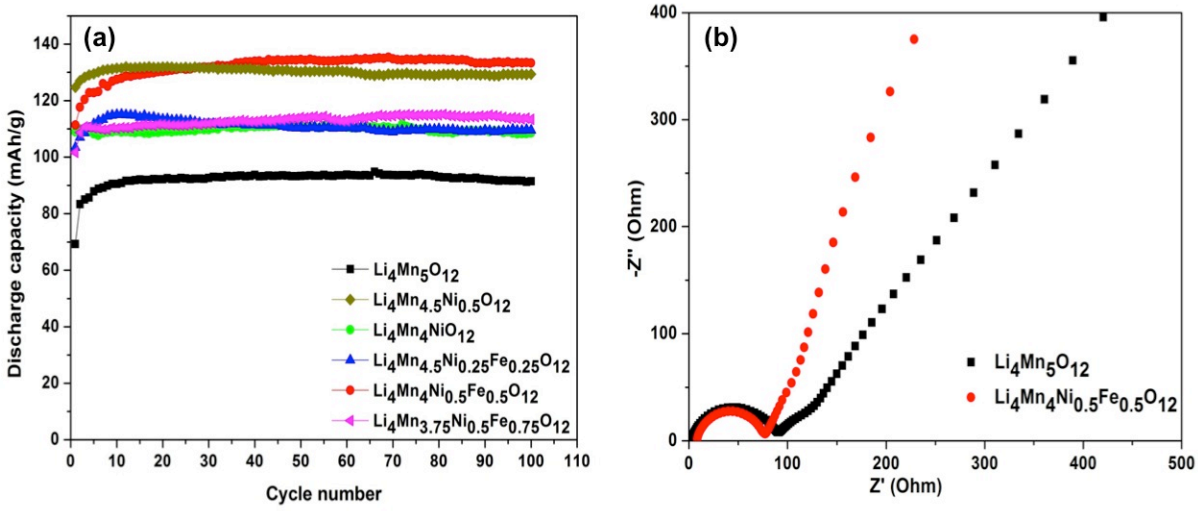


Figure 2.6 (a) Cycling performances of pristine $Li_4Mn_5O_{12}$ and doped $Li_4Mn_{5-x-y}Ni_xFe_yO_{12}$

cathodes at 0.1 *C*, (b) Electrochemical impedance spectra of pristine $Li_4Mn_5O_{12}$ and $Li_4Mn_4Ni_{0.5}Fe_{0.5}O_{12}$ (the sample with the optimized composition).

Cyclic voltammograms (CV) measurements in a voltage range of 3.2 - 5.0 V *vs*. $Li/Li^+$ at a scan rate of 0.1 mV/s at room temperature are carried out to further explore electrochemical characteristics of the doped cathode materials. As described in the experimental part, the doped samples are prepared via a facile sol-gel method combined with post-heat treatment at 900 $^oC$ for 3 hours. It is well known that all the manganese ions in pure stoichiometric $Li_4Mn_5O_{12}$ have a valence state of +4. However, spinel $Li_4Mn_5O_{12}$ is widely reported as sensitive to the synthesis or high annealing temperature (T > 500˚C), which causes it to decompose into layered $Li_2MnO_3$ and spinel $Li_{1+z}Mn_{2-z}O_4$ ($0<z<0.33$) [9, 37]; and this material is considered as a 4.0 V cathode due to the redox couple of $Mn^{3+}/Mn^{4+}$.

As seen in Figure 2.7a, pristine $Li_4Mn_5O_{12}$ shows strong peaks at ~4.2 V and ~3.8 V, corresponding to the oxidation and reduction reactions of $Mn^{3+}/Mn^{4+}$ possibly from the spinel $Li_{1+z}Mn_{2-z}O_4$ phase. It is also observed that a strong anodic peak occurs at ~4.9 V (marked as *) in the first charging process. As reported in literature, the layered $Li_2MnO_3$ can transform into $MnO_2$ due to the extraction of $Li^+$ in the form of $Li_2O$ [38-40], resulting in the above anodic peak at ~4.9 V. It is also found that such electrochemical activation of the layered $Li_2MnO_3$ is irreversible since the strong peak is weakened drastically in subsequent electrochemical cycles. However, in the case of Ni-doped cathode materials ($Li_4Mn_{4.5}Ni_{0.5}O_{12}$, $Li_4Mn_4Ni_1O_{12}$), there are two new anodic peaks appearing at 4.8 V and 4.9V as well as one new cathodic peak at 4.6 V, possibly caused by voltage difference between $Ni^{2+}/Ni^{3+}$ and $Ni^{3+}/Ni^{4+}$ redox couples. As for (Ni, Fe)-doped cathodes, there is a broad high-voltage redox peak at around 4.9 V, which is ascribed to the $Fe^{3+}/Fe^{4+}$ redox reactions. Similar results have been reported by G. B. Zhong et al [22] and Ohzuku et al [41]. It is also noted the CV curves of all the (Ni, Fe)-doped cathode materials are almost identical

in the extended cycles (3rd and 4th), suggesting improved electrochemical reversibility compared to pristine $Li_4Mn_5O_{12}$.

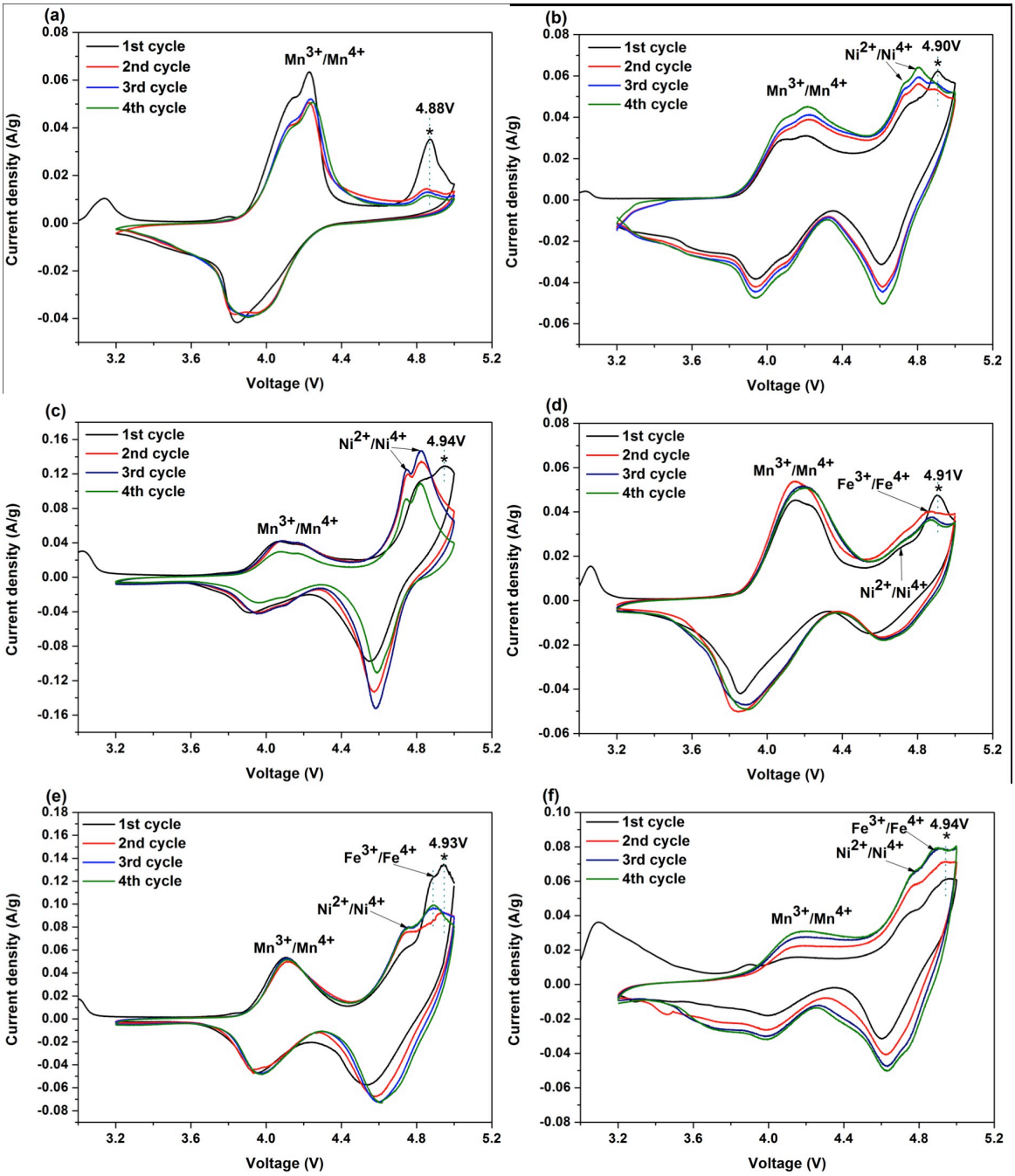


Figure 2.7 Cyclic voltammograms of (a) pristine $Li_4Mn_5O_{12}$, (b) $Li_4Mn_{4.5}Ni_{0.5}O_{12}$, (c) $Li_4Mn_4NiO_{12}$, (d) $Li_4Mn_{4.5}Ni_{0.25}Fe_{0.25}O_{12}$, (e) $Li_4Mn_4Ni_{0.5}Fe_{0.5}O_{12}$, (f) $Li_4Mn_{3.75}Ni_{0.5}Fe_{0.75}O_{12}$ cathode materials.

## 2.4 Conclusions

To achieve both high voltage and high capacity of spinel $Li_4Mn_5O_{12}$, a simple strategy of doping with transition metal Ni and Fe ions is introduced in this work. Electrochemical performances of the doped spinel powders are investigated for application as high-voltage cathode materials in LIBs up to 5.0 V. As predicted, the as-synthesized dual doped $Li_4Mn_4Ni_{0.5}Fe_{0.5}O_{12}$ cathode material not only delivers a high discharge capacity of 133 mAh/g after 100 cycles at 0.1 *C* rate, which is much higher than the capacity of 90 mAh/g from pristine $Li_4Mn_5O_{12}$, but also demonstrates a higher operating voltage increased from 4.0 to 4.7 V. According to XRD, SEM and EDS results, such enhanced electrochemical performances can be attributed to redox couples $Ni^{2+/3+/4+}$ and $Fe^{3+/4+}$ of the doping ions and the unique nano/micro structure of the doped cathode materials consisting of nano-sized particles embedded on the surface of micro-sized particles. In addition, the doping of Ni and Fe ions shows distinct effects on the morphology, crystal structure and particle size of the spinel cathode materials. Considering its facile synthesis method and remarkably improved electrochemical performance, (Ni, Fe)-doped $Li_4Mn_5O_{12}$ would be a promising high-voltage cathode material for high-energy high-power LIBs.

## 2.5 References


1. M. M. Thackeray, C. Wolverton, E. D. Isaacs, Electrical energy storage for transportation—approaching the limits of, and going beyond, lithium-ion batteries. Energy Environ. Sci, 2012, 5, 7854-7863.

2. V. Etacheri, R. Marom, R. Elazari, G. Salitra, D. Aurbach, Challenges in the development of advanced Li-ion batteries: a review. Energy Environ. Sci, 2011, 4, 3243-3262.

3. T. H. Kim, J. S. Park, S. K. Chang, S. Choi, J. H. Ryu, H. K. Song, The current move of lithium ion batteries towards the next phase. Adv. Energy Mater, 2012, 2, 860-872.

4. B. Xu, D. N. Qian, Z. Y. Wang, Y. S. Meng, Recent progress in cathode materials research for advanced lithium ion batteries. Mater. Sci. Eng, R, 2012, 73, 51-65.

5. B. L. Ellis, K. T. Lee, L. F. Nazar, Positive electrode materials for Li-ion and Li-batteries. Chem. Mater, 2010, 22, 691-714.

6. M. M. Thackeray, M. F. Mansuetto, C. S. Johnson, Thermal stability of $Li_4Mn_5O_{12}$ electrodes for lithium batteries. J. Solid State Chem, 1996, 125, 274-277.

7. Y. Shin, A. Manthiram, Origin of the high voltage (> 4.5 V) capacity of spinel lithium manganese oxides. Electrochim. Acta, 2003, 48, 3583-3592.

8. Y. P. Jiang, J. Xie, G. S. Cao, X. B. Zhao, Electrochemical performance of $Li_4Mn_5O_{12}$ nano-crystallites prepared by spray-drying-assisted solid state reactions. Electrochim. Acta, 2010, 56, 412-417.

9. J. Cao, J. Xie, G. Cao, T. Zhu, X. Zhao, S. Zhang, Electrochemical properties of $0.5Li_2MnO_3 \cdot 0.5Li_4Mn_5O_{12}$ nanotubes prepared by a self-templating method. Electrochim. Acta, 2013,111, 447-454.

10. M. M. Thackeray, L. A. de Picciotto, A. de Kock, P. J. Johnson, V. A. Nicholas, K. T. Adendorff, Spinel electrodes for lithium batteries — A review. J. Power sources, 1987, 21, 1-8.

11. S. Ivanova, E. Zhecheva, D. Nihtianova, M. Mladenov, R. Stoyanova, Electrochemical intercalation of $Li^+$ into nanodomain $Li_4Mn_5O_{12}$. J. Alloys Compd, 2013, 561, 252-261.

12. T. Takada, H. Hayakawa, E. Akiba, F. Izumi, B. C. Chakoumakos, Novel synthesis process and structure refinements of $Li_4Mn_5O_{12}$ for rechargeable lithium batteries. J. Power Sources, 1997, 68, 613-617.

13. C. H. Lu, T. Y. Wu, H. C. Wu, M. H. Yang, Z. Z. Guo, I. Taniguchi, Preparation and electrochemical characteristics of spherical spinel cathode powders via an ultrasonic spray pyrolysis process. Mater. Chem. Phys, 2008, 112, 115-119.

14. Y. X. Li, Z. L. Gong, Y. Yang, Synthesis and characterization of $Li_2MnSiO_4$/C nanocomposite cathode material for lithium ion batteries. J. Power Sources, 2007, 174, 528-532.

15. X. Li, Y. Xu, C. Wang, Suppression of Jahn–Teller distortion of spinel $LiMn_2O_4$ cathode. J. Alloys Compd, 2009, 479, 310-313.

16. H. J. Guo, Q. H. Li, X. H. Li, Z. X.Wang, W. J. Peng, Novel synthesis of $LiMn_2O_4$ with large tap density by oxidation of manganese powder. Energy Convers. Manage, 2011, 52, 2009-2014.

17. K. S. Lee, H. J. Bang, S. T. Myung, J. Prakash, K. Amine, Y. K. Sun, Synthesis and electrochemical properties of spherical spinel $Li_{1.05}M_{0.05}Mn_{1.9}O_4$ (M = Mg and Al) as a cathode material for lithium-ion batteries by co-precipitation method. J. Power Sources, 2007, 174, 726-729.

18. M. Hirayama, H. Ido, K. Kim, W. Cho, K. Tamura, J. Mizuki, R. Kanno, Dynamic structural changes at $LiMn_2O_4$/electrolyte interface during lithium battery reaction. J. Am. Chem. Soc, 2010, 132, 15268-15276.

19. H. J. Choi, K. M. Lee, J. G. Lee, $LiMn_{1.95}M_{0.05}O_4$ (M: Al, Co, Fe, Ni, Y) cathode materials prepared by combustion synthesis. J. Power Sources, 2001, 103, 154-159.

20. J. Song, D.W. Shin, Y. Lu, C. D. Amos, A. Manthiram, J. B. Goodenough, Role of Oxygen Vacancies on the Performance of Li $[Ni_{0.5-x}Mn_{1.5+x}]O_4$ (x= 0, 0.05, and 0.08) Spinel Cathodes for Lithium-Ion Batteries. Chem. Mater. 2012, 24, 3101-3109.

21. J. Zheng, J. Xiao, X. Yu, L. Kovarik, M. Gu, F. Omenya, X. Chen, X. Q. Yang, J. Liu, G. L. Graff, M. S. Whittingham, J. G. Zhang, Enhanced $Li^+$ ion transport in $LiNi_{0.5}Mn_{1.5}O_4$ through control of site disorder. Phys. Chem. Chem. Phys, 2012,14, 13515-13521.

22. G. B. Zhong, Y. Y. Wang, Y. Q. Yu, C. H. Chen, Electrochemical investigations of the $LiNi_{0.45}M_{0.10}Mn_{1.45}O_4$ (M= Fe, Co, Cr) 5 V cathode materials for lithium ion batteries. J. Power Sources, 2012, 205, 385-393.

23. J. Liu, A. Manthiram, Understanding the improved electrochemical performances of Fe-substituted 5 V spinel cathode $LiMn_{1.5}Ni_{0.5}O_4$. J. Phys. Chem. C, 2009, 113, 15073-15079.

24. K. J. Hong, Y. K. Sun, Synthesis and electrochemical characteristics of $LiCr_xNi_{0.5-x}Mn_{1.5}O_4$ spinel as 5 V cathode materials for lithium secondary batteries. J. Power Sources, 2002, 109, 427-430.

25. R. Alcántara, M. Jaraba, P. Lavela, J. L. Tirado, E. Zhecheva, R. Stoyanova, Changes in the Local Structure of $LiMg_yNi_{0.5-y}Mn_{1.5}O_4$ Electrode Materials during Lithium Extraction. Chem. Mater, 2004, 16, 1573-1579.

26. K. R. Chemelewski, A. Manthiram, Origin of site disorder and oxygen nonstoichiometry in $LiMn_{1.5}Ni_{0.5-x}M_xO_4$ (M= Cu and Zn) cathodes with divalent dopant ions. J. Phys. Chem. C, 2013, 117, 12465-12471.

27. F. Wu, N. Li, Y. Su, H. Shou, L. Bao, W. Yang, L. Zhang, R. An, S. Chen, Spinel/layered heterostructured cathode material for high-capacity and high-rate Li-ion batteries. Adv. Mater, 2013, 25, 3722-3726.

28. H. S. Fang, Z. X. Wang, X. H. Li, H. J. Guo, W. J. Peng, Exploration of high capacity $LiNi_{0.5}Mn_{1.5}O_4$ synthesized by solid-state reaction. J. Power Sources, 2006, 153, 174-176.

29. J. Zheng, J. Xiao, X. Yu, L. Kovarik, M. Gu, F. Omenya, X. Chen, X. Q. Yang, J. Liu, G. L. Graff, M. S. Whittingham, J. G. Zhang, Enhanced $Li^+$ ion transport in $LiNi_{0.5}Mn_{1.5}O_4$ through control of site disorder. Phys. Chem. Chem. Phys, 2012,14, 13515-13521.

30. S. Mukerjee, X. Q. Yang, X. Sun, S. J. Lee, J. McBreen, Y. Ein-Eli, In situ synchrotron X-ray studies on copper–nickel 5 V Mn oxide spinel cathodes for Li-ion batteries. Electrochim. Acta, 2004, 49, 3373-3382.

31. Y. Fu, H. Jiang, Y. Hu, L. Zhang, C. Li, Hierarchical porous $Li_4Mn_5O_{12}$ nano/micro structure as superior cathode materials for Li-ion batteries. J. Power Sources, 2014, 261, 306-310.

32. Y. Tian, D. Chen, X. Jiao, Y. Duan, Facile preparation and electrochemical properties of cubic-phase $Li_4Mn_5O_{12}$ nanowires. Chem. Commun, 2007, 2072-2074.

33. M. A. Kebede, N. Kunjuzwa, C. J. Jafta, M. K. Mathe, K. I. Ozoemena, Solution-combustion synthesized nickel-substituted spinel cathode materials ($LiNi_xMn_{2-x}O_4$; $0 \leq x \leq 0.2$) for lithium ion battery: enhancing energy storage, capacity retention, and lithium ion transport. Electrochim. Acta, 2014, 128, 172-177.

34. B. Ebin, S. Gurmen, C. Arslan, G. Lindbergh, Electrochemical properties of nanocrystalline $LiFe_xMn_{2-x}O_4$ (x= 0.2–1.0) cathode particles prepared by ultrasonic spray pyrolysis method. Electrochim. Acta, 2012, 76, 368-374.

35. Y. J. Wei, L. Y. Yan, C. Z. Wang, X. G. Xu, F. Wu, G. Chen, Effects of Ni doping on $[MnO_6]$ octahedron in $LiMn_2O_4$. J. Phys. Chem. B, 2004, 108, 18547-18551.

36. J. Shu, T. F. Yi, M. Shui, Y. Wang, R. S. Zhu , X. F. Chu , F. T. Huang, D. Xu, L. Hou, Comparison of electronic property and structural stability of $LiMn_2O_4$ and $LiNi_{0.5}Mn_{1.5}O_4$ as cathode materials for lithium-ion batteries. Comput. Mater. Sci, 2010, 50, 776-779.

37. Y. Xia, M. Yoshio, Optimization of Spinel $Li_{1+x}Mn_{2-y}O_4$ as a 4 V Li-Cell Cathode in Terms of a Li-Mn-O Phase Diagram. J. Electrochem. Soc., 1997, 144, 4186-4194.

38. N. Yabuuchi, K. Yoshii, S. T. Myung, I. Nakai, S. Komaba, Detailed studies of a high-capacity electrode material for rechargeable batteries, $Li_2MnO_3$− $LiCo_{1/3}Ni_{1/3}Mn_{1/3}O_2$. J. Am. Chem. Soc., 2011, 133, 4404-4419.

39. F. Amalraj, M. Talianker, B. Markovsky, D. Sharon, L. Burlaka, G. Shafir, E. Zinigrad, O. Haik, D. Aurbach, J. Lampert, M. Schulz-Dobrick, A. Garsuch, Study of the Lithium-Rich Integrated Compound $xLi_2MnO_3 \cdot (1\text{-}x)LiMO_2$ (x around 0.5; M = Mn, Ni, Co; 2:2:1) and Its Electrochemical Activity as Positive Electrode in Lithium Cells. J. Electrochem. Soc., 2012, 160, A324-A337.

40. C. S. Johnson, N. Li, J. T. Vaughey, S. A. Hackney, M. M. Thackeray, Lithium–manganese oxide electrodes with layered–spinel composite structures $xLi_2MnO_3 \cdot (1-x)Li_{1+y}Mn_{2-y}O_4$ ($0 < x < 1,\ 0 \leqslant y \leqslant 0.33$) for lithium batteries. Electrochem. Commun., 2005, 7, 528-536.

41. T. Ohzuku, S. Takeda, M. Iwanaga, Solid-state redox potentials for $Li[Me_{1/2}Mn_{3/2}]O_4$ (Me: 3d-transition metal) having spinel-framework structures: a series of 5 volt materials for advanced lithium-ion batteries. J. Power Sources, 1999, 82, 90-94.

42. C. M. Sim, Y. J. Hong, M. H. Kim, Y. S. Jang, B. K. Park, Y. C. Kang, Electrochemical and physical properties of layered-spinel composite cathode powders prepared by spray pyrolysis. Int. J. Electrochem. Sci., 2012, 7, 12110-12120.

43. J. Cao, J. Xie, G. Cao, T. Zhu, X. Zhao, S. Zhang, Electrochemical properties of $0.5Li_2MnO_3 \cdot 0.5Li_4Mn_5O_{12}$ nanotubes prepared by a self-templating method. Electrochim. Acta, 2013, 111, 447-454.

# CHAPTER 3. A NOVEL PREPARATION OF CORE-SHELL ELECTRODE MATERIALS VIA EVAPORATION-INDUCED SELF-ASSEMBLY OF NANOPARTICLES FOR ADVANCED LI-ION BATTERIES*

## 3.1 Introduction

The main drawbacks of commercial $LiCoO_2$ cathode materials such as limited delivery capacity, toxicity as well as high cost have hindered their application in plug-in hybrid electric vehicles (PHEV) or electric vehicles (EV).[1,2] In this regard, Li-rich layered oxides have attracted extensive attention due to their high specific capacity of ~250 mA h $g^{-1}$ when cycled over a broad voltage range between 2.0 and 4.8 V *versus* $Li/Li^+$ and other advantages such as environmental benignity, safety and relatively low cost.[3,4] Among Li-rich layered oxides, $Li[Li_{0.2}Mn_{0.54}Ni_{0.13}Co_{0.13}]O_2$, a solid solution in a two component notation as $0.5Li_2MnO_3 \cdot 0.5LiMn_{1/3}Ni_{1/3}Co_{1/3}O_2$ (hereafter denoted as LMNCO), has attracted extensive attention due to its extremely high theoretical capacity of 321 mA h $g^{-1}$, better cycling stability and rate capability than other Li-rich analogs. Unfortunately, these materials still suffer from unsatisfactory cycling stability and intrinsically poor rate capability.[3–5] Moreover, it has been reported that Li-rich layered oxides suffer from surface vulnerability at high voltage and erosion from electrolytes.[6–9] In order to address these challenges, many efforts have been devoted to improving the structural and surface stabilities by using a simple surface modification strategy. Up to now, various metal oxides ($Al_2O_3$,[10] $CeO_2$[11]*etc.*), fluorides and phosphates,[12–14] as well as some other Li-ion conducting $LiNiPO_4$,[15,16] $LiAlO_2$[17] and $Li_2ZrO_3$ [18] have been applied to stabilize the surface structure of Li-rich layered oxides and suppress side-reactions between the electrode and electrolyte, thereby leading to improved cycling performance and thermal stability. However, such coating

* This chapter previously appeared as Zhiqiang Xie, Sarah Ellis, Wangwang Xu, Dara Dye, Jianqing Zhao and Ying Wang, "A novel preparation of core-shell electrode materials via evaporation-induced self-assembly of nanoparticles for advanced Li-ion batteries", Chemical Communication, 2015, 51, 15000-15003. It is reprinted by permission of The Royal Society of Chemistry (RSC).

materials are either poor electronic or ionic conductors and generally are not electrochemically active, thereby leading to limited improvement in electrochemical performance of Li-rich layered oxides.

Recently, lithium manganese oxide (LMO) based spinel cathodes have attracted intensive attention due to their high rate capability resulting from their efficient 3D $Li^+$ diffusion channels.[19,20] Among them, spinel $Li_{1+x}Mn_2O_4$ has been studied as the coating material to overcome the above-mentioned drawbacks of Li-rich layered oxide materials. [21] In the design of a layered-spinel core–shell heterostructure, the spinel coating with efficient 3D Li-ion transport channels was expected to stabilize the layered bulk upon high-voltage cycling and to rapidly transport Li ions between the layered bulk and electrolyte, leading to improvements in both cycling stability and rate capability of Li-rich layered oxide cathodes. However, preparation of core–shell heterostructures reported in the literature required complex procedures and precise control of reaction conditions such as pH and concentration of the solutions, which poses challenges for large-scale production for high-energy high-power LIBs.[22] In addition, the spinel $Li_{1+x}Mn_2O_4$ has been reported to have an unsatisfactory cycling stability due to Jahn–Teller distortion and manganese dissolution through a disproportionation reaction.[23,24]

To improve electrochemical properties of conventional spinel $Li_{1+x}Mn_2O_4$, it is found in our recent work that Ni-doped spinel $Li_4Mn_5O_{12}$ ($Li_4Mn_{4.5}Ni_{0.5}O_{12}$) can be charged to around 5.0 V and show remarkable high-voltage cycling stability at room temperature.[25] In addition, its 3D $Li^+$ ion diffusion pathways ensure its excellent rate capability.[26] Therefore, it can be expected to be a promising coating material to replace spinel $Li_{1+x}Mn_2O_4$. Herein, we report a simple and facile one-pot preparation of L@S core–shell structure (Li-rich layered-spinel core–shell heterostructure) *via* evaporation-induced self-assembly (EISA) of ultrafine $Li_4Mn_{4.5}Ni_{0.5}O_{12}$ nanoparticles onto the surface of Li-rich layered

$Li[Li_{0.2}Mn_{0.54}Ni_{0.13}Co_{0.13}]O_2$ (LMNCO) without using any surfactant during the coating process. In this study, we also introduce a simple route to prepare ultrafine $Li_4Mn_{4.5}Ni_{0.5}O_{12}$ nanoparticles (5–20 nm) from the spinel $Li_4Mn_{4.5}Ni_{0.5}O_{12}$ bulk by the so-called sonofragmentation. Sonofragmentation is a well-known one-step process to directly produce nanoparticles from large-grained powders.[27,28] It has been reported that even intrinsically strong carbon nanotubes can be fragmented by sonication.[29] As a result, the as-prepared L@S core–shell material demonstrates significantly improved specific capacity, cycling performance and rate capability for application as a cathode in new-generation LIBs compared to pristine LMNCO. Due to the structural and functional versatility of nanoparticles, the synthetic approach reported in this work can be generalized to other materials to form novel core–shell structures, for applications in LIBs or other fields.

### 3.2 Experimental Section

3.2.1 Synthesis of core Li-excess $Li[Li_{0.2}Mn_{0.54}Ni_{0.13}Co_{0.13}]O_2$ nanoparticles.

Li-excess $Li[Li_{0.2}Mn_{0.54}Ni_{0.13}Co_{0.13}]O_2$ nanoparticles were synthesized using surfactant-assisted dispersion in a sol-gel method. We first prepared three precursor solutions: 5.4 mmol F127 ($EO_{106}PO_{70}EO_{106}$) in 50 mL ethanol, 0.08 mol transition metal acetate tetrahydrates (a molar ratio of $Mn^{2+}$ : $Ni^{2+}$: $Co^{2+}$=0.54 : 0.13 : 0.13) in 50 mL ethanol, and 0.12 mol lithium hydroxide in 20 mL DI water. The molar ratio of F127/$Mn^{2+}$ was 0.01. The transition metal precursor solution was added dropwise into the F127/ethanol solution under continuous stirring at 40°C, and then the lithium precursor solution was added. The mixed solution was heated at 80°C until the solvent was completely evaporated. Afterwards, the mixture was dried in air at 120°C for 12 h. The heat treatment of the dried mixture was carried out in air at 300°C for 3h, followed by sintering at 900°C for 12 h. $Li[Li_{0.2}Mn_{0.54}Ni_{0.13}Co_{0.13}]O_2$ nanoparticles were collected after cooling to room temperature. dnot adjust margins

3.2.2 Synthesis of shell layered-spinel integrated $Li_4Mn_{4.5}Ni_{0.5}O_{12}$ material.

The layered-spinel integrated $Li_4Mn_{4.5}Ni_{0.5}O_{12}$ was synthesized by a facile sol-gel method. Two precursor solutions were first prepared: 20 mmol transition metal (II) acetate tetrahydrates (a molar ratio of Mn2+:Ni2+=9:1) in 50 mL distilled water, and 16 mmol lithium hydroxide in 15 mL distilled water. The transition metal precursor solution was added dropwise into the lithium precursor solution under continuous stirring. The mixed solution was then heated at 80°C until the solvent was completely evaporated. Afterwards, the mixture was dried in air at 120°C for 12 h. The heat treatment of the dried mixture was carried out in air at 500°C for 5 h, followed by sintering at 900°C for 3h. The as-prepared particles were collected after cooling to room temperature.

3.2.3 Preparation of core-shell composite materials.

Ten mg $Li_4Mn_{4.5}Ni_{0.5}O_{12}$ was first dispersed in 20 mL ethanol in a sealed vial using an one-step sonication treatment in a VWR B2500A-BTH ultrasonication water bath, operating at 210 W and 40 kHz for 2 h. 90 mg $Li[Li_{0.2}Mn_{0.54}Ni_{0.13}Co_{0.13}]O_2$ powders were then added into the as-prepared suspension of $Li_4Mn_{4.5}Ni_{0.5}O_{12}$, followed by continuously stirring at 80°C until the solvent was completely evaporated. The composite materials were dried in air at 120°C for 12 h. The heat treatment of the dried powders was carried out in air at 500°C for 3 h and collected after cooling to room temperature.

3.2.4 Material characterizations

The crystal structure of the obtained powders was investigated by x-ray diffraction (XRD) using a Rigaku MiniFlex X-ray diffractometer with Cu Kα radiation. XRD Data was collected in the range of $10^{\circ} \leq 2\theta \leq 80^{\circ}$ at a scan rate of 2o/min at $\theta$ room temperature. The Morphology of the samples was observed using field emission scanning electron microscopy (FE-SEM) on a FEI Quanta 3D FEG FIB/SEM dual beam system. Transmission electron microscopy (TEM) and high-resolution TEM (HRTEM) images were captured to investigate

the crystal structure and core-shell structure of samples using a JEM-2010 instrument microscope at an acceleration voltage of 200 kV.

3.2.5 Electrochemical Measurements

Electrochemical properties of the synthesized cathode materials were evaluated using 2032-type coin cells. Typically, the cathodes were prepared by uniformly coating a homogeneous slurry of 80 wt % active material powders, 10 wt % acetylene black (conductive carbon, Alfa Aesar, 99.5%), and 10 wt % polyvinylidene fluoride (PVDF, Alfa Aesar) binder in 1-methyl-3-pyrrolidone (NMP) solvent on aluminum foils and then dried in vacuum at 120˚C for 24 h. Coin cells were assembled in an argon-filled glove box. The electrolyte was 1 M LiPF6 dissolved in ethylene carbonate (EC), dimethyl carbonate (DMC) and diethyl carbonate (DEC) at a volumetric ratio of 1:1:1. The electrochemical performance was tested at various C-rate regimes in the voltage range of 2.0-4.99 V by using an 8-channel battery analyzer (MTI Corporation). 1C rate was defined as 250 mAh/g. Cyclic voltammetric (CV) measurement was carried out on a CHI605C electrochemical analyzer at a scanning rate of 0.1 mV/s between 2.0 V and 4.99 V vs. $Li/Li^+$. All electrochemical measurements were performed at room temperature.

**3.3 Results and Discussion**

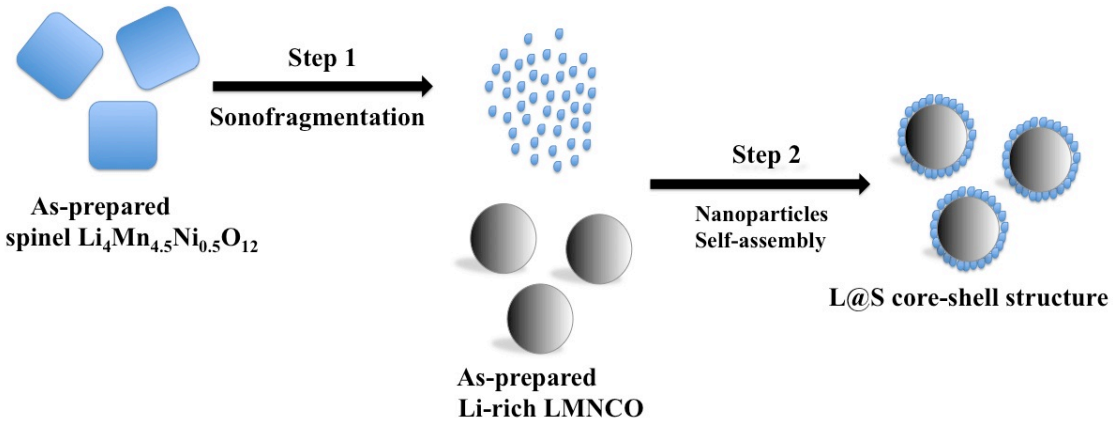


Figure 3.1 Schematic illustration of facile preparation of L@S core-shell heterostructure.

Figure 3.1 presents a schematic illustrating the facile synthesis procedure of L@S core-shell heterostructure via EISA, which is different from existing methods such as "dip and dry"[21] or co-precipitation.[22] Briefly, simple top-down preparation of spinel $Li_4Mn_{4.5}Ni_{0.5}O_{12}$ nanoparticles is introduced by applying ultrasonication to larger $Li_4Mn_{4.5}Ni_{0.5}O_{12}$ particles in ethanol for two hours. The large-sized $Li_4Mn_{4.5}Ni_{0.5}O_{12}$ particles are broken into smaller nanoparticles due to mechanical energy of ultrasonic wave. Afterwards, as described in the experimental part, the resultant suspension of $Li_4Mn_{4.5}Ni_{0.5}O_{12}$ ultrafine nanoparticles in ethanol are mixed with $Li[Li_{0.2}Mn_{0.54}Ni_{0.13}Co_{0.13}]O_2$ suspension in ethanol, followed by continuously stirring at 80°C until the solvent is completely evaporated. In this step, ultrafine nanoparticles of $Li_4Mn_{4.5}Ni_{0.5}O_{12}$ tend to self-assembly on the surface of large-sized $Li[Li_{0.2}Mn_{0.54}Ni_{0.13}Co_{0.13}]O_2$ particles in order to drastically reduce surface energy. Finally, after post-annealing at 500°C for 3 hours, L@S core-shell heterostructure is successfully obtained.

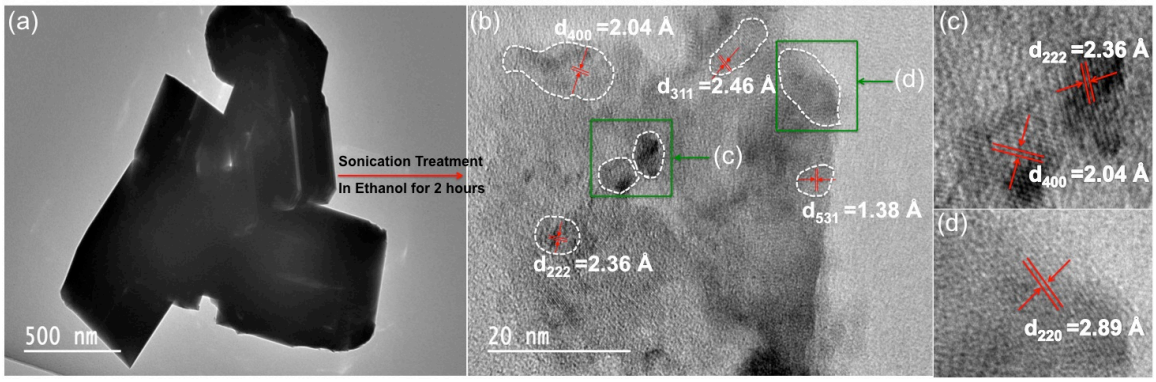


Figure 3.2 (a) TEM bright field images of spinel $Li_4Mn_{4.5}Ni_{0.5}O_{12}$ particles before sonofragmentation, (b) HRTEM image of $Li_4Mn_{4.5}Ni_{0.5}O_{12}$ after sonofragmentation, with (c) and (d) showing zoom-in view of two regions in the green rectangles in (b).

The as-prepared spinel $Li_4Mn_{4.5}Ni_{0.5}O_{12}$ particles are characterized by both scanning electron microscopy (SEM) and transmission electron microscopy (TEM). The SEM image of $Li_4Mn_{4.5}Ni_{0.5}O_{12}$ particles before sonofragmentation in Figure S1 shows numerous highly-crystalline nanoparticles with smooth surfaces. Figure 3.2a and b display TEM and high-resolution TEM (HRTEM) images of spinel $Li_4Mn_{4.5}Ni_{0.5}O_{12}$ powders before and after sonofragmentation, respectively. Figure 3.2a reveals the average size of primary $Li_4Mn_{4.5}Ni_{0.5}O_{12}$ particles is ~500 nm. Interestingly, it is found in Figure 2b and c that sonication can effectively reduce the particle size of $Li_4Mn_{4.5}Ni_{0.5}O_{12}$ powders into nanoscale (5~20 nm). The lattice fringes of each nanoparticle in Figure 3.2c are clearly observed. The zoom-in view of two regions in green rectangles in Figure 3.2b is displayed in Figure 3.2c and d. The lattice fringes of the $Li_4Mn_{4.5}Ni_{0.5}O_{12}$ surface coating can be readily indexed to the planes of (222), (400) and (220), respectively, suggesting the efficient preparation of ultrafine monocrystalline nanoparticles by using the sonication treatment. This approach demonstrates a promising way to produce various inorganic nanoparticles and will find wide potential applications in many fields such as nano-scale electronic devices.

As revealed in the SEM image of pristine layered LMNCO in Figure 3.3a, the sample is composed of nanoparticles (~200 nm) with smooth surface, indicating their highly crystalline nature. It is noted that L@S core-shell sample looks very similar to LMNCO particles under SEM since the ultrathin coating cannot be detected by SEM. Therefore, TEM is used to examine morphology of the core-shell structure as shown in Figure 3.3c and d. Crystal structures of the as-prepared pristine layered LMNCO, spinel $Li_4Mn_{4.5}Ni_{0.5}O_{12}$ and L@S core-shell samples are further identified using powder X-ray diffraction (XRD) as shown in Figure 3.3b. The main peaks from the $Li_4Mn_{4.5}Ni_{0.5}O_{12}$ sample can be readily indexed to $Li_4Mn_5O_{12}$ with spinel phase of face-centered cubic structure (ICDD: 46-0810). A secondary phase of monoclinic $Li_2MnO_3$ with C2/m symmetry (ICDD: 84-1634) is evidenced as well, which might be ascribed to decomposition of $Li_4Mn_5O_{12}$ spinel phase during post-heat treatment at 900ºC.[25] The strong peaks from both pristine LMNCO and L@S core-shell heterostructure samples can be indexed as a layered α-$NaFeO_2$ structural type with space group R3m symmetry and some weak superstructure reflections (marked as * in Figure 3b) can be ascribed to monoclinic phase $Li_2MnO_3$. Compared to XRD patterns of pristine LMNCO and spinel $Li_4Mn_{4.5}Ni_{0.5}O_{12}$, the XRD pattern from the L@S core-shell heterostructure sample combines with the patterns of both layered structure and cubic spinel structure with weak shoulder peaks assigned to the spinel coating as pointed by the arrows in Figure 3.3b.

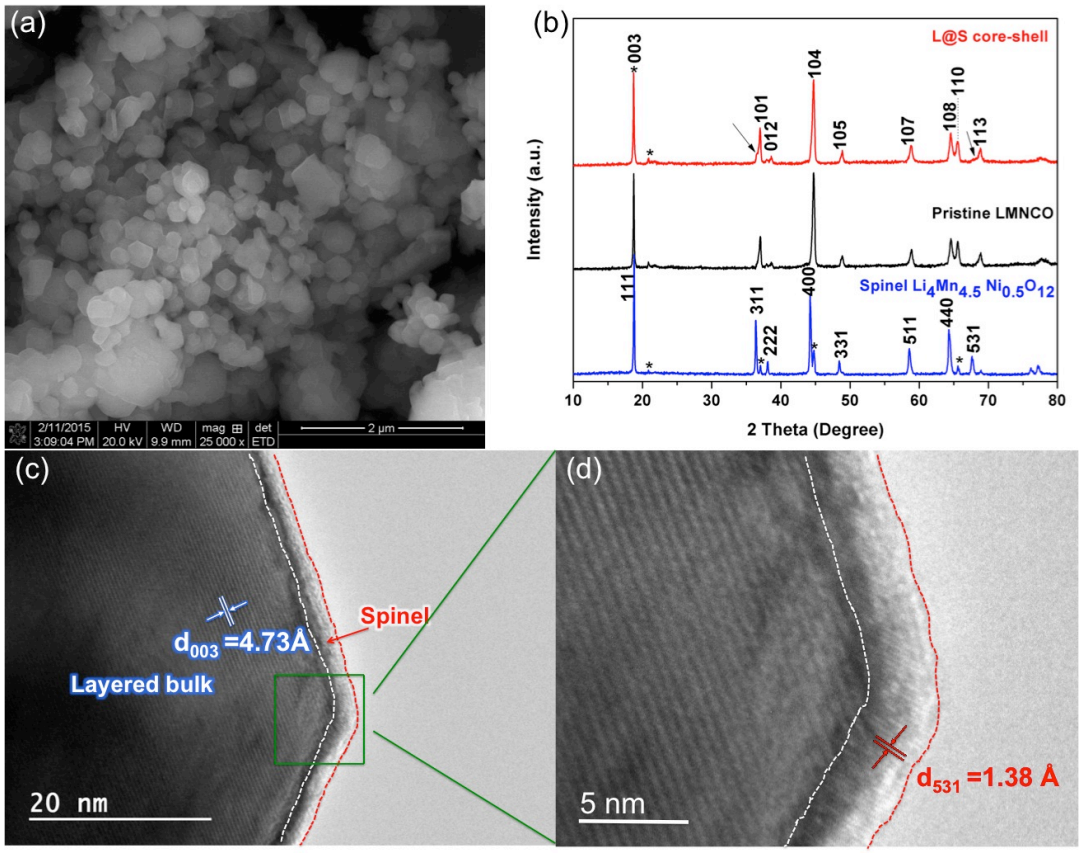


Figure 3.3 (a) SEM image of pristine layered LMNCO, (b) Powder XRD patterns of spinel $Li_4Mn_{4.5}Ni_{0.5}O_{12}$, pristine layered LMNCO, L@S core-shell heterostructured powders, (c) HRTEM images of L@S core-shell sample and (d) zoom-in view of the surface of L@S core-shell in the green rectangle in (c).

High-resolution TEM (HRTEM) is used to examine L@S core-shell sample to further identify its surface structure. As observed in Figure 3.3c, the bulk layered structure of pristine LMNCO is well-preserved in the L@S core-shell structure, displaying lattice fringes with an interplanar spacing of ca. 4.73 Å. It can also be seen that a homogeneous outer layer is uniformly coated on the surface of layerd LMNCO bulk. The enlarged view in Figure 3.3d reveals a crystalline outer layer with lattice fringes showing an interplanar spacing of ca. 1.38 Å, which do not belong to the layered structure but are consistent with the (531) plane of the cubic spinel (Fd-3m), confirming that the outer layer is the spinel coating. Therefore, it can

be concluded that novel L@S core-shell structure can be facilely synthesized via evaporation-induced self-assembly of nanoparticles, which opens new route for achieving various core-shell structures for different applications.

Figure 4.4a and b compares initial three charge/discharge curves of pristine LMNCO and L@S core-shell heterostructured cathodes when cycled between 2.0 and 4.99 V *vs*. $Li/Li^+$ at 25 mA/g (~0.1 *C*). It is found that L@S core-shell heterostructured cathode is capable of providing a discharge capacity of ~272 mAh/g after three cycles, which is higher than pristine LMNCO that delivers a discharge capacity of ~248 mAh/g. Compared to the discharge plot of pristine LMNCO, two newly-formed plateaus at around 4.7 and 2.7 V are observed for L@S core-shell heterostructured sample, which is associated with the coating of spinel $Li_4Mn_{4.5}Ni_{0.5}O_{12}$.[25, 26] Therefore, lithium ions can be intercalated into the spinel coating at around 4.7 and 2.7 V (marked by arrows) during the discharge process, thereby leading to higher discharge capacities of L@S core-shell structure.

In order to compare cycling stability of L@S core-shell and pristine LMNCO cathodes, both samples are cycled at 0.1 and 0.5 C in the wide high-voltage range between 2.0 – 4.99 V *vs*. $Li/Li^+$, respectively, as shown in Fig. 3.4c and d. As observed in Figure 3.4c, pristine LMNCO delivers a maximal capacity of ~258 mAh/g and maintains ~233 mAh/g after 60 cycles at 0.1 *C*. In contrast, L@S core-shell cathode delivers a maximal capacity of ~ 286 mAh/g and retains 273 mAh/g after 60 cycles exhibiting a higher capacity retention of 95.4 % than that of the pristine LMNCO (90.3%). Figure 3.4d compares cycling performances of the two samples at a higher rate of 0.5 *C*. In this test, L@S core-shell delivers a maximal capacity of ~ 183 mAh/g and retains ~ 153 mAh/g after 100 cycles, which is much higher than that of pristine LMNCO giving ~125 mAh/g after 100 cycles. The improvement in cycling performance and specific capacity herein can be ascribed to the stabilizing effect of thin spinel phase coating, which not only helps to reduce the erosion

from electrolyte under high voltage but also restrain the bulk LMNCO active-mass loss during long cycling.

Figure 3.4e summarizes rate performances of pristine LMNCO and L@S cathodes at various charge/discharge rates, namely 0.1 *C*, 0.2 *C*, 0.5 *C*, 1 *C*, 2 *C* and 5 *C* at 2.0 – 4.99 V *vs*. $Li/Li^+$. It is found that pristine LMNCO shows a poor rate capability, with almost no discharge capacity at 5 *C* though a good recovery to ~225 mAh/g when cycled back to 0.1 *C*. On the contrary, L@S core-shell sample delivers initial discharge capacities of 126 mAh/g, 97 mAh/g and 37 mAh/g at 1 *C,* 2 *C* and 5 *C*, respectively; when cycled back to 0.1 *C* from 5 *C*, its discharge capacity reaches as high as 269 mAh/g, demonstrating an outstanding electrochemical reversibility. Such enhanced rate performance is resulted from the following factors. First, the spinel coating with excellent structural stability can effectively stabilize the surface structure of LMNCO core, thereby reducing the erosion from the electrolyte and the bulk active-mass lose. Second, the spinel coating facilitates fast Li ions diffusion from the electrolyte to the layered LMNCO core. In addition, due to structural compatibility between the layered LMNCO and spinel phase coating, L@S is expected to have high structural stability. It is also noted that the L@S core-shell cathode needs more charge-discharge cycles to reach its maximum capacity at 0.1 *C* than pristine LMNCO cathode. The reason for this difference can be attributed to the relatively uniform spinel $Li_4Mn_{4.5}Ni_{0.5}O_{12}$ coating at the outer surface of the LMNCO core, which leads to the gradual electrochemical activation of the $Li_2MnO_3$ component in LMNCO core during the initial several cycles. As a result, L@S core-shell composite cathode needs more electrochemical cycles to reach its maximum capacity in comparison with the pristine LMNCO.

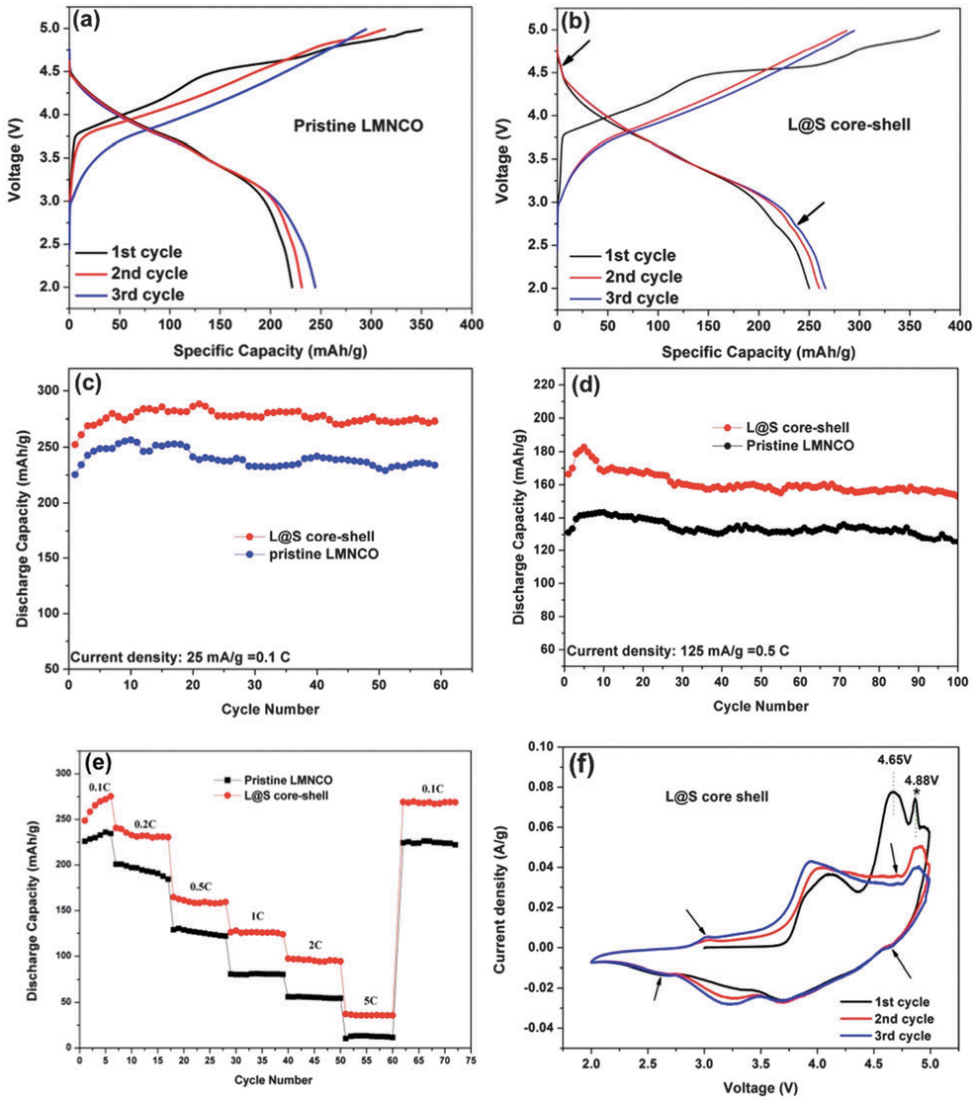


Figure 3.4 Initial three charge/discharge curves of (a) pristine layered LMNCO, (b) L@S core-shell heterostructured cathodes when cycled between 2.0 - 4.99 V *v*s. Li/Li$^+$ at a specific current of 25 mA/g (0.1*C*). (c) and (d): Cycling performances of pristine LMNCO and L@ core-shell cathodes at 0.1 and 0.5 *C*, respectively. (e) Rate performances of pristine LMNCO and L@S core-shell cathodes at various charge/discharge rates. (f) Cyclic voltammograms of L@S core-shell cathode in the first three cycles at a scan rate of 0.1 mV/s in a voltage range of 2.0 - 4.99 V *vs*. Li/Li$^+$.

Cyclic voltammetric (CV) measurements are then carried out to further explore electrochemical characteristics of the core, shell, and core-shell materials. Fig. S2 presents the first CV three cycles of pristine LMNCO and spinel $Li_4Mn_{4.5}Ni_{0.5}O_{12}$, respectively, at a

scan rate of 0.1 mV/s in the voltage range of 2.0 - 4.99 V. As for the CV curve of pristine LMNCO (Fig. S2a), the first pair of redox peaks at 4.16/3.63 V in the first electrochemical cycle corresponds to the redox reactions of $Ni^{2+}/Ni^{4+}$ followed by $Co^{3+}/Co^{4+}$, while Mn still remains as tetravalent in $LiMn_{1/3}Ni_{1/3}Co_{1/3}O_2$ structure.[30, 31] The anodic peak at 4.67 V is associated with decomposition of $Li_2MnO_3$ to $Li_2O$ and Li-active $MnO_2$, the unavoidable decomposition of electrolyte and formation of solid electrolyte interphase (SEI) at such a high potential above 4.5 V.[32] Such an electrochemical activation process of $Li_2MnO_3$ would result in high capacity of LMNCO via simultaneously losing oxygen irreversibly as $Li_2O$ and $MnO_2$. Therefore, the cathodic peak at ~3.0 V becomes apparent after charging to 4.99 V and can be attributed to the redox reaction of $Mn^{3+}/Mn^{4+}$ that may take place in the electrochemical reaction after the $Li_2MnO_3$ component is electrochemically activated. It is also found that the anodic peak at 4.67 V in the first CV curve disappears in subsequent CV cycles. Fig. S2b displays a typical CV curve of spinel $Li_4Mn_{4.5}Ni_{0.5}O_{12}$. It is clearly observed that the 2$^{nd}$ and 3$^{rd}$ curves of spinel $Li_4Mn_{4.5}Ni_{0.5}O_{12}$ are almost identical, indicating outstanding electrochemical reversibility and structural stability during cycling over a wide voltage range between 2.0 and 4.99 V *vs*. $Li/Li^+$, which is expected to be a promising surface coating for pristine LMNCO. In the CV curves of LMNCO coated with spinel $Li_4Mn_{4.5}Ni_{0.5}O_{12}$ (L@S core-shell) as shown in Figure 3.4f, it is found that the L@S core-shell cathode shows a slightly better electrochemical reversibility than pristine LMNCO. The redox peaks at 4.16/3.63 V are associated with oxidation of $Co^{3+}/Co^{4+}$ redox only from LMNCO core and $Ni^{2+}/Ni^{4+}$ redox from both LMNCO core and spinel $Li_4Mn_{4.5}Ni_{0.5}O_{12}$ shell. Interestingly, the above redox peaks from L@S core-shell show higher corresponding current density than that of pristine LMNCO, probably attributed to the thin spinel coating that reduces the erosion from electrolyte and transition-metal ion dissolution. It is also noted that some peaks (pointed by arrows in the Figure 3.4f) and another extra peak at 4.88 V can be

ascribed to the spinel phase coating, confirming the L@S core-shell heterostructure, which is consistent with the XRD and TEM results.

### 3.4 Conclusions

In conclusion, we report simple and novel synthesis of L@S core-shell structured electrode material via facile evaporation-induced self-assembly (EISA) of ultrafine crystalline $Li_4Mn_{4.5}Ni_{0.5}O_{12}$ nanoparticles on the surface of Li-rich layered $Li[Li_{0.2}Mn_{0.54}Ni_{0.13}Co_{0.13}]O_2$ particles. This L@S core-shell cathode material demonstrates significantly improved specific capacity, cycling performance and rate capability compared to pristine Li-rich layered cathode. Due to structural and functional versatility of nanoparticles, our study provides new insights into preparation of various core-shell structures via EISA of nanoparticles for applications in LIBs or other energy-related fields.

### 3.5 References


1. J. B. Goodenough, Y. Kim, Challenges for rechargeable Li batteries. Chem. Mat., 2010, 22, 587-603.

2. M. Armand, J. M. Tarascon, Building better batteries. Nature, 2008, 451, 652-657.

3. B. Xu, C. R. Fell, M. Chi, Y. S. Meng, Identifying surface structural changes in layered Li-excess nickel manganese oxides in high voltage lithium ion batteries: A joint experimental and theoretical study. Energy Environ. Sci., 2011, 4, 2223-2233.

4. M. Gu, A. Genc, I. Belharouak, D. Wang, K. Amine, S. Thevuthasan, D. R. Baer, J. G. Zhang, N. D. Browning, J. Liu, C. Wang, Nanoscale phase separation, cation ordering, and surface chemistry in pristine $Li_{1.2}Ni_{0.2}Mn_{0.6}O_2$ for Li-ion batteries. Chem. Mater., 2013, 25, 2319-2326.

5. H. Yu, H. Zhou, High-energy cathode materials ($Li_2MnO_3$–$LiMO_2$) for lithium-ion batteries. J. Phys. Chem. Lett., 2013, 4, 1268-1280.

6. D. Wang, I. Belharouak, G. Zhou, K. Amine, Nanoarchitecture multi-structural cathode materials for high capacity lithium batteries. Adv. Funct. Mater., 2012, 23, 1070-1075.

7. L. Chen, Y. F. Su, S. Chen, N. Li, L. Y. Bao, W. K. Li, Z. Wang, M. Wang, F. Wu, Hierarchical $Li_{1.2}Ni_{0.2}Mn_{0.6}O_2$ nanoplates with exposed {010} planes as high-performance cathode material for lithium-ion batteries. Adv. Mater., 2014, 26, 6756-6760.

8. H. Liu, C. Y. Du, G. P. Yin, B. Song, P. J. Zuo, X. Q. Cheng, Y. L. Ma, Y. Z. Gao, An Li-rich oxide cathode material with mosaic spinel grain and a surface coating for high performance Li-ion batteries. J. Mater. Chem. A., 2014, 2, 15640-15646.

9. A. R. Armstrong, M. Holzapfel, P. Novak, C. S. Johnson, S. H. Kang, M. M. Thackeray, P. G. Bruce, Demonstrating oxygen loss and associated structural reorganization in the lithium battery cathode $Li[Ni_{0.2}Li_{0.2}Mn_{0.6}]O_2$. J. Am. Chem. Soc., 2006, 128, 8694-8698.

10. G. S. Zou, X. K. Yang, X. Y. Wang, L. Ge, H. B. Shu, Y. S. Bai, C. Wu, H. P. Guo, L. Hu, X. Yi, B. W. Ju, H. Hu, D. Wang, R. Z. Yu, Improvement of electrochemical performance for Li-rich spherical $Li_{1.3}[Ni_{0.35}Mn_{0.65}]O_{2+x}$ modified by $Al_2O_3$. J. Solid State Electrochem., 2014, 18, 1789-1797.

11. W. Yuan, H. Z. Zhang, Q. Liu, G. R. Li, X. P. Gao, Surface modification of $Li(Li_{0.17}Ni_{0.2}Co_{0.05}Mn_{0.58})O_2$ with CeO2 as cathode material for Li-ion batteries. Electrochim. Acta, 2014, 135, 199-207.

12. Y. K. Sun, M. J. Lee, C. S. Yoon, J. Hassoun, K. Amine, B. Scrosati, The role of $AlF_3$ coatings in improving electrochemical cycling of Li-enriched nickel-manganese oxide electrodes for Li-ion batteries. Adv. Mater., 2012, 24, 1192-1196.

13. M. S. Park, J. W. Lee, W. Choi, D. Im, S. G. Doo, K. S. Park, On the surface modifications of high-voltage oxide cathodes for lithium-ion batteries: new insight and significant safety improvement. J. Mater. Chem., 2010, 20, 7208-7213.

14. Q. Wang, J. Liu, A. V. Murugan and A. Manthiram, High capacity double-layer surface modified $Li[Li_{0.2}Mn_{0.54}Ni_{0.13}Co_{0.13}]O_2$ cathode with improved rate capability. J. Mater. Chem., 2009, 19, 4965-4972.

15. S. H. Kang, M. M. Thackeray, Enhancing the rate capability of high capacity $xLi_2MnO_3 \cdot (1-x)LiMO_2$ (M = Mn, Ni, Co) electrodes by Li–Ni–$PO_4$ treatment. Electrochem. Commun., 2009, 11, 748-751.

16. J. R. Croy, M. Balasubramanian, D. Kim, S. H. Kang, M. M. Thackeray. Designing high-capacity, lithium-ion cathodes using X-ray absorption spectroscopy. Chem. Mat., 2011, 23, 5415-5424.

17. H. S. Kim, Y. Kim, S. I. Kim, S. W. Martin, Enhanced electrochemical properties of $LiNi_{1/3}Co_{1/3}Mn_{1/3}O_2$ cathode material by coating with $LiAlO_2$ nanoparticles. J. Power Sources., 2006, 161, 623-627.

18. X. P. Zhang, S. W. Sun, Q. Wu, N. Wan, D. Pan, Y. Bai, Improved electrochemical and thermal performances of layered $Li[Li_{0.2}Ni_{0.17}Co_{0.07}Mn_{0.56}]O_2$ via $Li_2ZrO_3$ surface modification. J. Power Sources., 2015, 282, 378-384.

19. S. Ivanova, E. Zhecheva, D. Nihtianova, M. Mladenov, R. Stoyanova, Electrochemical intercalation of $Li^+$ into nanodomain $Li_4Mn_5O_{12}$. J. Alloys Compd., 2013, 561, 252-261.

20. J. Cao, J. Xie, G. Cao, T. Zhu, X. Zhao, S. Zhang, Electrochemical properties of $0.5Li_2MnO_3 \cdot 0.5Li_4Mn_5O_{12}$ nanotubes prepared by a self-templating method. Electrochim. Acta., 2013, 111, 447-454.

21. F. Wu, N. Li, Y. F. Su, L. J. Zhang, L. Y. Bao, J. Wang, L. Chen, Y. Zheng, L. Q. Dai, J. Y. Peng, S. Chen, Ultrathin spinel membrane-encapsulated layered lithium-rich cathode material for advanced Li-ion batteries. Nano Lett., 2014, 14, 3550-3555.

22. Q. B. Xia, X. F. Zhao, M. Q. Xu, Z. P. Ding, J. T. Liu, L. B. Chen, D. G. Ivey, W. F. Wei, A Li-rich layered@spinel@carbon heterostructured cathode material for high capacity and high rate lithium-ion batteries fabricated via an in situ synchronous carbonization-reduction method. J. Mater. Chem. A., 2015, 3, 3995-4003.

23. K. S. Lee, H. J. Bang, S. T. Myung, J. Prakash, K. Amine, Y. K. Sun, Synthesis and electrochemical properties of spherical spinel $Li_{1.05}M_{0.05}Mn_{1.9}O_4$ (M = Mg and Al) as a cathode material for lithium-ion batteries by co-precipitation method. J. Power Sources., 2007, 174, 726-729.

24. M. Hirayama, H. Ido, K. Kim, W. Cho, K. Tamura, J. Mizuki, R. Kanno, Dynamic Structural Changes at $LiMn_2O_4$/Electrolyte Interface during Lithium Battery Reaction. J. Am. Chem. Soc., 2010, 132, 15268-15276.

25. Z. Q. Xie, H. Eikhuemelo, J. Q. Zhao, C. Cain, W. W. Xu, Y. Wang, Ni and Fe dual-doped $Li_4Mn_5O_{12}$ spinels as cathode materials for high-voltage Li-ion batteriesJ. Electrochem. Soc., 2015, 162, A1523.

26. J. Q. Zhao, S. C. Ellis, Z. Q. Xie, Y. Wang, Facile synthesis of integrated layered-spinel composite cathode materials for high-voltage lithium-ion batteries up to 5.0 V", ChemElectroChem, 22, 1821-1829.

27. K. A. Kusters, S. E. Pratsinisap, S. G. Thorna, D. M. Smith, Energy-size reduction laws for ultrasonic fragmentation. Powder Technol., 1994, 80, 253-263.

28. M. D. Kass, Ultrasonically induced fragmentation and strain in alumina particles. Mater. Lett., 2000, 42, 246-250.

29. Y. Y. Huang, T. P. J. Knowles, E. M. Terentjev, Strength of nanotubes, filaments, and nanowires from sonication-induced scission. Adv. Mater., 2009, 21, 3945-3948.

30. T. Zhao, S. Chen, L. Li, X. Zhang, R. Chen, I. Belharouak, F. Wu, K. Amine, Synthesis, characterization, and electrochemistry of cathode material Li $[Li_{0.2}Co_{0.13}Ni_{0.13}Mn_{0.54}]O_2$ using organic chelating agents for lithium-ion batteries. J. Power Sources., 2013, 228, 206-213.

31. T. H. Cho, Y. Shiosaki, H. Noguchi, Preparation and characterization of layered $LiMn_{1/3}Ni_{1/3}Co_{1/3}O_2$ as a cathode material by an oxalate co-precipitation method. J. Power Sources., 2006, 159,1322-1327.

32. S. K. Martha, J. Nanda, G. M. Veith, N. J. Dudney, Electrochemical and rate performance study of high-voltage lithium-rich composition: $Li_{1.2}Mn_{0.525}Ni_{0.175}Co_{0.1}O_2$. J. Power Sources., 2012, 199, 220-226.

# CHAPTER 4. ONE-STEP SOLVOTHERMAL SYNTHESIS OF SN NANOPARTICLES DISPERSED IN TERNARY MANGANESE-NICKEL-COLBALT CARBONATE AS SUPERIOR ANODE MATERIALS FOR LITHIUM-ION BATTERIES*

## 4.1 Introduction

In the past decades, rechargeable lithium-ion batteries (LIBs) have been widely used as energy storage devices for portable electronic devices. However, the increasing demand for their emerging applications in hybrid electric vehicles (HEVs) and electric vehicles (EVs) requires us to develop LIBs with higher energy density and power density [1,2]. However, the theoretical capacity of common commercial graphite anode in current LIBs is only 372 mAh/g, limiting the energy and power of the LIBs [3]. Thus, it is imperative to explore alternative anode materials with higher reversible capacity and better rate capability, as well as long cycle life, low cost, and the potential for industrial scale production. In this context, pure metallic Sn has attracted considerable attention as an anode materials for LIBs due to its high theoretical specific capacity of ~994 mAh/g, corresponding to the formation of $Li_{22}Sn_5$ [4,5]. Nevertheless, its practical application is limited because Sn experiences a dramatic volume change of ~300% during the lithiation/delithiation processes, resulting in the pulverization of electrodes and fast fading in capacity [6-8]. The severe aggregation of Sn nanoparticles upon cycling also causes the capacity degradation of the Sn anode [9, 10].

In order to alleviate the problems mentioned above, two typical methods have been reported in literature. One approach is to reduce Sn particle size to nanoscale to efficiently mitigate the absolute strain induced by the large volume change during $Li^+$ insertion and

* This chapter previously appeared as Zhiqiang Xie, Jianqing Zhao and Ying Wang, "One-step solvothermal synthesis of Sn nanoparticles dispersed in ternary manganese-nickel-cobalt carbonate as superior anode materials for lithium ion batteries", Electrochim. Acta, 2015, 174, 1023–1029. It is reprinted by permission of Elsevier.

extraction processes [8,11-15]. However, the cycleability remains an issue because the Sn nanoparticles prefer to aggregate during cycling [9,16,17]. The other strategy is to design nanocomposites containing Sn and stress-accommodating carbon matrixes [15,18-23]. A variety of carbon matrixes have been used, such as amorphous carbon [23-28], ordered mesoporous carbon (OMC) [17], graphite [25,29,30], singe-walled carbon nanotubes (SWNTs) [31,32], multi-walled carbon nanotubes (MWNTs) [33-35], carbon nanofibers [36]. However, the synthesis process of most Sn/C composites mentioned above usually involve multiple steps and high temperature annealing which are not practical for large scale production for commercialization.

Recently, transition metal carbonates $MCO_3$ (M=Mn. Co, Ni, etc.) as a new family of anode materials in LIBs have been reported to have much higher reversible capacities than graphite and better cycling performances than bare Sn [37-41]. In addition, these materials can be synthesized using a cost-effective one-step low-temperature process without further treatment [41,43,44]. The lithium storage mechanism of $MCO_3$ can be explained via a reversible conversion reaction as follows [40]:

$$MCO_3 + 2Li^+ + 2e^- \leftrightarrow M + Li_2CO_3 \quad (1)$$

Theoretical capacities of carbonate anodes can be calculated using the reversible reaction (1). For example, theoretical capacities of $MnCO_3$, $CoCO_3$ and $NiCO_3$ are determined as 466, 451 and 451 mAh/g, respectively. It is interesting to note that transition metal carbonates as anode materials have always demonstrated much higher practical capacity than its theoretical value. For example, Tirado's group reported that submicron $MnCO_3$ particles delivered an initial reversible capacity of 750 mAh/g higher than its theoretical capacity of 466 mAh/g. The cited authors ascribed the extra capacity to "non-faradic contribution" or "pseudocapacitance" [39,44]. Recently, it was found that partial cobalt substitution in $MnCO_3$ was favorable for lithium storage and showed enhanced cycling performance at higher rates in comparison with

pure $MnCO_3$ [45]. However, cycling performances of transition metal carbonates need improvements for practical application in lithium ion batteries. For instance, it has been found that $MnCO_3$ submicrometric particles only retained ~450 mAh/g after 25 cycles due to the low electronic conductivity of carbonates and large volume changes during repeated cycles [44].

In this regard, our group has lately reported synthesis of a new ternary manganese-nickel-cobalt carbonate $Mn_{0.54}$ $Ni_{0.13}$ $Co_{0.13}$ $(CO_3)_{0.8}$ ($MNCCO_3$) via a one-step low-temperature solvothermal route for application as LIB anode, which has demonstrated an unexpectedly high initial charge capacity of 1173.1 mAh/g at a specific current of 25 mA/g. When cycled at 250 mA/g, $MNCCO_3$ anode retains a final specific capacity of 434 mAh/g after 100 electrochemical cycles [41], indicating a significantly enhanced cycling stability in comparison with other pure carbonates or binary carbonates. However, due to the poor electronic conductivity, cycling stability and rate performance of transition metal carbonates are not sufficient for applications in new-generation LIBs.

In the present work, to combine all the merits and enhance electrochemical properties of both Sn and ternary carbonate $MNCCO_3$, we design and synthesize a novel structure with Sn nanoparticles well-dispersed in the microspheres of $MNCCO_3$ (Sn@$MNCCO_3$) using a facile one-step solvothermal process. In this Sn@$MNCCO_3$ composite, both Sn and $MNCCO_3$ provide a high reversible capacity. It is also expected that the well-dispersed Sn nanoparticles will enhance the electronic conductivity of the overall electrode, while $MNCCO_3$ serves as a matrix to buffer against the huge volume changes of Sn nanoparticles in the composite. To the best of our knowledge, this work is the first effort to explore its lithium storage performance for application as anode in lithium ion batteries. Moreover, Sn content can be optimized for maximized battery performance. The Sn@$MNCCO_3$ composite with the optimal 10 wt% Sn shows a highly reversible specific capacity, excellent cycling stability and

significantly improved rate capability profiting from the synergic effect of the components in the composite.

## 4.2 Experimental Section

### 4.2.1 Synthesis of bare $Mn_{0.54}Ni_{0.13}Co_{0.13}(CO_3)_{0.8}$ and Sn@$MNCCO_3$ composite

As reported in our previous work [41], base material $Mn_{0.54}Ni_{0.13}Co_{0.13}(CO_3)_{0.8}$ carbonates (denoted as $MNCCO_3$) were first synthesized using a solvothermal route. Six mmol transition metal acetates (a molar ratio of $Mn^{2+}$ : $Ni^{2+}$: $Co^{2+}$ = 0.54 : 0.13 : 0.13) were dissolved in 10 ml ethylene glycol under continuous stirring at 40°C for half an hour, followed by adding 22.5 mmol urea as the precipitant. Additional solvent was replenished to form a 15 ml solution in total. Afterwards, the resultant solution was transferred into a 23 ml Teflon container and placed within a sealed stainless steel autoclave. Heat treatment of the autoclave was carried out in an oven at 200 °C for 20 hours. After cooling down to room temperature, the resultant powders were centrifuged and washed with distilled water at least three times and were collected after drying at 120 ºC in vacuum overnight.

In order to obtain Sn nanoparticles embedded in $Mn_{0.54}Ni_{0.13}Co_{0.13}(CO_3)_{0.8}$ (denoted as Sn@$MNCCO_3$), different amount of Sn nanoparticles (60-80nm, US Research Nanomaterials, Inc) ranging from 5 to 25 wt.% were directly added in the ethylene glycol solvent together with transition metal acetates and urea for the same solvothermal process.

### 4.2.2 Material characterizations.

The morphology and size of the as-prepared composite materials were analyzed using a FEI Quanta 3D FEG field emission scanning electron microscope (FESEM). The as-prepared samples were also characterized by X-ray diffraction (XRD) using a Rigaku MiniFlex X-ray diffractometer with Cu $K_a$ radiation at a scan rate of $2^{\circ}\,min^{-1}$. EDS mapping has been acquired at L-edge of Sn.

4.2.3 Electrochemical measurements

Electrochemical measurements of the anode materials were performed in the 2032 type coin cells with lithium metal as the counter electrode at room temperature. The anode was prepared by coating a slurry of 70 wt.% active materials, 20 wt.% acetylene black (conductive carbon, Alfa Aesar) and 10 wt.% polyvinylidene fluoride (PVDF, Alfa Aesar) onto a Cu foil substrate. Prior to use, the electrodes were dried under vacuum at 120ºC overnight and then pressed to enhance the contact between the active materials and the conductive carbon. The electrolyte was 1 M $LiPF_6$ dissolved in ethylene carbonate (EG), dimethyl carbonate (DMC) and diethyl carbonate (DEC) at a volumetric ratio of 1:1:1. The electrodes were assembled in an argon-filled glove box. Electrochemical performance of the sample was tested at various *C* rates in a voltage range of 0.01-3.0 V using an 8-channel battery analyzer (MTI Corporation). All the measurements were carried out at room temperature and all potentials are given *vs.* the $Li/Li^+$ semi-couple.

**4.3 Results and Discussion**

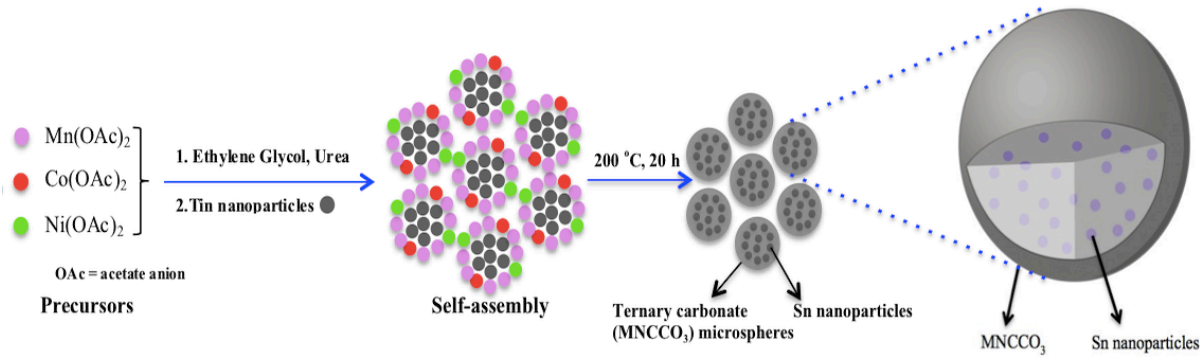


Figure 4.1 Schematic showing synthesis of Sn@MNCCO3 composite via a one-step solvothermal process.

Figure 4.1 presents a schematic illustrating the one-step solvothermal synthesis of $Sn@MNCCO_3$ composite. As reported in our previous work [41], due to the similar polarity between ethylene glycol (EG) and acetate anions ($CH_3COO^-$) of transition metal precursors,

EG-based solvothermal reaction can induce self-assembly of transition metal cations and acetate anions, resulting in the final spherical structure of $MNCCO_3$ mater. In this case, Sn nanoparticles tend to be encapsulated within the spherical colloids formed by transition-metal acetate precursors, in order to drastically reduce surface energy of the reactants. In the subsequent co-precipitation process, decomposition of urea releases $CO_3^{2-}$ anions which then react with $M^{2+}$ (M=Mn, Ni, Co) to produce a ternary manganese-nickel-cobalt carbonate compound when treated at 200 ºC for 20 hours in the autoclave, while Sn nanoparticles are restricted within $MNCCO_3$ spheres. As a result, the spherical structure of $Sn@MNCCO_3$ composite is achieved, in which the Sn nanoparticles are dispersed throughout the $MNCCO_3$ matrix.

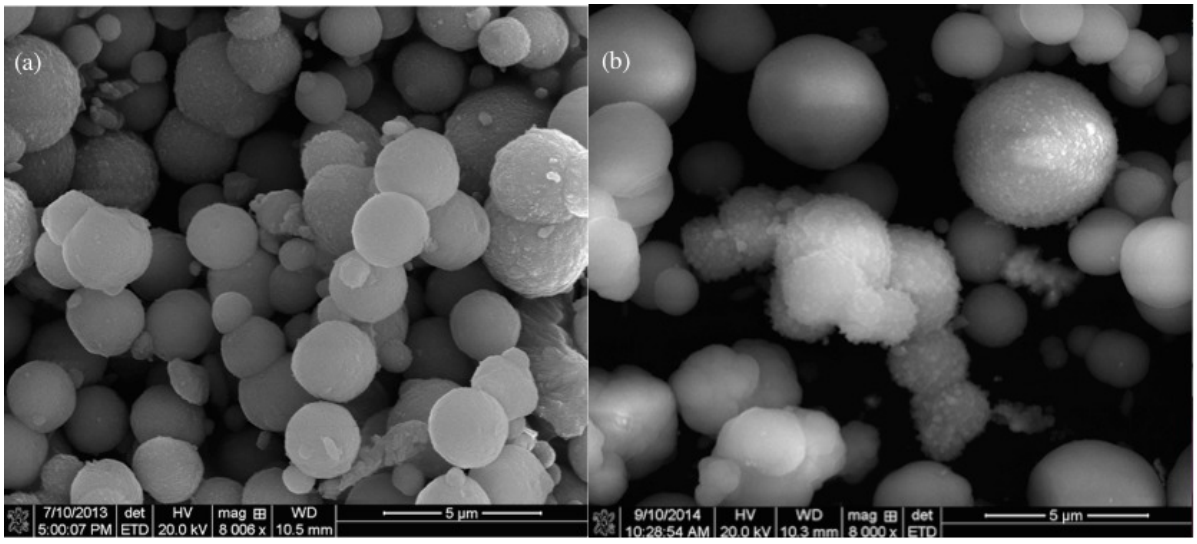


Figure 4.2 SEM images of (a) bare $MNCCO_3$ and (b) $10Sn@MNCCO_3$ composite (the composite with 10 wt.% Sn nanoparticles dispersed in $MNCCO_3$ matrix).

Figure 4.2a and b show typical SEM images of bare $MNCCO_3$ and $Sn@MNCCO_3$ composites synthesized by the facile one-step solvothermal route. It is seen that bare $MNCCO_3$ is composed of relatively smooth solid spheres with a size from 2.5 µm to 5 µm and the composite $Sn@MNCCO_3$ maintains the similar structure and morphology. However, it is found that Sn nanoparticles are located on some of the external areas of $Sn@MNCCO_3$, possibly Sn nanoparticles tend to aggregate due to their high surface area.

To identify the novel structure of Sn nanoparticles embedded in micro-meter spheres of ternary manganese-nickel-cobalt carbonate, focused ion beam (FIB) milling and SEM imaging were performed and then the cross-sectional elemental composition was analyzed by EDS mapping. Figure 4.3a and b show the SEM images 10Sn@$MNCCO_3$ sample before and after FIB milling. As seen in Figure 4.3b, part of a selected sphere (~4um) was removed by FIB milling. The sample after FIB milling was tilted to further analyze the cross-sectional feature (as shown in Figure 4.3c). Based on EDS mapping results, Mn, Ni, Co O and C elements were distributed homogeneously in selected micro-meter spheres (as presented in Figure 4.3d-h), revealing well-synthesized ternary carbonate matrix. It is worth noting that Figure. 3i shows the Sn element also has a homogeneous distribution in the cross-section of the selected micro-meter sphere, suggesting the well-dispersed Sn nanoparticles within the ternary carbonate matrix. In addition, EDS mapping results show that ~9 wt.% of Sn exists in the 10Sn@$MNCCO_3$ sample, which is close to its nominal amount. This novel structure of Sn nanoparticles embedded in $MNCCO_3$ is expected to be a very promising anode material for application in lithium ion batteries. The confinement of Sn nanoparticles inside the $MNCCO_3$ matrix can counteract the huge volume expansion during charge and discharge processes, which is one of the main reasons for leading to anode degradation and poor electrochemical cycle life.

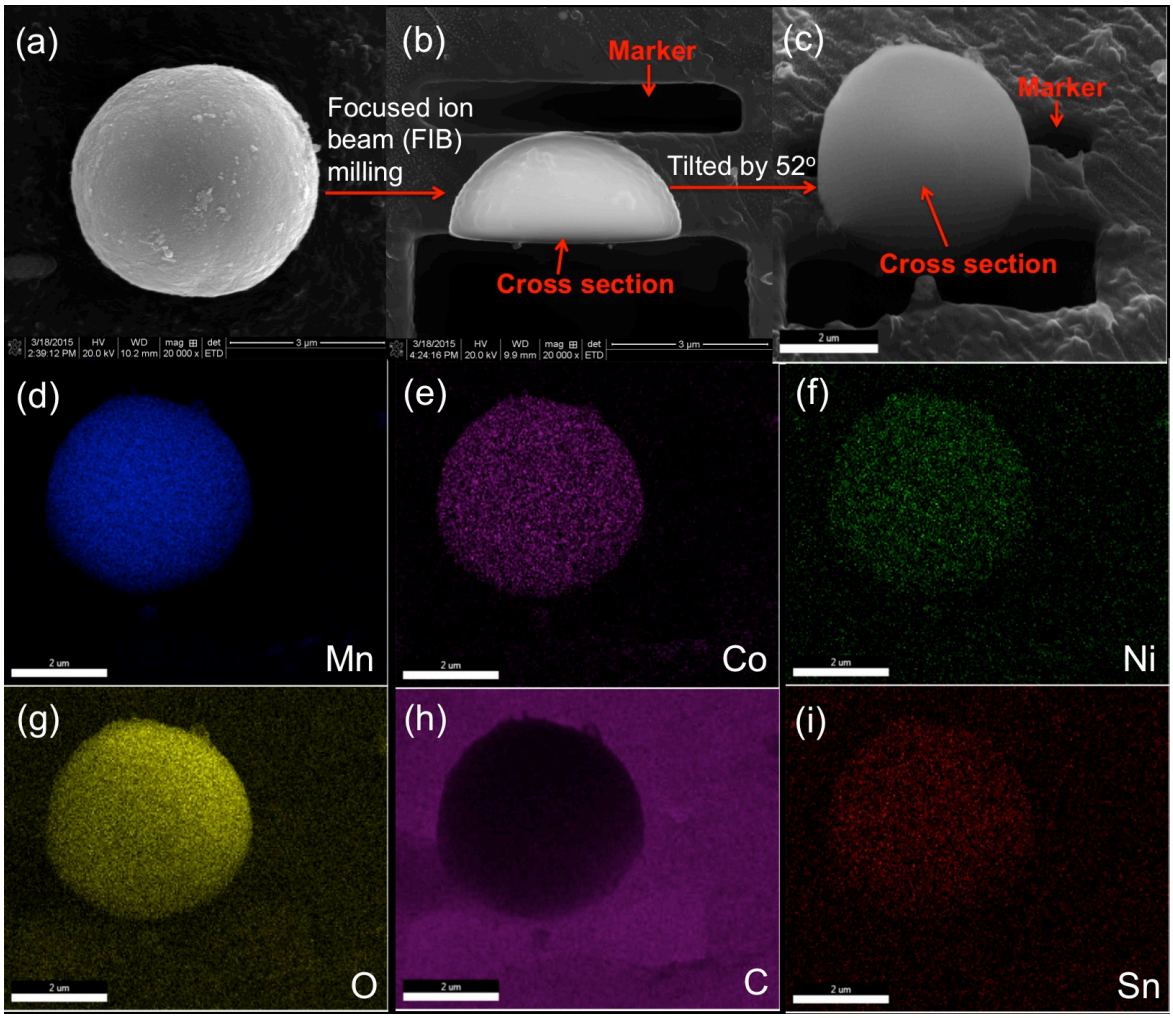


Figure 4.3 SEM images of (a) 10Sn@MNCCO$_3$ before FIB milling, (b) sample after FIB milling (marker shown here is used as a reference), (c) sample at 52$^o$ tilt, (d-i) elemental maps of Mn, Co, Ni, O, C and Sn, respectively.

Figure 4.4 shows XRD patterns of the as-prepared Sn@MNCCO$_3$ composites with various amount of Sn nanoparticles and bare MNCCO$_3$ . All the major XRD peaks of bare MNCCO$_3$ can be indexed to rhodochrosite MnCO$_3$, but we notice the peaks have slight shifts to the higher diffraction angle due to nominal cobalt and nickel substitutions. The XRD patterns of 5Sn@MNCCO$_3$ and 10Sn@MNCCO$_3$ composites reveal, as main features, peaks that can be indexed to rhodochrosite MnCO$_3$ and metallic Sn, suggesting the formation of the Sn@MNCCO$_3$ heterostructures. However, with the increase of Sn amount from 15 to 25 wt.%

in the composite, the strong peaks from SnO are evidenced as well, which can be explained as follows. (*i*) The commercial Sn nanoparticles used in this work are not pure Sn but with a low fraction of SnO, as indicated in the XRD result of bare Sn; (*ii*) Sn particles that are not embedded and protected inside $MNCCO_3$ microspheres may be oxidized to SnO due to exposure to air during the sample handling.

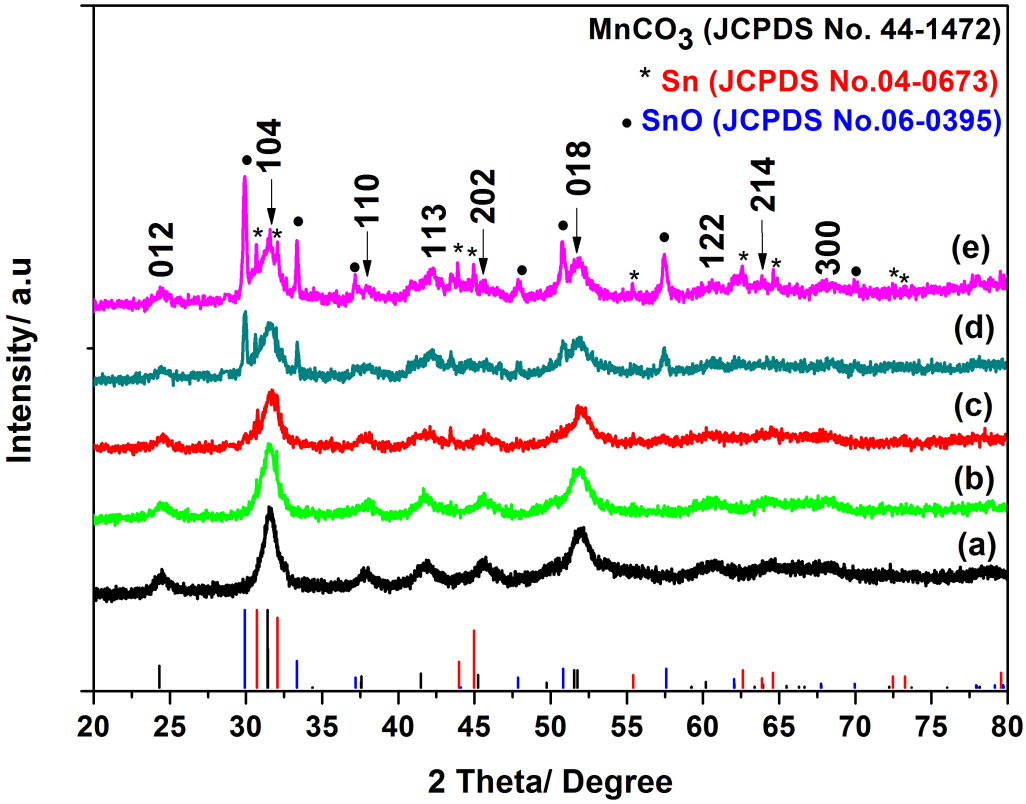


Figure 4.4 XRD patterns of (a) $MNCCO_3$, (b) 5Sn@$MNCCO_3$, (c) 10Sn@$MNCCO_3$, (d) 15Sn@$MNCCO_3$, (e) 25Sn@$MNCCO_3$. The standard XRD peaks of $MnCO_3$, metallic Sn and SnO are also presented.

In order to study the effects of the amount of Sn loading on the electrochemical performance of Sn@$MNCCO_3$ composites, Sn@$MNCCO_3$ /Li half cells are assembled to investigate electrochemical performance in a voltage range of 0.01-3.0 V *vs*. $Li/Li^+$ (see details in experimental section). Figure 4.5a compares cycling performances of the as-

prepared Sn@$MNCCO_3$ composites with various Sn loading amounts. For comparison purpose, the as-received Sn nanoparticles and bare ternary carbonate $MNCCO_3$ are also examined under the same conditions. Bare Sn nanoparticles show a high initial charge capacity of 973 mAh/g, which is close to its theoretical capacity of 994 mAh/g, but rapid capacity fading is observed due to the drastic volume changes upon cycling, thereby leading to severe pulverization of Sn particles. Such poor cycleability of Sn has also been reported in literature [9,10]. As for bare ternary manganese-nickel-cobalt carbonate $MNCCO_3$, it delivers an initial charge capacity of ~828 mAh/g, almost doubling its theoretical capacity of 461 mAh/g [41]. The extra electrochemical capacity may be attributed to non-faradic capacity [44] and reversible formation/dissolution of gel-like polymer film on the surface of ternary carbonate $MNCCO_3$ [42]. Additionally, it is found that Sn loading amount has a significant effect on electrochemical performance of the as-prepared Sn@$MNCCO_3$ composite. It can be seen that the composite with 10 wt.% Sn (10Sn@$MNCCO_3$) delivers the highest charge capacity of ~560 mAh/g after 100 cycles, as the composite exhibits a significant improvement in charge capacity with the increase of the Sn content from 5 to 10 wt.% and then decreases dramatically with the Sn content increased from 15 to 25 wt.%. The initial increase in the charge capacity can be expected due to the increased reaction between tin and lithium. However, increasing Sn content beyond 10 wt.% may result in aggregation of Sn nanoparticles outside $MNCCO_3$ microspheres, leading to fast fading in capacity, which is evidenced by the SEM results. It is noted that 10Sn@$MNCCO_3$ composite shows a final charge capacity that is 176 mAh/g higher than that of bare $MNCCO_3$ after 100 cycles. The 10 wt.% Sn is expected to contribute a capacity of 99.4 mAh/g to the composite at most, since the theoretical specific capacity of Sn is 994 mAh/g. Therefore, the enhanced electrochemical performance is ascribed to the structure of Sn nanoparticles well dispersed in $MNCCO_3$ microspheres, which is not only fully utilized to store lithium ions to provide higher capacity,

but also offers better electronic conductivity to enhance cycling stability of $MNCCO_3$ matrix in the composite.

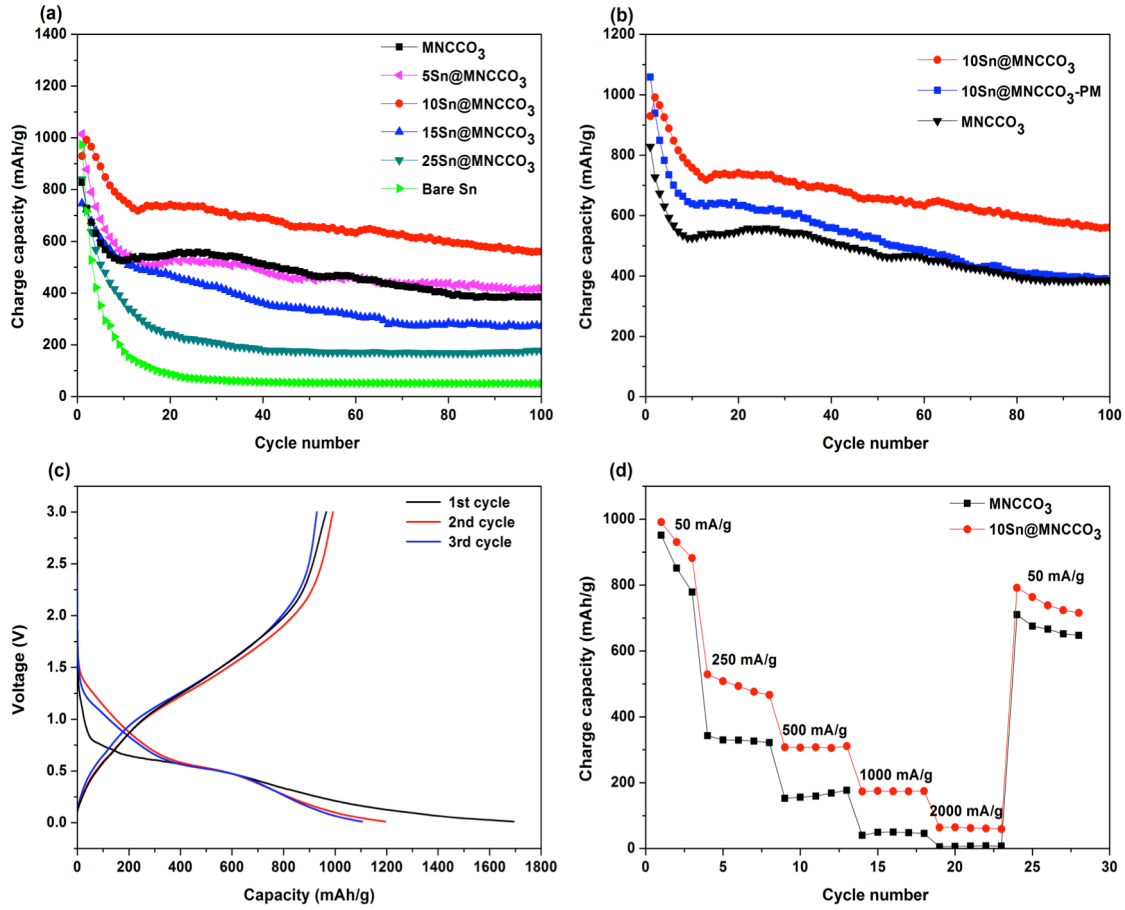


Figure 4.5 (a) Cycling performances of $Sn@MNCCO_3$ composites with various Sn content cycled at a specific current of 100 mA/g in a voltage window of 0.01-3.0 V *vs.* $Li/Li^+$. (b) Cycling performances of $10Sn@MNCCO_3$ (the composite with 10 wt.% Sn) obtained via solvothermal method, $10Sn@MNCCO_3$-PM (physical mixture of $MNCCO_3$ and 10 wt.% Sn), and the base material $MNCCO_3$. (c) Charge and discharge profiles of $10Sn@MNCCO_3$ composite in the first three cycles at a specific current of 100 mA/g. (d) Rate performances of $10Sn@MNCCO_3$ and bare $MNCCO_3$ at various specific currents.

To further explore the effectiveness of the one-step solvothermal synthesis of Sn@$MNCCO_3$ composite, the sample with 10 wt.% Sn physically mixed with base material $MNCCO_3$ (10Sn@$MNCCO_3$–PM) is electrochemically evaluated under the same conditions for comparison purpose, and its cycling performance is presented in Figure 4.5b. The sample of 10Sn@$MNCCO_3$-PM exhibits a higher charge capacity than the base material $MNCCO_3$, but rapid capacity fading is observed and shows a similar cycling performance with the base material $MNCCO_3$ after 60 cycles, retaining 524 mAh/g after 50 cycles and 386 mAh/g after 100 cycles. In contrast, 10Sn@$MNCCO_3$ synthesized via a solvothermal approach displays much better cycling stability and capacity retention (657 mAh/g after 50 cycles, 560 mAh/g after 100 cycles), suggesting that Sn nanoparticles well dispersed in $MNCCO_3$ microspheres via a facile solvothermal route leads to better utilization of Sn nanoparticles for the enhanced electrochemical performance compared to the simple physical mixture.

Figure 4.5c shows typical charge/discharge profiles of the as-prepared 10Sn@$MNCCO_3$ composite in the initial three cycles at a specific current of 100 mA/g. The 10Sn@$MNCCO_3$ composite displays high initial discharge and charge capacities of ~1700 mAh/g and ~929 mAh/g, respectively. The large irreversible capacity loss in the first cycle is mainly attributed to the formation of the solid-electrolyte interphase (SEI) film on the surface of the electrodes. However, the improved reversibility is observed in subsequent second and third cycles. In addition to cycleability, the rate performance of 10Sn@$MNCCO_3$ composite is investigated as well. Figure 4d shows the distinctly enhanced rate performance compared to bare $MNCCO_3$. As we can see in Figure 4.5d, the charge capacity of 10Sn@$MNCCO_3$ decreases from a value of 991 mAh/g when cycled at 50 mA/g to 64 mAh/g at 2000 mA/g with the increasing specific current. When the specific current returns from 2000 mA/g to 50 mA/g, 10Sn@$MNCCO_3$ retains a high capacity of 791 mAh/g, indicating the outstanding electrochemical reversibility.

To further explore electrochemical reactions during charge/discharge cycling, cyclic voltammograms (CV) of the Sn@$MNCCO_3$ composites with various Sn amounts, $MNCCO_3$ and bare Sn anodes are presented in Figure 4.6. As shown in Figure 4.6a, there are two narrow reduction peaks and two broad oxidation peaks in the first cycle for the bare $MNCCO_3$. The first narrow reduction peak occurs at ~0.8 V, corresponding to the electrolyte decomposition and formation of solid electrolyte interface (SEI) film on the surface of bare $MNCCO_3$ anode [19,21]. The second broad reduction peak below 0.5 V can be ascribed to the combined effects from formation of the SEI film, reduction of transition metal ions ($M^{2+}$, M=Mn, Co and Ni) to metallic $M^0$ and discharge reaction of the as-formed gel-like polymer on the surface of the carbonate anode [42]. It is found that the current intensity of this peak considerably deceases in subsequent cycles, which can be attributed to the fact that the SEI film mainly grows in the initial discharge. Correspondingly, the oxidation peaks centered on ~1.50 V can be attributed to oxidation of metallic transition metal $M^o$ and charge reaction of gel-like polymer, respectively [42]. Figure 4.6f shows the typical CV curves of bare Sn nanoparticles. The reduction peaks at ~0.30 and 0.60 V can be ascribed to the alloying reaction between lithium and Sn, and four separated oxidation peaks occur at 0.40-0.90 V, which are associated with the extraction of Li from Sn [46]. For the 10Sn@$MNCCO_3$ composite (as shown in Figure 4.6c), the first broad reduction peak in the first CV cycle is shown in the range of 0.01 - 0.8 V, which may be attributed to the formation of SEI film on the surface of anode and lithium alloying reaction in tin nanoparticles ($Li_xSn$). Due to the overlapping of these steps, they are not distinguishable in the related CV peaks. The second broad reduction peak occurs at 1.25 V, corresponding to reduction of transition metal ions ($M^{2+}$, M=Mn , Co and Ni) to metallic state $M^o$. Whereas, two broad oxidation peaks occur at 0.65 and 1.45 V, corresponding to delithiation of $Li_xSn$ alloys and oxidation of $M^o$, respectively. For comparison purpose, the CV curves of 5Sn@$MNCCO_3$ 15Sn@$MNCCO_3$

and 25Sn@$MNCCO_3$ are also presented in Figure 4.6b, d and e. It is found that the oxidation peak at ~ 0.65 V becomes stronger gradually with the increase of Sn amount from 5 to 25 wt.% in composites, which is in good accordance with the XRD results.

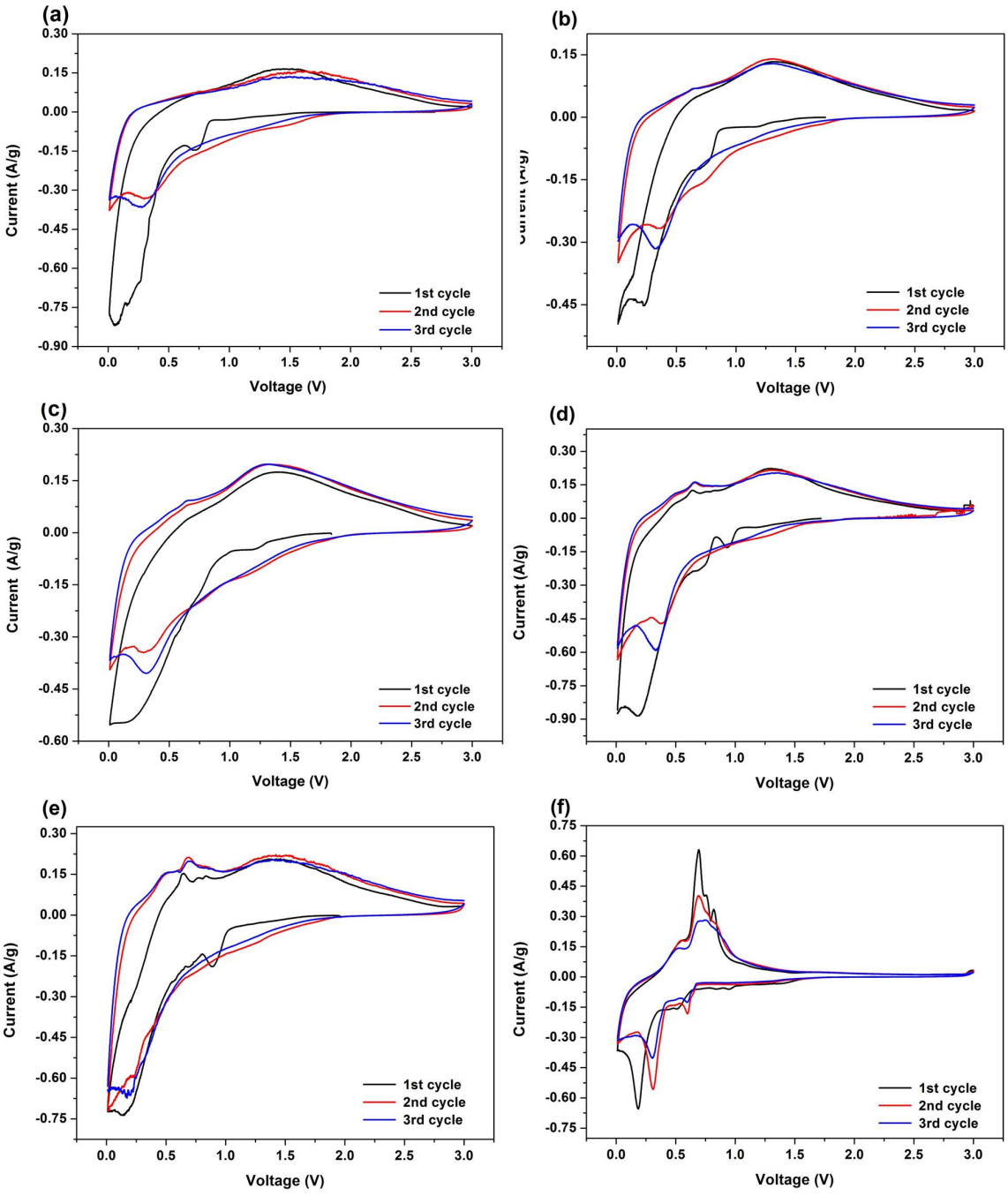


Figure 4.6 Cyclic voltammograms of (a) bare $MNCCO_3$, (b) 5Sn@$MNCCO_3$ (the composite with 5 wt.% Sn), (c) 10Sn@$MNCCO_3$, (d) 15Sn@$MNCCO_3$, (e) 25Sn@$MNCCO_3$, and (f) bare Sn in the first three cycles at a scan rate of 0.1 mV/s.

The enhanced electrochemical performance of 10Sn@$MNCCO_3$ composite can be attributed to its unique structure of Sn nanoparticles well dispersed within the ternary carbonate matrix. First, both Sn and ternary carbonate $MNCCO_3$ possess high reversible capacities, which are combined to result in a high capacity for the 10Sn@$MNCCO_3$ composite. Second, $MNCCO_3$ matrix can efficiently buffer against the huge volume changes of metallic Sn particles, ensuring Sn can be fully utilized for lithium storage. Finally, well-dispersed Sn nanoparticles in the composite have a high electronic conductivity, and thus help to preserve the good electrical contact of the overall electrode during electrochemical cycling, leading to the enhanced rate performance.

**4.4 Conclusions**

We report facile one-step low-temperature synthesis of novel Sn@$MNCCO_3$ composite with tin nanoparticles well dispersed in ternary manganese-nickel-cobalt $Mn_{0.54}$ $Ni_{0.13}$ $Co_{0.13}$ $(CO_3)_{0.8}$. It is found that Sn content can be optimized for maximized electrochemical performance of the composite. With the optimal 10 wt.% Sn content, the Sn@$MNCCO_3$ composite demonstrates excellent electrochemical properties such as a high initial charge capacity of 929 mAh/g at a specific current of 100 mA/g, as well as improved cycling stability and rate capability in comparison with bare ternary carbonate $MNCCO_3$, bare Sn nanoparticles, and physical mixture of $MNCCO_3$ with 10 wt.% Sn, due to enhanced electronic conductivity caused by Sn and more flexible volume change during Li ion intercalation/deintercalation processes provided by the carbonate matrix. Therefore, Sn@$MNCCO_3$ composite is a promising alternative anode material for application in new-generation high-performance lithium ion batteries.

## 4.5 References


1. Y. H. Xu, Q. Liu, Y. J. Zhu, Y. H. Liu, A. Langrock, M. R. Zachariah, C. S. Wang, Uniform nano-Sn/C composite anodes for lithium ion batteries. Nano Lett., 2013, 13, 470-474.

2. B. Wang, X. L Li, X. F. Zhang, B. Luo, M. H. Jin, M. H. Liang, Shadi A. Dayeh, S. T. Picraux, L. J. Zhi, Adaptable silicon–carbon nanocables sandwiched between reduced graphene oxide sheets as lithium ion battery anodes. ACS Nano, 2013, 7, 1437-1445.

3. C. N. He, S. Wu, N. Q. Zhao, C. S. Shi, E. Z. Liu, J. J. Li, Carbon-encapsulated $Fe_3O_4$ nanoparticles as a high-rate lithium ion battery anode material. ACS Nano, 2013, 7, 4459-4469.

4. M. Winter, J. O. Besenhard, Electrochemical lithiation of tin and tin-based intermetallics and composites. Electrochim. Acta, 1999, 45, 31-50.

5. M. Wachtler, J. O. Besenhard, M. Winter, Tin and tin-based intermetallics as new anode materials for lithium-ion cells. J. Power Sources, 2001, 94, 189-193.

6. O. Mao, R. A. Dunlap, J. R. Dahn, Mechanically alloyed Sn-Fe (-C) powders as anode materials for Li-Ion batteries: I. the Sn2Fe-C system, J. Electrochem. Soc., 1999,146, 405-413.

7. H. Li, L. Shi, W. Lu, X. Huang, L. Chen, Studies on capacity loss and capacity fading of nanosized SnSb alloy anode for Li-ion batteries. J. Electrochem. Soc., 2001, 148, 915-922.

8. B. Wang, B. Luo, X. L. Li, L. J. Zhi, The dimensionality of Sn anodes in Li-ion batteries. Mater. Today, 2012, 15, 544-552.

9. I. A. Courtney, W. McKinnon, J. Dahn, On the aggregation of tin in SnO composite glasses caused by the reversible reaction with lithium. J. Electrochem. Soc., 1999, 146, 59–68.

10. K. T. Lee, Y. S. Jung, S. M. Oh, Synthesis of tin-encapsulated spherical hollow carbon for anode material in lithium secondary batteries. J. Am. Chem. Soc., 2003, 125 5652-5653.

11. A. R. Kamali, D. J. Fray, Tin-based materials as advanced anode materials for lithium ion batteries: a review. Rev. Adv. Mater.Sci., 2011, 27, 14-24.

12. J. S. Chen, X. W. Lou, $SnO_2$ and $TiO_2$ nanosheets for lithium-ion batteries. Mater. Today, 2012, 15, 246-254.

13. Y. Wang, J. Y. Lee, T. C. Deivaraj, Tin nanoparticle loaded graphite anodes for Li-ion battery applications. J. Electrochem. Soc., 2004, 151, 1804-1809.

14. G. Derrien, J. Hassoun, S. Panero, B. Scrosati, Nanostructured Sn–C composite as an advanced anode material in high-performance lithium-ion batteries. Adv. Mater., 2007, 19, 2336-2340.

15. J. Hassoun, G. Derrien, S. Panero, B. Scrosati, A nanostructured Sn–C composite lithium battery electrode with unique stability and high electrochemical performance. Adv. Mater., 2008, 20, 3169-3175.

16. G. X. Wang, B. Wang, X. L. Wang, J. Park, S. X. Dou, H. Ahn, K. Kim, Sn/graphene nanocomposite with 3D architecture for enhanced reversible lithium storage in lithium ion batteries. J Mater Chem., 2009, 19, 8378-8384.

17. J. K. Hwang, S. H. Woo, J. M. Shim, C. S. Jo, K. T. Lee, J. W. Lee, One-pot synthesis of tin-embedded carbon/silica nanocomposites for anode materials in lithium-ion batteries. ACS Nano, 2013, 7, 1036-1044.

18. M. Egashira, H. Takatsuji, S. Okada, J. Yamaki, Properties of containing Sn nanoparticles activated carbon fiber for a negative electrode in lithium batteries. J. Power Sources, 2002, 107, 56-60.
19. G. Wang, Y. Q. Ma, Z. Y. Liu, J. N. Wu, Novel highly porous Sn–C composite as high performance anode material for lithium-ion batteries. Electrochim. Acta, 2012, 65, 275-279.

20. Y. S. Jung, K. T. Lee, J. H. Ryu, D. Im, S. M. Oh, Sn-carbon core-shell powder for anode in lithium secondary batteries. J. Electrochem. Soc., 2005, 152, 1452-1457.

21. X. Xia, X. Wang, H. M. Zhou, X. Niu, L. G. Xue, X. W. Zhang, Q. F. Wei, The effects of electrospinning parameters on coaxial Sn/C nanofibers: morphology and lithium storage performance. Electrochim. Acta, 2014, 121 345-351.

22. Y. Yu, L. Gu, C. Zhu, P. A. van Aken, J. Maier, Tin nanoparticles encapsulated in porous multichannel carbon microtubes: preparation by single-nozzle electrospinning and application as anode material for high-performance Li-based batteries. J. Am. Chem. Soc., 2009, 131, 15984-15985.

23. Y. Yu, L. Gu, C. Wang, A. Dhanabalan, P.A. van Aken, J. Maier, Encapsulation of Sn@carbon nanoparticles in bamboo-like hollow carbon nanofibers as an anode material in lithium-based batteries. Angew. Chem., Int. Ed., 2009, 48, 6485-6489.

24. S. H. Lee, M. Mathews, H. Toghiani, D. O. Wipf, C. U. Pittman, Fabrication of carbon-encapsulated mono-and bimetallic (Sn and Sn/Sb Alloy) nanorods. Potential lithium-ion battery anode materials. Chem. Mat., 2009, 21, 2306-2314.

25. J. Park, J. Y. Eom, H. Kwon, Fabrication of Sn–C composite electrodes by electrodeposition and their cycle performance for Li-ion batteries. Electrochem. Commun., 2009, 11, 596-598.

26. Z. W. Zhao, Z. P. Guo, P. Yao, H. K. Liu, Mesoporous carbon-tin nanocomposites as anode materials for Li-ion battery. J. Mat. Sci. Technol., 2008, 24, 657-660.

27. T. Morishita, T. Hirabayashi, T. Okuni, N. Ota, M. Inagaki, Preparation of carbon-coated Sn powders and their loading onto graphite flakes for lithium ion secondary battery. J. Power Sources, 2006, 160, 638-642.

28. M. Marcinek, L. J. Hardwick, T. J. Richardson, X. Song, R. Kostecki, Microwave plasma chemical vapor deposition of nano-structured Sn/C composite thin-film anodes for Li-ion batteries. J. Power Sources, 2007, 173, 965-971.

29. K. Wang, X. He, J. Ren, C. Jiang, C. Wan, Ball milling of graphite/tin composite anode materials in a liquid medium. J. New Mater. Electrochem. Syst., 2007, 10, 167-170.

30. L. Z. Zhao, S. J. Hu, Q. Ru, W. S. Li, X. H. Hou, R. H. Zeng, D. S. Lu, Effects of graphite on electrochemical performance of Sn/C composite thin film anodes. J. Power Sources, 2008, 184, 481-484.

31. J. W. Zheng, S. M. L. Nai, M. F. Ng, P. Wu, J. Wei, M. Gupta, DFT study on nano structures of Sn/CNT complex for potential Li-ion battery application. J. Phys. Chem., 2009, 113, 14015-14019.

32. Y. Wang, M. Wu, Z. Jiao, J. Y. Lee, Sn@CNT and Sn@C@CNT nanostructures for superior reversible lithium ion storage. Chem. Mat., 2009, 21, 3210-3215.

33. K. Z. Lin, X. L. Wang, Y. H. Xu, J. Wuhan University of Technology - Mater. Sci. Ed., 2006, 21, 60-63.

34. W. X. Chen, J. Y. Lee, Z. Liu, The nanocomposites of carbon nanotube with Sb and $SnSb_{0.5}$ as Li-ion battery anodes. Carbon, 2003, 41, 959-966.

35. U. Tocoglu, O. Cevher, M. O. Guler, H. Akbulut, Core–shell tin-multi walled carbon nanotube composite anodes for lithium ion batteries. Int J. of Hydrogen Energy, 2014, 39, 21386-21390.

36. Y. H. Yu, Q. Yang, D. H. Teng, X. P. Yang, S. K. Ryu, Reticular Sn nanoparticle-dispersed PAN-based carbon nanofibers for anode material in rechargeable lithium-ion batteries. Electrochem. Commun., 2010, 12, 1187-1190.

37. L. Y. Shao, R. Ma, K. Q. Wu, M. Shui, M. M. Lao, D. J. Wang, N. B. Long, Y. L. Ren, J. Shu, Metal carbonates as anode materials for lithium ion batteries. J. Alloy. Compd., 2013, 581, 602-609.

38. L. W. Su, Z. Zhou, X. Qin, Q. W. Tang, D. H. Wu, P. W. Shen, $CoCO_3$ submicrocube/graphene composites with high lithium storage capability. Nano Energy, 2013, 2, 276-282.

39. M. J. Arago´n, C. Pe´rez-Vicente, J. L. Tirado, Submicronic particles of manganese carbonate prepared in reverse micelles: A new electrode material for lithium-ion batteries. Electrochem. Commun., 2007, 9, 1744-1748.

40. Y. R. Zhong, L. W. Su, M. Yang, J. P. Wei, Z. Zhou, Rambutan-like $FeCO_3$ hollow microspheres: facile preparation and superior lithium storage performances. Appl. Mater. Interfaces, 2013, 5, 11212-11217.

41. J. Q. Zhao, Y. Wang, High-capacity full lithium-ion cells based on nanoarchitectured ternary manganese–nickel–cobalt carbonate and its lithiated derivative. J. Mater. Chem. A, 2014, 2, 14947-14956.

42. S. Laruelle, S. Grugeon, P. Poizot, M. Doll´e, L. Dupont, J. M. Tarascon, On the origin of the extra electrochemical capacity displayed by MO/Li cells at low potential. J. Electrochem. Soc., 2002, 149, 627-634.

43. S. Xuan, M. Chen, L. Hao, W. Jiang, X. Gong, Y. Hu, Z. Chen, Preparation and characterization of microsized $FeCO_3$, $Fe_3O_4$ and $Fe_2O_3$ with ellipsoidal morphology. J. Magn. Magn. Mater., 2008, 320, 164-170.

44. M. J. Aragón, B. León, C. Perez Vicente, J. L. Tirado, A new form of manganese carbonate for the negative electrode of lithium-ion batteries. J. Power Sources, 2011, 196, 2863-2866.

45. S. Mirhashemihaghighi, B. Leon, C. Perez Vicente, J. L. Tirado, R. Stoyanova, M. Yoncheva, E. Zhecheva, R. Saez Puche, E. M. Arroyo, J. Romero de Paz, ithium storage mechanisms and effect of partial cobalt substitution in manganese carbonate electrodes. Inorg. Chem., 2012, 51, 5554-5561.

46. I. A. Courtney, J. R. Dahn, Electrochemical and in situ X-ray diffraction studies of the reaction of lithium with tin oxide composites. J. Electrochem. Soc., 1997, 144, 2045-2052.

# CHAPTER 5. HIERARCHICAL SANDWICH-LIKE STRUCTURE of ULTRAFINE N-RICH POROUS CARBON NANOSPHERES GROWN ON GRAPHENE SHEETS AS SUPERIOR LITHIUM-ION BATTERY ANODES*

## 5.1 Introduction

Lithium-ion batteries (LIBs) have been widely used as power sources in portable electronics.[1-3] Nevertheless, the ever-increasing demands for emerging applications in portable electronics and electric vehicles (EVs) are driving the development of LIBs with higher energy density and power density as well as longer cycling life. As one of the commercially available anode materials, graphite is the most common one but still exhibits some drawbacks such as a low theoretical capacity of 372 mAh $g^{-1}$ and distinctly poorer electrochemical performances at higher charge-discharge rates, which is far from satisfactory for meeting the needs of high-energy high-power LIBs.[3,4] Thus, it is imperative to explore alternative carbonaceous electrode materials with larger capacity, improved cycling stability, better rate performance, and the potential for industrial scale production.

To develop high-performance carbonaceous electrode materials for new-generation LIBs, one strategy is to design and synthesize a novel nanostructure with the following features: (*i*) large surface area with abundant active sites to facilitate Li-ion storage capacity,[5-7] (*ii*) high porosity for enhanced charge transport, thereby resulting in improved rate capability,[8-10] (*iii*) excellent structural stability and electronic conductivity to promote rapid charge transfer with prolonged cycle life,[11,12] and (*iv*) heteroatom N or S doping to manipulate electronic and electrochemical properties and increase number of available active sites for Li-ion storage.[13-15] To achieve these, many new carbonaceous anode materials

* This chapter previously appeared as Zhiqiang Xie, Ziyang He, Xuhui Feng, Wangwang Xu, Xiaodan Cui, Jiuhong Zhang, Cheng Yan, Moises A Carreon, Zheng Liu, and Ying Wang, "Hierarchical sandwich-like structure of ultrafine N-rich porous carbon nanospheres grown on graphene sheets as superior lithium-Ion battery anodes", ACS Appl. Mater. Interfaces, 2016, 8, 10324–10333. It is reprinted by permission of American Chemical Society.

with various nanostructures have been evaluated for lithium storage and demonstrated significantly improved performance compared to commercial graphite anodes, such as heteroatom-doped graphene sheets,[12] micro/nanoporous carbon,[16] hollow carbon spheres,[17] carbon nanofibers,[18] and carbon nanobeads.[19] In spite of these efforts, few have sought to satisfy all the aforementioned features simultaneously since most carbonaceous materials have low electrical conductivity and poor structural stability when cycled at high charge/discharge rates as well as limited active sites for effective Li-ion storage. Therefore, the lithium storage capability and rate performance of carbonaceous anodes still need improvements. By introducing more available active sites for lithium storage, incorporation of nitrogen into carbon has proven to significantly enhance both electronic conductivity and electrochemical reactivity of carbon-based anode materials, resulting in improved performance in LIBs and other energy applications.[13-15,35,36] However, the synthesis of N-rich carbonaceous nanostructures reported previously usually involve tedious processes such as complex chemical reactions, chemical vapor deposition (CVD),[20] thermal annealing with ammonia,[21] and/or various template-based approaches, which are expensive and time-consuming, and thus limit their practical applications for industrial scale production. Because of these trade-offs, design and synthesis of highly porous N-rich carbonaceous anode materials with superior electrical conductivity remain a big challenge.

Metal organic frameworks (MOFs) are a family of crystalline materials with inorganic-organic hybrid structure and have been widely studied for gas separation,[22] sensors,[23] catalysis,[24] owing to their large pore volumes and extremely high specific surface areas. Recently, MOFs have attracted much interest for the applications in LIBs and have proved to be promising precursors for constructing various nanostructured electrodes.[25-28] For instance, Yue *et al*. reported cubic mesoporous Co-ZnO@C via

pyrolysis of Co-doped MOF-5, showing a reversible capacity of 725 mAh $g^{-1}$ after 50 cycles at a specific current of 100 mA $g^{-1}$.[26] Han *et al*. used direct carbonization at 800$^{o}$C under inert atmosphere to fabricate ZIF-8@chitosan composites, which exhibit a specific capacity of 750 mAh $g^{-1}$ after 50 cycles at a specific current of 50 mA $g^{-1}$.[27] Hou *et al*. reported a Co3O4/N-doped carbon hybrid with dodecahedrons structure that delivers 892 mAh $g^{-1}$ after 100 cycles at a specific current of 100 mA $g^{-1}$.[28] Nevertheless, due to the unavoidable breakdown inside the crystalline MOFs and relatively large crystal size ranging from 250 to 500 nm, these MOFs-derived N-doped carbon matrices still exhibit poor structural stability and low electronic conductivity, and thus result in significant capacity fading over prolonged cycling in LIBs.

Herein, to achieve carbonaceous anode material with all the merits of hierarchically porous structure, superior excellent conductivity and high-level nitrogen doping, we present a *in situ* synthesis approach to obtain sandwich-like, graphene-based porous nitrogen-doped carbons (PNCs@Gr) via facile pyrolysis of zeolitic imidazolate framework (ZIF-8) nanocrystals grown on graphene oxide (GO) (ZIF-8@GO), for application as a high-performance anode material in LIBs. We selectedZIF-8 as a suitable carbon precursor to yield *in situ* N-doped porous carbon due to its high N content of ~34 wt%, large porosity and high specific surface area, and meanwhile GO serves as a structure-directing agent and potential platform for nucleation, growth and stabilization of ZIF-8 nanocrystals. Due to insufficient surface functional groups of GO, the amide carbonyl groups of poly(vinylpyrrolidone) (PVP) can be utilized to enrich the functional groups of GO, which might be beneficial for the uniform growth of ZIF-8 nanocrystals on the GO sheet. During subsequent carbonization process, ZIF-8 nanoparticles are transformed to N-rich porous carbon nanospheres, meanwhile GO is thermally reduced to highly conductive graphene. Finally, the sandwich-like PNCs@Gr nanostructure with high porosity, superior electrical

conductivity and rich nitrogen content is successfully synthesized and will thus boost electrochemical performance in LIBs, due to synergic effects of the highly desirable properties. As a result, the sandwich-like PNCs@Gr electrode demonstrates remarkable capacities, outstanding rate performances, as well as cycling stability that are better than most carbonaceous anode materials reported previously.

## 5.2 Experimental Section

### 5.2.1 Preparation of ZIF-8

ZIF-8 crystals were synthesized by mixing 0.81 g of 2-methyimidazole with 25 ml of methanol. To this solution, 0.7 g of $Zn(NO_3)_2 \cdot 6H_2O$ and 25 ml of methanol were added. . Afterwards, the mixed solution was stirred for 5 h. Finally, the solid was collected by centrifuging the mixture at 3000 rpm for 10 min followed by washing with methanol for three times. The collected solid was dried at 75$^{o}$C overnight before using.

### 5.2.2 Synthesis of ZIF-8@GO

Synthesis of ZIF-8@GO was carried out based on a modified approach from literature.[31] Typically, one gram of the as-prepared graphene oxide solution (8 mg $mL^{-1}$) was dispersed in methanol solution containing 50 mg of PVP, by sonication and stirring. Then 5 ml of $Zn(NO_3)_2 \cdot 6H_2O$ of methanol solution and 5 ml of 2-methyimidazole were separately added into GO/PVP solution (40 ml) and the mixed solution was kept for 5 h at room temperature. Afterwards, the product was collected by centrifuging at 3000 rpm for 10 min followed by washing with methanol for three times. After freeze drying, the final product (ZIF-8@GO) was obtained.

### 5.2.3 Synthesis of PNCs@Gr

The as-synthesized ZIF-8@GO was heated at 700$^{o}$C for 5 h under $N_2$ using a ramp rate of 2$^{o}$C/min. For comparison purpose, bare PNCs was prepared by facile pyrolysis of the as-synthesized ZIF-8 sample under the same condition.

5.2.4 Material characterizations

Powder X-ray diffraction (XRD) was carried out using a Rigaku MiniFlex X-ray diffractometer with Cu Kα radiation. XRD Data was collected in the range of 5˚≤2Θ≤90˚ at a scan rate of $2^{o}$/min. Scanning electron microscopy (SEM) and energy-dispersive X-ray spectroscopy (EDS) were performed using a FEI Quanta 3D FEG FIB/SEM dual beam system. The nanostructures of the samples were investigated by transmission electron microscopy (TEM) and high-resolution TEM (HRTEM) using a JEM-2010 instrument microscope operating at 200 kV. X-ray photoelectron spectroscope (XPS) was performed using an AXIS 165 spectrometer and a twin-anode AlKa X-ray source. Thermogravimetric (TG) analysis was carried out using an SII STA7300 analyzer at a ramp rate of 1 °C/min under $N_2$ atmosphere. Brunauer-Emmett-Teller (BET) measurements were conducted using Quantachrome Instruments Autosorb-iQ with extra-high pure gases. Raman spectroscopy was carried out by confocal Raman system in air ambient environment (WITEC alpha300 R) with 532nm diodes laser.

5.2.5 Electrochemical Measurements

The working electrodes in this work were studied by integrating into 2032-type coin cells for various electrochemical measurements at room temperature. Within the coin cells, the lithium foil works as the counter electrode and all the coin cells were assembled in a glove box filled with argon. In a typical fabrication procedure of electrodes, 80 wt% PNCs or PNCs@Gr powders, 10 wt% conductive carbon (acetylene black, Alfa Aesar, 99.5%), and 10 wt% polyvinylidene fluoride (PVDF, Alfa Aesar) binder were first dissolved into 1-methyl-3-pyrrolidone (NMP) to form a homogeneous slurry, which was then uniformly coated on copper foils. Afterwards, the coated copper foils were dried in vacuum at 120˚C for a day. The commercial electrolyte for LIBs was used to construct the battery cells. Typically, 1 M $LiPF_6$ was dissolved in ethylene carbonate (EG)/ dimethyl carbonate (DMC)/diethyl

carbonate (DEC) (1:1:1, v/v/v). Electrochemical performances of the as-prepared electrodes were evaluated at various current rates by using an 8-channel battery analyzer (MTI Corporation). Cyclic voltammetric (CV) measurements were carried out using a CHI605C electrochemical analyzer at a scanning rate of 0.1 mV/s.

### 5.3 Results and discussion

A scheme showing the facile and scalable route for synthesizing PNCs@Gr in this work is presented in Figure 5.1. First, GO is modified with PVP in the solution, since many previous studies have reported that PVP working as surfactant can be absorbed onto the surface of graphene oxide sheets and then help to achieve good dispersion of graphene oxides by lowering their surface energy. In addition, amide carbonyl groups of PVP and oxygen functional groups of GO may coordinate with Zn ions and promote the uniform growth of ZIF-8 crystals on graphene oxide sheets. Next, the sandwich-like ZIF-8@GO sheet was transformed into the PNCs@Gr by direct pyrolysis in $N_2$ atmosphere at 700$^{o}$C. During this process, organic ligands (2-methylimidazolate) from ZIF-8 nanocrystals are carbonized, meanwhile part of nitrogen species and the carbon-reduced zinc metal vaporize away due to instability of nitrogen species at high temperature and low melting point of zinc.[30,31] Within this unique nanostructure, both porous N-doped carbon nanoparticles and graphene sheets not only serve as highways for fast electron transport, but also facilitate fast mass transport at electrode/electrolyte interfaces. Therefore, it is expected that the sandwich-like, graphene-based PNCs@Gr nanostructure will boost the electrochemical performance in LIBs.

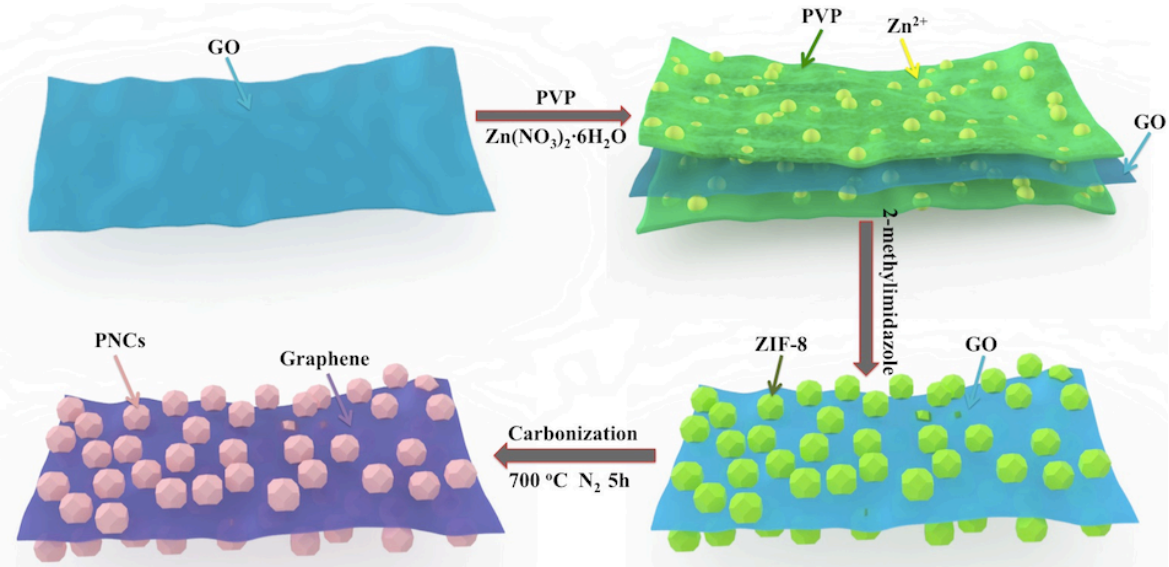


Figure 5.1 Scheme showing the synthetic route for preparing the sandwich-like PNCs@Gr nanostructure.

Figure 5.2a and b show powder X-ray diffraction (XRD) patterns of the as-synthesized samples, namely, ZIF-8, ZIF-8@GO, bare PNCs and sandwich-like PNCs@Gr nanostructure. Before carbonization, the main diffraction peaks can be readily indexed to crystalline ZIF-8 and no noticeable difference is observed between ZIF-8 and ZIF-8@GO from the XRD patterns, since the main peak of ZIF-8 (112) almost overlaps with the main peak (001) of GO at $2\theta$ =12.5°. After carbonization, ZIF-8 and ZIF-8@GO transform to PNCs and PNCs@Gr. The XRD patterns change significantly with the main peak occurring at around 25° corresponding to the (002) reflection of graphite. The broad low-intensity peaks imply that the PNCs and PNCs@Gr have low degree of graphitization, which is consistent with previous reports of other carbonaceous materials.[30-34] It is also found that Zn diffraction peaks are not present in the XRD patterns of both PNCs and PNCs@Gr, indicating that carbon-reduced Zn metal with low melting point (419.5°C) may have been vaporized away during the carbonization process at 700°C. The thermo-gravimetric analysis (TGA) result of pristine ZIF-8 sample. It can be seen that the ZIF-8 sample starts to

decompose at around 550$^{o}$C, indicating a good thermal stability, which is beneficial for being a suitable carbonization precursor, since severe vaporization at high temperature can be avoided, thereby improving the yield of final products. As shown in Fig. S2, the Raman spectra of the ZIF-8@GO and sandwich-like PNCs@Gr structures reveal two characteristic peaks at 1352 and 1590 $cm^{-1}$, which are attributed to the D band and G band of graphitic structure. Notably, the $I_D/I_G$ value of PNCs@Gr ($I_D/I_G$=0.99) is higher than ZIF-8@GO ($I_D/I_G$=0.94), demonstrating the formation of abundant defects and disordered carbon during the carbonization process.[25]

The lithium storage properties of N-doped carbonaceous anode materials highly depend on the doped nitrogen type and doping amount. Therefore, X-ray photoelectron spectroscopy (XPS) measurements of pristine ZIF-8 and bare PNCs are performed. As can be seen in Figure 5.2c-d, after carbonization, the high-resolution spectrum of N 1s is deconvoluted into three different peaks, namely, pyridinic N (398.3 ± 0.2 eV), pyrrolic N (399.8 ± 0.2 eV), and quaternary N (400.8 ± 0.3 eV). This phenomenon indicates successful doping of nitrogen into the resultant porous carbon during the carbonization process of N-containing organic ligands, which is consistent with previous report.[31] According to the literature,[35] electronic conductivity of carbonaceous materials can be significantly increased mproved by nitrogen doping, resulting in improved charge transfer at the interface, which are highly desirable for electrodes in LIBs. Furthermore, it is believed that the presence of nitrogen dopants introduces more defects and thus offers more available active sites to enhance the Li-ion storage properties.[36]

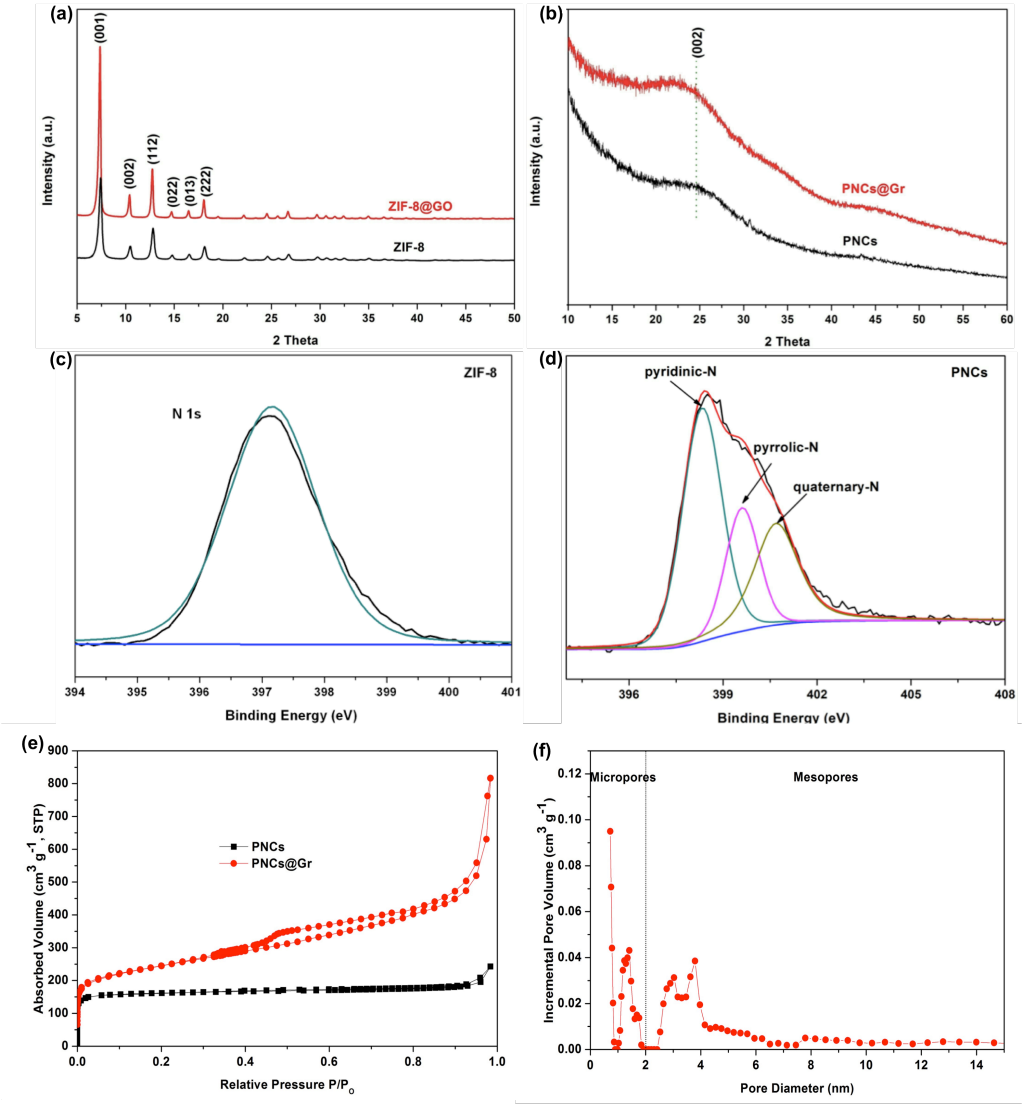


Figure 5.2 XRD patterns of (a) ZIF-8 and ZIF-8@GO before carbonization and (b) bare PNCs and sandwich-like PNCs@Gr nanostructure after carbonization. High-resolution spectrums of the N 1s XPS peaks of (c) ZIF-8 and (d) bare PNCs. (e) Nitrogen adsorption-desorption isotherms of bare PNCs and sandwich-like PNCs@Gr nanostructure. (f) Pore size distribution (PSD) of PNCs@Gr.

To further examine the porous structure of bare PNCs and PNCs@Gr, $N_2$ adsorption-desorption isotherms are performed to determine their specific surface area (SSA) and corresponding pore size distribution (PSD). As shown in Figure 5.2e, bare PNCs display a typical type-I isotherm showing a slight step over the relative pressure from 0.9 to 1.0,

revealing a large portion of micropores, probably due to the inheritance of highly porous ZIF-8. Nevertheless, the sandwich-like PNCs@Gr shows a typical type-IV curve exhibiting a pronounced hysteresis loop. The high $N_2$ adsorption at the relative low pressure reveals the high microporosity, while the hysteresis loop indicates some portion of mesopores exist within the sandwich-like structure. The mesopores may originate from the evaporation of Zn during the carbonization process and likely stacking between sandwich-like PNCs@Gr. Figure 2f shows the pore size distribution (PSD) of sandwich-like PNCs@Gr, revealing both micropores are peaked at 0.77 and 1.40 nm and mesopores are peaked at 3.05 and 3.80 nm based on the Density Functional Theory (DFT) analysis. The appropriate proportion of micropores guarantees its high SSA and mesopores are preferable for electrolyte penetration and Li-ion transport, and thus are extremely favorable for both high energy density and high rate performance in LIBs. Furthermore, thanks to the abundant micro- and mesopores, the specific surface area (SSA) of PNCs@Gr reaches as high as 872 $m^2 g^{-1}$, while that of bare PNCs is only 508 $m^2 g^{-1}$, as revealed by the Brunauer-Emmett-Teller (BET) measurements. Owing to the severe restacking of graphene sheets, the pristine rGO or graphene obtained via thermal annealing of GO proves to possess low SSA of below 100 $m^2 g^{-1}$,[37] which is significantly lower than theoretical SSA value (2630 $m^2 g^{-1}$) of graphene without any overlap of sheets. Therefore, such a significant improvement in the SSA of sandwich-like PNCs@Gr is mainly attributed to synergic effects of components in this hybrid, whereas the likely agglomeration of PNCs and severe restacking of graphene sheets can be effectively addressed by this hierarchical nanostructure design. The larger surface area of PNCs@Gr is anticipated to offer more active sites for lithium ion storage, thus leading to improved specific capacity and enhanced rate capability compared to bare PNCs.

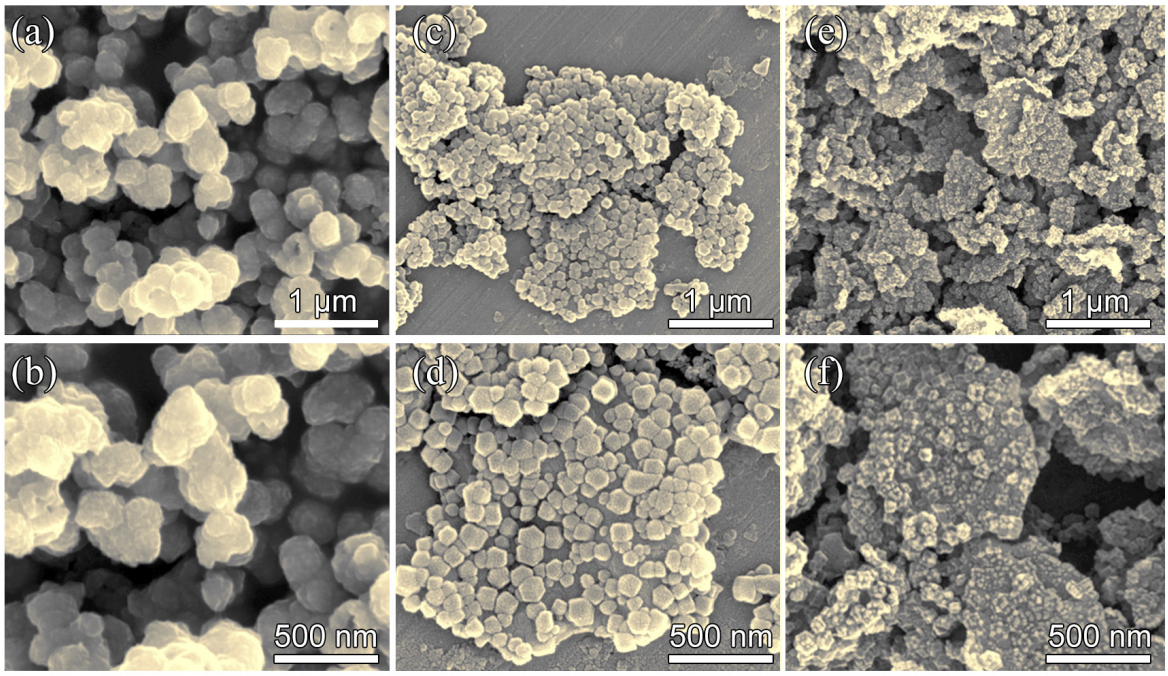


Figure 5.3 SEM images of (a, b) bare PNCs, (c, d) ZIF-8@GO and (e, f) sandwich-like PNCs@Gr nanostructure.

Figure 5.3 displays SEM images of bare PNCs, ZIF-8@GO and sandwich-like PNCs@Gr. As shown in Figure 5.3a and b, bare PNCs consist of numerous nanoparticles (~200 nm in diameter) with rough surfaces and severe agglomeration is also observed. Interestingly, Figure 3c and d reveal that ZIF-8@GO sample preserves the sheet-like morphology of micrometer-sized GO, in which polyhedron-like ZIF-8 nanocrystals are uniformly grown on the GO surface and their average diameter is approximately 150 nm. As shown in Figure 5.3e and f, the PNCs@Gr sample demonstrates that the sheet-like morphology is well preserved after direct carbonization of ZIF-8@GO at 700$^{o}$C. Moreover, it is observed that most PNCs in the composite of PNCs@Gr are composed of ultrafine nanoparticles (~20 nm), likely owing to partial decomposition of ZIF-8 during the carbonization process.

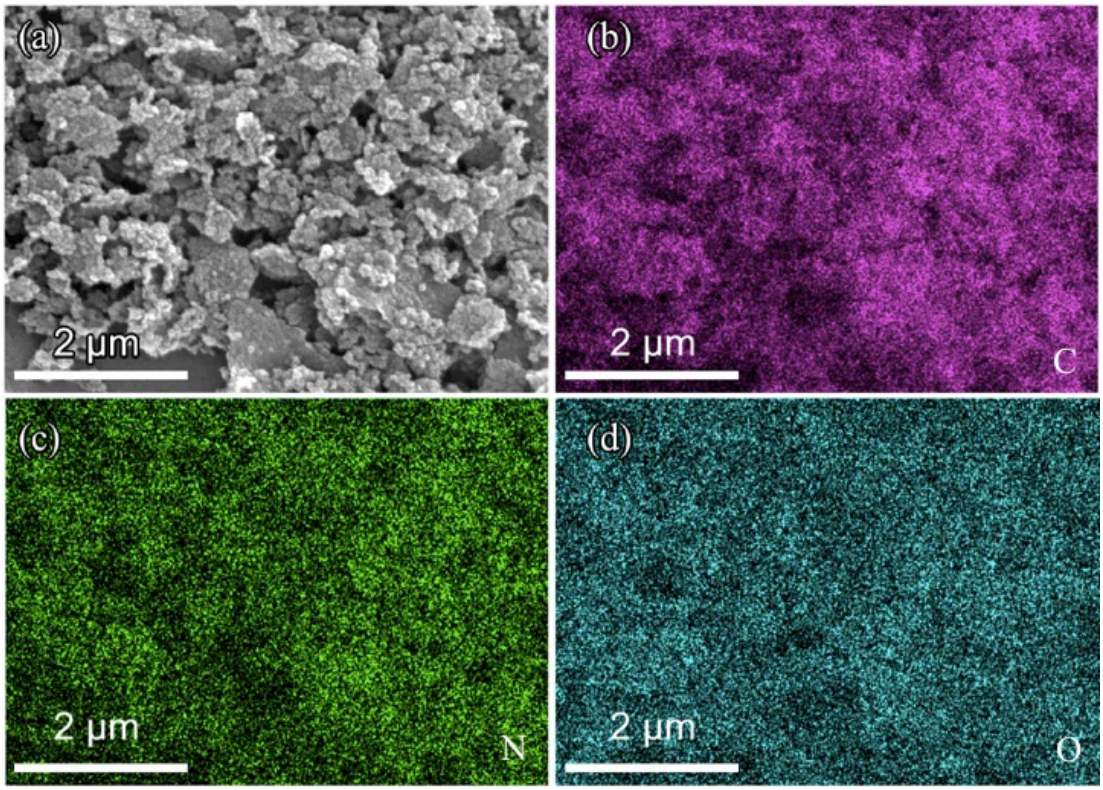


Figure 5.4 (a) SEM image of the sandwich-like PNCs@Gr nanostructure, and (b-d) corresponding elemental mapping results.

The composition of sandwich-like PNCs@Gr nanostructure is further analyzed by energy dispersive spectroscopy (EDS) elemental mapping. As revealed in Figure 5.4a-d, carbon, nitrogen, and oxygen elements are homogeneously distributed, suggesting that the PNCs derived from ZIF-8 are dispersed uniformly on the graphene sheet, and thus form a sandwich-like nanostructure. Furthermore, due to the evaporation of Zn during the carbonization process, we barely observe Zn element distribution from elemental mapping results. In addition, the PNCs@Gr sample contains 21.5 wt% nitrogen, which is significantly higher than most of previously reported N-doped carbonaceous materials in LIBs.[5,16,40,44]

TEM characterization was also performed for better visualization of ZIF-8@GO and PNCs@Gr, as displayed in Figure 5.5. As can be seen in Figure 5.5a and b (TEM images of ZIF-8@GO at different magnifications) that ZIF-8 nanoparticles are homogeneously grown on GO sheets, which is in good agreement with the SEM observations. In addition, the HR-

TEM image of ZIF-8@GO in Figure 5.5c reveals a very small area of exposed GO at the edges, confirms the existence of GO in the sample and the sandwich-like structure of ZIF-8@GO. After carbonization, Figure 5.5d-e reveal that PNCs@Gr displays apparently porous feature and preserve the sandwich-like morphology of ZIF-8@GO. The inset of Figure 5d shows the corresponding selected area electron diffraction (SAED), indicating the amorphous nature of PNCs@Gr, which is supported by the XRD result above. Finally, the HRTEM image in Figure 5.5f confirms the existence of graphene in the composite.

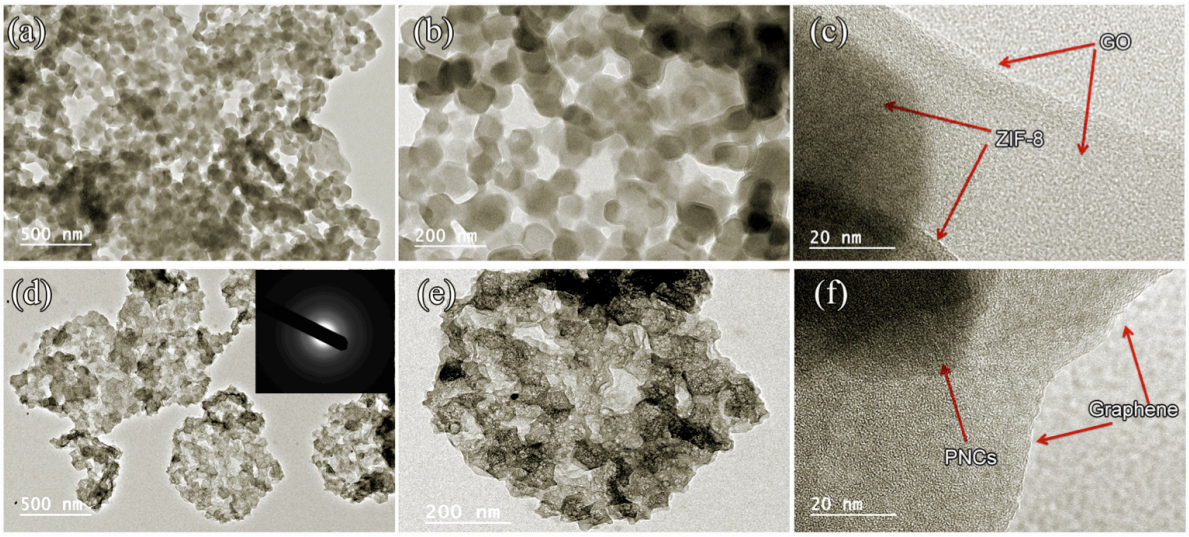


Figure 5.5 (a, b) TEM images of ZIF-8@GO at different magnifications, and (c) HRTEM image of ZIF-8@GO. (d, e) TEM images of the sandwich-like PNCs@Gr nanostructure at different magnifications, and (f) HRTEM image of PNCs@Gr.

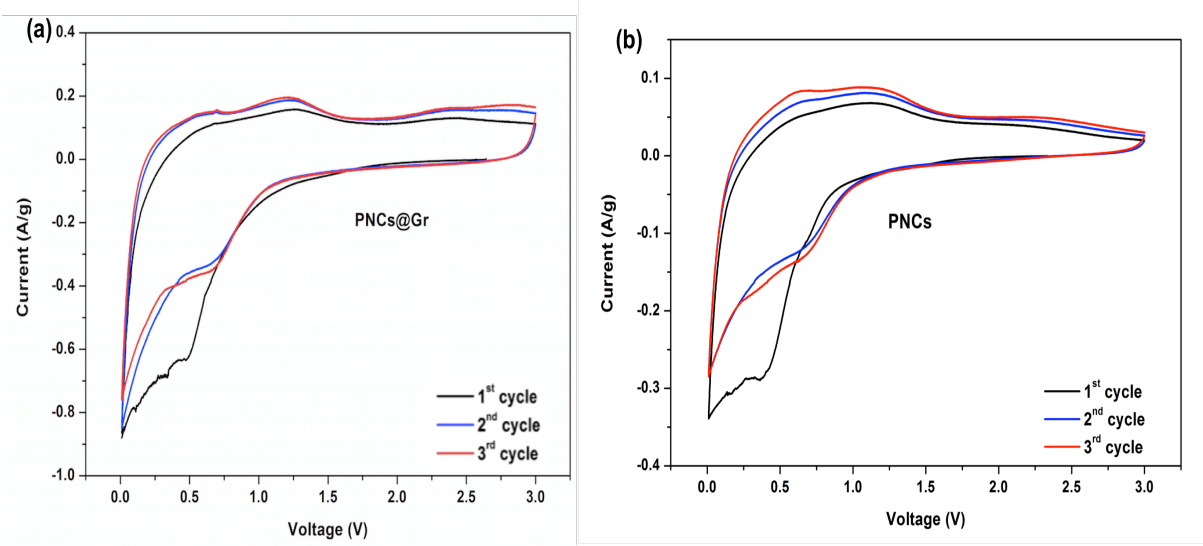


Figure 5.6 Cyclic voltammetry curves of (a) sandwich-like PNCs@Gr and (b) bare PNCs at a scan rate of 0.1 $mVs^{-1}$.

To evaluate lithium storage properties of the as-prepared bare PNCs and sandwich-like PNCs@Gr samples, various electrochemical measurements are performed. Cyclic voltammetry (CV) curves of bare PNCs and sandwich-like PNCs@Gr electrode are recorded between 0.01 and 3.0 V vs. $Li/Li^+$, as shown in Figure 5.6. Both bare PNCs and PNCs@Gr display typical CV characteristics of carbon-based anodes. However, it should be noted that the redox peaks from the PNCs@Gr electrode show obviously higher specific current than that of bare PNCs, likely resulted from the enhanced electrical conductivity and electrochemical reactivity of the electrode.

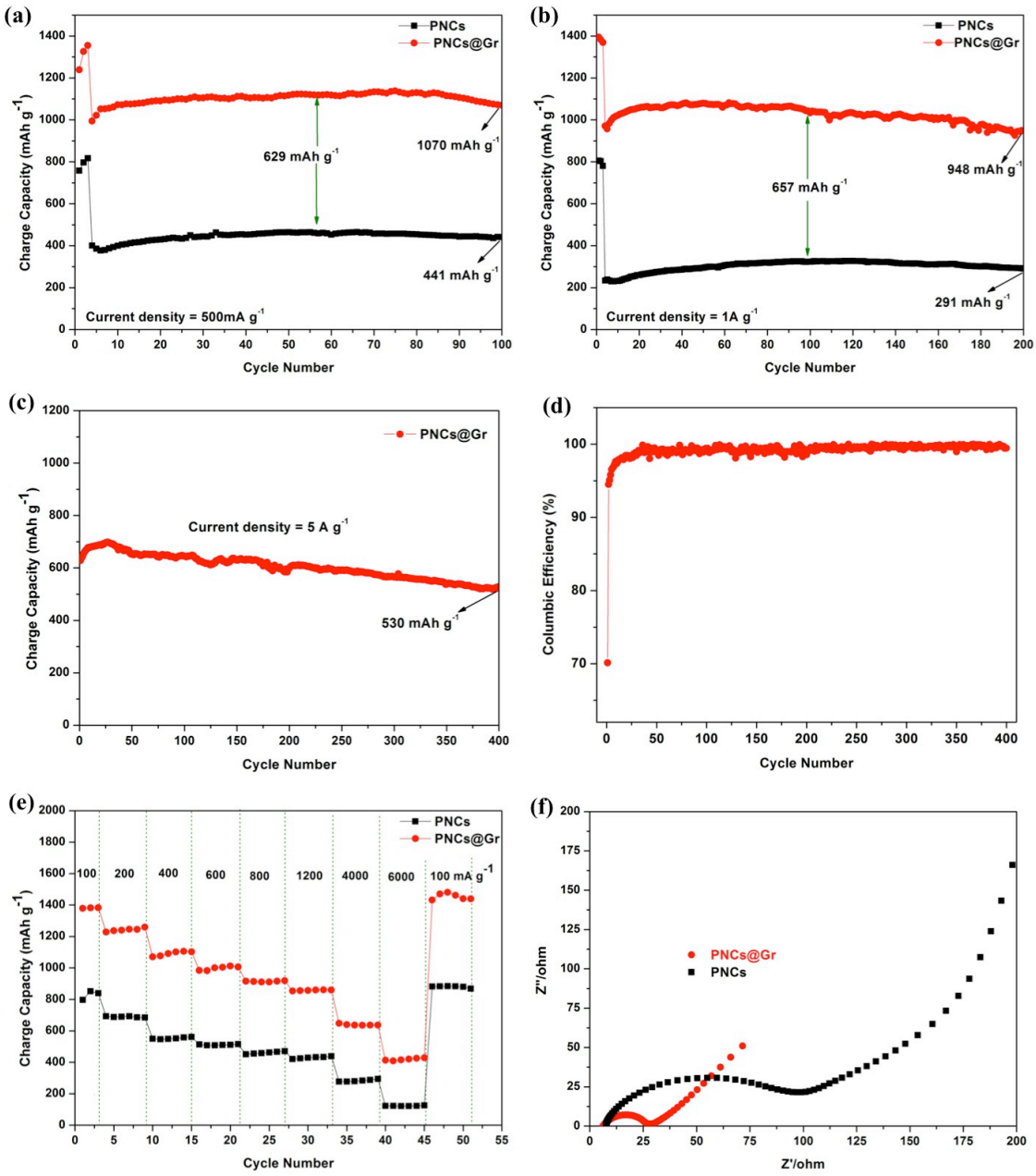


Figure 5.7 Electrochemical characterizations of bare PNCs and sandwich-like PNCs@Gr electrodes. (a, b) Cycling test of bare PNCs and sandwich-like PNCs@Gr electrodes at 500 mA $g^{-1}$ and 1A g-1, respectively. (c) Cycling performance of the sandwich-like PNCs@Gr electrode at 5 A $g^{-1}$ for 400 cycles and (d) corresponding Columbic efficiency. (e) Rate capability of bare PNCs and sandwich-like PNCs@Gr electrodes cycled at various specific currents ranging from100 mA g-1 to 6 A g-1. (f) Nyquist plots of bare PNCs and sandwich-like PNCs@Gr electrodes.

The cycling performances of both PNCs and PNCs@Gr are also evaluated at specific currents of 500 mA $g^{-1}$ and 1 A $g^{-1}$, respectively. To activate the electrodes, a specific current of 100 mA $g^{-1}$ is initially used for the first three cycles during the cycling performance. As revealed in Figure 5.7a-b, the PNCs@Gr anode shows an outstanding cycling performance and a high reversible capacity. At a specific current of 500 mA $g^{-1}$, the PNCs@Gr maintains a much higher reversible capacity of 1070 mAh $g^{-1}$ than that of bare PNCs (441 mAh $g^{-1}$) after 100 cycles, showing a significant improvement of capacity by 629 mAh $g^{-1}$. Even at a higher specific current of 1 A $g^{-1}$, the PNCs@Gr can remain a high reversible capacity of 948 mAh $g^{-1}$ after 200 cycles, which is approximately 97.7% of the $4^{th}$ cycle, while the capacity of bare PNCs is only 291 mAh $g^{-1}$. More importantly, when the specific current reaches 5 A $g^{-1}$, the sandwich-like PNCs@Gr nanostructure retains a specific capacity of 530 mAh $g^{-1}$ after 400 cycles, demonstrating a capacity retention of as high as 84.4%, as shown in Figure 5.7c. In addition, as shown in Figure 5.7d, upon prolonged cycling, the Columbic efficiency of PNCs@Gr is increased to above 99% after initial several cycles, demonstrating its excellent electrochemical reversibility. It is noted that electrochemical performances of PNCs@Gr exceed most previously reported carbon-based materials[16,18,38-45] and recently reported MOF-derived anode materials for LIBs. [16,18,27-29,39-52] Such remarkable improvements of specific capacity and long-term cycling stability are attributed to the following factors. First, in the sandwich-like PNCs@Gr nanostructure, highly desirable combination of micro- and mesopores and ultrafine carbon nanospheres (~20 nm) embedded on the graphene surface offer larger surface area (872 $m^2$ $g^{-1}$) in comparison with bare PNCs (508 $m^2$ $g^{-1}$), and thus not only result in large electrode/electrolyte interface to effectively store lithium ions, but also facilitate fast charge transfer. Second, the highly conductive, mechanically strong and flexible graphene not only improve electronic conductivity of the whole electrode, but also help reduce agglomeration and collapse of structure upon long-term cycling, resulting in

excellent structural stability and superior cycling performance. Finally, the high-level nitrogen doping is believed to further enhance both electronic properties and electrochemical reactivity of PNCs@Gr electrode via introducing defects and more available active sites for lithium storage.

Notably, the PNCs@Gr anode also shows superior rate capability at various specific currents from 100 to 6000 mA $g^{-1}$. As displayed in Figure 5.7e, the reversible capacities of PNCs@Gr are 1378, 1228, 1070, 984, 915, 854 and 647 mAh $g^{-1}$ at 100, 200, 400, 600, 800, 1200 and 4000 mA $g^{-1}$, respectively. Even at 6000 mA $g^{-1}$, the reversible capacity of PNCs@Gr remains 412 mAh $g^{-1}$. More importantly, when the specific current returns back to 100 mA $g^{-1}$, the specific capacity can be recovered to 1432 mAh $g^{-1}$, demonstrating its outstanding reaction reversibility and cycling stability. However, bare PNCs anode shows much lower reversible capacities of 797, 692, 550, 508, 451, 421, 277 and 123 mAh $g^{-1}$ when cycled at 100, 200, 400, 600, 800, 1200, 4000 and 6000 mA $g^{-1}$, respectively. The superior rate capability of the sandwich-like PNCs@Gr electrode is ascribed to its hieratical nanostructure, in which graphene significantly improves electrical conductivity of the electrode, and ultrafine carbon nanospheres offer shorter transport length of lithium ions and better stability when cycled at higher charge/discharge rates, thereby resulting in considerable improvement in rate capability compared to bare PNCs. Therefore, it can be concluded that the PNCs@Gr anode exhibits superior rate capability, significantly improved cycling stability and reversible capacity compared to bare PNCs.

To further understand the origin of superior rate capability of sandwich-like PNCs@Gr anode, electrochemical impedance spectra (EIS) is carried out to investigate electrochemical kinetics occurring at the electrode/electrolyte interfaces and Li-ion intercalation/deintercalation within electrode materials in the battery cells. As seen in Figure 5.7f, the Nyquist plots of bare PNCs and PNCs@Gr shows a slanted line in the low-

frequency region and a depressed semicircle in the medium-frequency region. It is observed that the electrode of sandwich-like PNCs@Gr nanostructure shows a charge transfer resistance of 30 Ω, which is much lower than that of bare PNCs (100 Ω), indicating a significantly enhanced charge transfer within the whole electrode.

Figure 5.8a shows the initial three cycles of the PNCs@Gr electrode at 100 mA $g^{-1}$ from the rate performance testing. Typical charge/discharge profiles are consistent with N-doped carbonaceous anodes for LIBs.[5,16] It is observed that a large irreversible capacity loss occurs in the initial cycle, attributed to the unavoidable decomposition of the electrolyte and formation of the solid-electrolyte interphase (SEI) film.[25] Such observation is consistent with the CV results in Fig. 6, in which the cathodic peaks disappear in the 2nd and 3rd cycles. The charge/discharge curves of the PNCs@Gr electrode cycled at various rates are also displayed in Figure 5.8b.

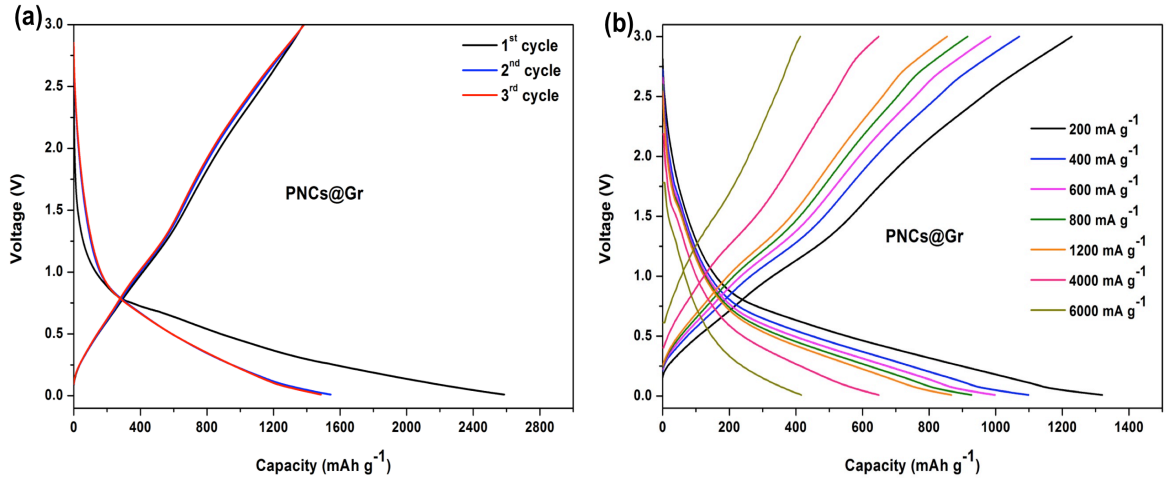


Figure 5.8 Charge-discharge profiles of the sandwich-like PNCs@Gr electrode (a) cycled at 100 $mAg^{-1}$ (the initial three cycles from rate capability testing) and (b) cycled at various rates.

The super high capacity, significantly enhanced rate capability, and excellent cycling performance of sandwich-like PNCs@Gr nanostructure are ascribed to their novel nanostructure and desirable nitrogen doping. In its synthesis, *in situ* growth of ultrafine carbon nanoparticles with highly porous structure effectively reduce the agglomeration

phenomenon compared to bare PNCs, and thus leads to sufficient electrode/electrolyte interface and shorter transport length of Li ions, thereby promoting rapid charge transfer. Furthermore, highly conductive and mechanically strong graphene provides continuous electron-transport pathways and stabilizes the structure upon long-term cycling. In addition, it is believed that the high-level N-doping in PNCs@Gr composite can further enhance its electronic conductivity and electrochemical reactivity, which is beneficial for its electrochemical performances in LIBs.

## 5.4 Conclusions

In conclusion, a sandwich-like, graphene-based porous nitrogen-doped carbons (PNCs@Gr) has been fabricated through direct pyrolysis of zeolitic imidazolate framework (ZIF-8) nanoparticles *in situ* grown on graphene oxide (GO) (ZIF-8@GO), for application as a promising anode material in LIBs. When tested in battery cells, the sandwich-like nanostructure exhibits high reversible capacity, better cycling stability and excellent rate capability in comparison with bare PNCs. The outstanding electrochemical performances of PNCs@Gr anode can be attributed to its novel sandwich-like nanostructure and proper N-doping in the composite. Thus PNCs@Gr demonstrates to be a promising alternative to commercial graphite anode with great potential in high-performance LIBs. In addition, the obtained sandwich-like PNCs@Gr may also be applicable for supercapacitors and other fields.

## 5.5 References

1. S. Chu, A. Majumdar, Opportunities and challenges for a sustainable energy future. Nature, 2012, 488, 294−303.

2. Z. Q. Xie, J. Q. Zhao, Y. Wang, One-step solvothermal synthesis of Sn nanoparticles dispersed in ternary manganese-nickel-cobalt carbonate as superior anode materials for lithium ion batteries. Electrochim. Acta, 2015, 174, 1023-1029.

3. W. W. Xu, Z. Q. Xie, X. D. Cui, K. N. Zhao, L. Zhang, L. Q. Mai, Y. Wang, Direct growth of an economic green energy storage material: a monocrystalline jarosite-$KFe_3(SO_4)_2(OH)_6$-nanoplates@rGO hybrid as a superior lithium-ion battery cathode. J. Mater. Chem. A. 2016, 4, 3735-3742.

4. N. A. Kaskhedikar, J. Maier, Lithium storage in carbon nanostructures. Adv. Mater. 2009, 21, 2664-2680.

5. L. Qie, W. M. Chen, Z. H. Wang, Q. G. Shao, X. Li, L. X. Yuan, X. L. Hu, W. X. Zhang, Y. H. Huang, Nitrogen-doped porous carbon nanofiber webs as anodes for lithium ion batteries with a superhigh capacity and rate capability. Adv. Mater. 2012, 24, 2047-2050.

6. Y. Chen, X. Li, K. Park, J. Song, J. Hong, L. Zhou, Y. W. Mai, H. Huang, J. B. Goodenough, Hollow carbon-nanotube/carbon-nanofiber hybrid anodes for Li-ion batteries. J. Am. Chem. Soc. 2013, 135, 16280-16283.

7. L. Qie, W. Chen, H. Xu, X. Xiong, Y. Jiang, F. Zou, X. Hu, Y. Xin, Z. Zhang, Y. Huang, Synthesis of functionalized 3D hierarchical porous carbon for high-performance supercapacitors. Energy Environ. Sci. 2013, 6, 2497-2504.

8. Y. Li, Z. Li, P. K. Shen, Simultaneous formation of ultrahigh surface area and three-dimensional hierarchical porous graphene-like networks for fast and highly stable supercapacitors. Adv. Mater. 2013, 17, 2474-2480.

9. Y. Liang, D. Wu, R. Fu, Carbon microfibers with hierarchical porous structure from electrospun fiber-like natural biopolymer. Sci. Rep. 2013, 3, 1119.

10. C. Hu, L. Wang, Y. Zhao, M. Ye, Q. Chen, Z. Feng, L. Qu, Designing nitrogen-enriched echinus-like carbon capsules for highly efficient oxygen reduction reaction and lithium Ion storage. Nanoscale. 2014, 6, 8002-8009.

11. Z. Li, Z. Xu, X. Tan, H. Wang, C. M. B. Holt, T. Stephenson, B. C. Olsen, D. Mitlin, Mesoporous nitrogen-rich carbons derived from protein for ultra-high capacity battery anodes and supercapacitors. Energy Environ. Sci. 2013, 6, 871-878.

12. Z. S. Wu, W. C. Ren, L. Xu, F. Li, H. M. Cheng, Doped graphene sheets as anode materials with superhigh rate and large capacity for lithium ion batteries. ACS Nano. 2011, 5, 5463-5471.

13. W. H. Shin, H. M. Jeong, B. G. Kim, J. K. Kang, J. W. Choi, Nitrogen-doped multiwall carbon nanotubes for lithium storage with extremely high capacity. Nano Lett. 2012, 12, 2283-2288.

14. Y. G. Li, W. Zhou, H. L. Wang, L. M. Xie, Y. Y. Liang, F. Wei, J. C. Idrobo, S. J. Pennycook, H. J. Dai, An oxygen reduction electrocatalyst based on carbon nanotube–graphene complexes. Nat. Nanotechnol. 2012, 7, 394-400.

15. L. J. Yang, S. J. Jiang, Y. Zhao, L. Zhu, S. Chen, X. Z. Wang, Q. Wu, J. Ma, Y. W. Ma, Z. Hu, Boron-doped carbon nanotubes as metal-free electrocatalysts for the oxygen reduction reaction. Angew. Chem., Int. Ed. 2011, 50, 7132-7135.

16. K. T. Lee, J. C. Lytle, N. S. Ergang, S. M. Oh, A. Stein, Synthesis and rate performance of monolithic macroporous carbon electrodes for lithium-ion secondary batteries. Adv. Funct. Mater. 2005, 15, 547-556.

17. F. D. Han, Y. J. Bai, R. Liu, B. Yao, Y. X. Qi, N. J. Lun, X. Zhang, Template-free synthesis of interconnected hollow carbon nanospheres for high-performance anode material in lithium-ion batteries. Adv. Energy Mater. 2011, 1, 798-801.

18. Li, C.; Yin, X.; Chen, L.; Li, Q.; Wang, T. Porous Carbon Nanofibers Derived from Conducting Polymer: Synthesis and Application in Lithium-Ion Batteries with High-Rate Capability. J. Phys. Chem. C. 2009, 113, 13438-13442.

19. H. Wang, T. Abe, S. Maruyama, Y. Iriyama, Z. Ogumi, K. Yoshikawa, Graphitized carbon nanobeads with an onion texture as a lithium-ion battery negative electrode for high-rate use. Adv. Mater. 2005, 17, 2857-2860.

20. D. Wei, Y. Liu, Y. Wang, H. Zhang, L. Huang, G. Yu, Synthesis of N-doped graphene by chemical vapor deposition and its electrical properties. Nano Lett. 2009, 9, 1752-1758.
21. X. R. Wang, X. L. Li, L. Zhang, Y. Yoon, P. K. Weber, H. L. Wang, J. Guo, H. J. Dai, N-doping of graphene through electrothermal reactions with ammonia. Science 2009, 324, 768-771.

22. T. H. Bae, J. S. Lee, W. Qiu, W. J. Koros, C. W. Jones, S. Nair, A high-performance gas-separation membrane containing submicrometer-sized metal–organic framework crystals. Angew. Chem. Int. Ed. 2010, 49, 9863-9866.

23. B. V. Harbuzaru, A. Corma, F. Rey, J. L. Jordá, D. Ananias, L. D. Carlos, J. Rocha, A miniaturized linear pH sensor based on a highly photoluminescent self-assembled europium(III) metal–organic framework. Angew. Chem. Int. Ed. 2009, 48, 6476-6479.

24. R. Li, J. Hu, M. Deng, H. Wang, X. Wang, Y. Hu, H. L. Jiang, J. Jiang, Q. Zhang, Y. Xie, Y. Xiong, Integration of an inorganic semiconductor with a metal–organic framework: a platform for enhanced gaseous photocatalytic reactions. Adv. Mater. 2014, 26, 4783-4788.

25. F. C. Zheng, Y. Yang, Q. W. Chen, High lithium anodic performance of highly nitrogen-doped porous carbon prepared from a metal-organic framework", Nat. Commun. 2014,5,5261 doi: 10.1038/ncomms6261.

26. H. Yue, Z. Shi, Q. Wang, Z. Cao, H. Dong, Y. Qiao, Y. Yin, S. Yang, MOF-derived cobalt-doped ZnO@C composites as a high-performance anode material for lithium-ion batteries. ACS Appl. Mater. Interfaces. 2014, 6, 17067-17074.

27. Y. Han, P. Qi, S. Li, X. Feng, J. Zhou, H. Li, S. Su, X. Li, B. Wang, A novel anode material derived from organic-coated ZIF-8 nanocomposites with high performance in lithium ion batteries. Chem. Commun. 2014, 50, 8057-8060.

28. Y. Hou, J. Y. Li, Z. H. Wen, S. M. Cui, C. Yuan, J. H. Chen, $Co_3O_4$ Nanoparticles embedded in nitrogen-doped porous carbon dodecahedrons with enhanced electrochemical properties for lithium storage and water splitting. Nano Energy. 2015, 12, 1-8.

29. X. Li, W. Qi, D. Mei, M. L. Sushko, I. Aksay, J. Liu, Functionalized graphene sheets as molecular templates for controlled nucleation and self-assembly of metal oxide-graphene nanocomposites. Adv. Mater. 2012, 24, 5136-5141.

30. H. L. Jiang, B. Liu, Y. Q. Lan, K. Kuratani, T. Akita, H. Shioyama, F. Q. Zong, Q. Xu, From metal–organic framework to nanoporous carbon: toward a very high surface area and hydrogen uptake. J. Am. Chem. Soc, 2011, 133, 11854-11857.

31. T. Palaniselvam, B. P. Biswal, R. Banerjee, S. Kurungot, Zeolitic imidazolate framework (ZIF)-drived, hollow-core, nitrogen-doped carbon nanostructures for oxygen-reduction reactions in PEFCs. Chem. Eur. J. 2013, 19, 9335-9342.

32. L. L. Zhang, X. S. Zhao, Carbon-based materials as supercapacitor electrodes. Chem. Soc. Rev. 2009, 38, 2520–2531.

33. K. Jost, C. R. Perez, J. K. McDonough, V. Presser, M. Heon, G. Dion, Y. Gogotsi, Carbon coated textiles for flexible energy storage. Energy Environ. Sci. 2011, 4, 5060–5067.

34. Y. W. Zhu, S. Murali, M. D. Stoller, K. J. Ganesh, W. W. Cai, P. J. Ferreira, A. Pirkle, R. M. Wallace, K. A. Cychosz, M. Thommes, Dong. Su, E. A. Stach, R. S. Ruoff, Carbon-based supercapacitors produced by activation of graphene. Science 2011, 332, 1537–1541.

35. L. Zhao, Y. S. Hu, H. Li, Z. Wang, L. Chen, Porous $Li_4Ti_5O_{12}$ coated with N-doped carbon from ionic liquids for Li-ion batteries. Adv. Mater. 2011, 23, 1385-1388.

36. J. H. Hou, C. B. Cao, F. Idrees, X. L. Ma, Hierarchical porous nitrogen-doped carbon nanosheets derived from silk for ultrahigh-capacity battery anodes and supercapacitors. ACS Nano. 2015, 9, 2556-2564.

37. Y. Hou, Z. H. Wen, S. M. Cui, S. Q. Ci, S. Mao, J. H. Chen, An advanced nitrogen-doped graphene/cobalt-embedded porous carbon polyhedron hybrid for efficient catalysis of oxygen reduction and water splitting. Adv. Funct. Mater. 2015, 25, 872-882.

38. M. Chen, C. Yu, S. H. Liu, X. M. Fan, C. T. Zhao, X. Zhang, J. S. Qiu, Micro-sized porous carbon spheres with ultra-high rate capability for lithium storage. Nanoscale 2015, 7, 1791-1795.

39. J. Ou, Y. Z. Zhang, L. Chen, Q. Zhao, Y. Meng, Y. Guo, D. Xiao, Nitrogen-rich porous carbon derived from biomass as a high performance anode material for lithium ion batteries. J. Mater. Chem. A. 2015, 3, 6534-6541.

40. D. C. Guo, F. Han, A. H. Lu, Porous carbon anodes for a high capacity lithium-ion battery obtained by incorporating silica into benzoxazine during polymerization. Chem. Eur. J. 2015, 21, 1520-1525.

41. F. F. Wang, R. R. Song, H. H. Song, X. H. Chen, J. S. Zhou, Z. K. Ma, M. C. Li, Q. Lei, Simple synthesis of novel hierarchical porous carbon microspheres and their application to rechargeable lithium-ion batteries. Carbon. 2015, 81, 314-321.

42. Y. M. Chen, X. Y. Li, K. S. Park, J. Song, J. H. Hong, L. M. Zhou, Y. W. Mai, H. T.

Huang, J. B. Goodenough, Hollow carbon-nanotube/carbon-nanofiber hybrid anodes for Li-ion batteries. J. Am. Chem. Soc. 2013, 135, 16280-16283.

43. D. D. Cai, S. Q. Wang, P. C. Lian, X. F. Zhu, D. D. Li, W. S. Yang, H. H. Wang, Super high capacity and rate capability of high-level nitrogen-doped graphene sheets as anode materials for lithium-ion batteries. Electrochim. Acta. 2013, 90, 492-497.

44. X. F. Li, J. Liu, Y. Zhang, Y. L. Li, H. Liu, X. B. Meng, J. L. Yang, D. S. Geng, D. N. Wang, R. Y. Li, X. L. Sun, High concentration nitrogen doped carbon nanotube anodes with superior $Li^+$ storage performance for lithium rechargeable battery application. J. Power Sources. 2012, 197, 238-245.

45. Z. Li, Z. W. Xu, X. H. Tan, H. L. Wang, C. M. B. Holt, T. Stephenson, B. C. Olsen, D. Mitlin, Mesoporous nitrogen-rich carbons derived from protein for ultra-high capacity battery anodes and supercapacitors. Energy Environ. Sci. 2013, 6, 871-878.

46. G. Huang, F. F. Zhang, X. C. Du, Y. L. Qin, D. M. Yin, L. M. Wang, Metal organic frameworks route to in situ insertion of multiwalled carbon nanotubes in $Co_3O_4$ polyhedra as anode materials for lithium-ion batteries. ACS. Nano. 2015, 9, 1592-1599.

47. G. H. Zhang, S. C. Hou, H. Zhang, W. Zeng, F. L. Yan, C. C. Li, H. G. Duan, High-performance and ultra-stable lithium-ion batteries based on MOF-derived ZnO@ZnO quantum dots/C core-shell nanorod arrays on a carbon cloth anode. Adv. Mater. 2015, 27, 2400-2405.

48. A. Banerjee, U. Singh, V. Aravinda, M. Srinivasan, S. Ogale, Synthesis of CuO nanostructures from Cu-based metal organic framework (MOF-199) for application as anode for Li-ion batteries. Nano Energy. 2013, 2, 1158-1163.

49. S. J. Yang, S. H. Nam, T. H. Kim, J. H. Im, H. S. Jung, J. H. Kang, S. G. Wi, B. W. Park, C. R. Park, Preparation and exceptional lithium anodic performance of porous carbon-coated ZnO quantum dots derived from a metal–organic framework. J. Am, Chem. Soc. 2013, 135, 7394-7397.

50. X. D. Xu, R. G. Cao, S. Y. Jeong, J. Cho, Spindle-like mesoporous α-Fe2O3 anode material prepared from MOF template for high-rate lithium batteries. Nano Lett. 2012, 12, 4988-4991.

51. Z. L. Xiu, M. H. Alfaruqi, J. H. Gim, J. J. Song, S. J. Kim, T. V. Thi, P. T. Duong, J. P. Baboo, V. Mathew, J. K. Kim, Hierarchical porous anatase $TiO_2$ derived from a titanium metal–organic framework as a superior anode material for lithium ion batteries. Chem. Commun. 2015, 51, 12274-12277.

# CHAPTER 6. CONCLUSIONS

In this thesis, two approaches have been developed to significantly enhance the electrochemical performance of cathode materials for advanced lithium-ion batteries: One is transition metal doping of $Li_4Mn_5O_{12}$ cathodes via a facile sol-gel method combined with post-heat treatment to improve its specific capacity and voltage plateau; the other one is to synthesize core-shell (L@Score-shell) cathode material for high-energy and high-power lithium-ion batteries. In addition to cathode materials, two types of high-performance anode materials have been designed and synthesized for lithium-ion batteries. One is a novel structure with Sn nanoparticles well dispersed in the microspheres of manganese-nickel-cobalt carbonate MNCCO3 (Sn@MNCCO3) prepared by using a facile one-step solvothermal process. The other one is sandwich-like, porous nitrogen-doped carbon synthesized by using zeolitic imidazolate framework (ZIF-8) as a template and carbon precursor.

The spinel $Li_4Mn_5O_{12}$ has been considered as a prospective 3V cathode material for the next generation of lithium-ion batteries (LIBs) due to its high energy density and excellent cycling stability. However, the low operating voltage (~3V) makes $Li_4Mn_5O_{12}$ impractical for high-energy high-power LIBs. To address this issue, Ni and Fe dual doped $Li_4Mn_{5-x-y}Ni_xFe_yO_{12}$ has been prepared via a facile sol-gel method combined with post-heat treatment. The effects of dual-cations doping on the crystal structure, morphology and electrochemical properties were investigated by X-ray diffraction (XRD), scanning electron microscopy (SEM), energy-dispersive X-ray spectroscopy (EDS) and galvanostatic charge/discharge analysis. As a result, $Li_4Mn_4Ni_{0.5}Fe_{0.5}O_{12}$ exhibits the highest reversible specific capacity of 133 mAh/g at a specific current density of 25 mA/g after 100 cycles and exhibits a significantly improved high voltage performance with corresponding capacity of ~80 mAh/g at an average voltage of 4.7 V vs. $Li/Li^+$ and ~122 mAh/g at above 4.0 V. These

results indicate the dual doping of Ni and Fe can effectively improve both the operating voltage and reversible specific capacity of $Li_4Mn_5O_{12}$ with excellent cycling stability, demonstrating a promising high-voltage cathode material for high-energy high-power LIBs.

We report, for the first time, simple and novel synthesis of a Li-rich layered-spinel core-shell heterostructure (L@Score-shell) via evaporation-induced self-assembly (EISA) of Ni-doped $Li_4Mn_5O_{12}$ nanoparticles ($Li_4Mn_{4.5}Ni_{0.5}O_{12}$) onto the surface of layered $Li[Li_{0.2}Mn_{0.54}Ni_{0.13}Co_{0.13}]O_2$ (LMNCO) without using any surfactant during the coating process. The resultant L@S core-shell as cathode in lithium ion batteries demonstrates significantly improved specific capacity, cycling performance and rate capability compared to pristine LMNCO.

Sn with high theoretical specific capacity has suffered from poor cycling stability due to its huge volume changes during charging/discharging processes. Thus, a novel structure of tin nanoparticles well dispersed in ternary manganese-nickel-cobalt carbonate $Mn_{0.54}Ni_{0.13}Co_{0.13}(CO_3)_{0.8}$ ($MNCCO_3$) is synthesized using a facile one-step solvothermal process and demonstrates significantly improved electrochemical performance compared to Sn nanoparticles or bare $MNCCO_3$. Additionally, Sn content can be optimized to maximize the battery performance of the composite. When tested as an anode material in lithium ion batteries, the composite with 10 wt.% Sn nanoparticles dispersed in $MNCCO_3$ matrix ($10Sn@MNCCO_3$) demonstrates the best performance, delivering a high initial charge capacity of 929 mAh/g and retains a specific capacity of 657 mAh/g after 50 cycles and 560 mAh/g after 100 cycles at a specific current of 100 mA/g. The charge capacity of $10Sn@MNCCO_3$ decreases from a value of 991 mAh/g when cycled at 50 mA/g to 64 mAh/g at 2000 mA/g with the increasing specific current. When the specific current returns from 2000 mA/g to 50 mA/g, $10Sn@MNCCO_3$ retains a high capacity of 791 mAh/g. The improved electrochemical performance can be ascribed to the synergic effect of both

components in the composite, in which ternary carbonate $MNCCO_3$ matrix not only provides high practical capacity, but also effectively accommodates the strain of dramatic volume change during long cycling, meanwhile Sn ensures a good electrical contact of the overall electrode due to its high electronic conductivity.

A sandwich-like, graphene-based porous nitrogen-doped carbon (PNCs@Gr) has been prepared through facile pyrolysis of zeolitic imidazolate framework nanoparticles in situ grown on graphene oxide (GO) (ZIF-8@GO). Such sandwichlike nanostructure can be used as anode material in lithium ion batteries, exhibiting remarkable capacities, outstanding rate capability, and cycling performances that are some of the best results among carbonaceous electrode materials and exceed most metal oxide-based anode materials derived from metal orgainc frameworks (MOFs). Apart from a high initial capacity of 1378 mAh/g at 100 mA/g, this PNCs@Gr electrode can be cycled at high specifi c currents of 500 and 1000 mA/g with very stable reversible capacities of 1070 and 948 mAh/g to 100 and 200 cycles, respectively. At a higher specifi c current of 5000 mA/g, the electrode still delivers a reversible capacity of over 530 mAh/g after 400 cycles, showing a capacity retention of as high as 84.4%. Such an impressive electrochemical performance is ascribed to the ideal combination of hierarchically porous structure, a highly conductive graphene platform, and high-level nitrogen doping in the sandwich-like PNCs@Gr electrode obtained via in situ synthesis.

In conclusion, this thesis work provides various approaches to achieve significantly improved electrochemical performances of electrode materials for advanced lithium-ion batteries. Transition metal doping is very cost-effective for enhancing the specific capacity and improving the voltage plateau of $Li_4Mn_5O_{12}$ spinel cathode materials. Furthermore, novel design and synthesis of nanostructured electrode materials can achieve higher capacity and better rate capability of both cathode and anode materials.

## APPENDIX: PERMISSION TO USE COPYRIGHTED MATERIALS

1. Permission of Using Published Material from *Journal of The Electrochemical Society*:

**Reproduced by permission of ECS-The Electrochemical Society for the following paper:**
Zhiqiang Xie, Hilary Eikhuemelo, Jianqing Zhao, Carrington Cain, Wangwang Xu and Ying Wang, "Ni and Fe dual doped $Li_4Mn_5O_{12}$ spinels as cathode materials for high-voltage Li-ion batteries", Journal of The Electrochemical Society, 2015, 162, A1523-A1529.
DOI: 10.1149/2.0601508jes
http://jes.ecsdl.org/content/162/8/A1523.short

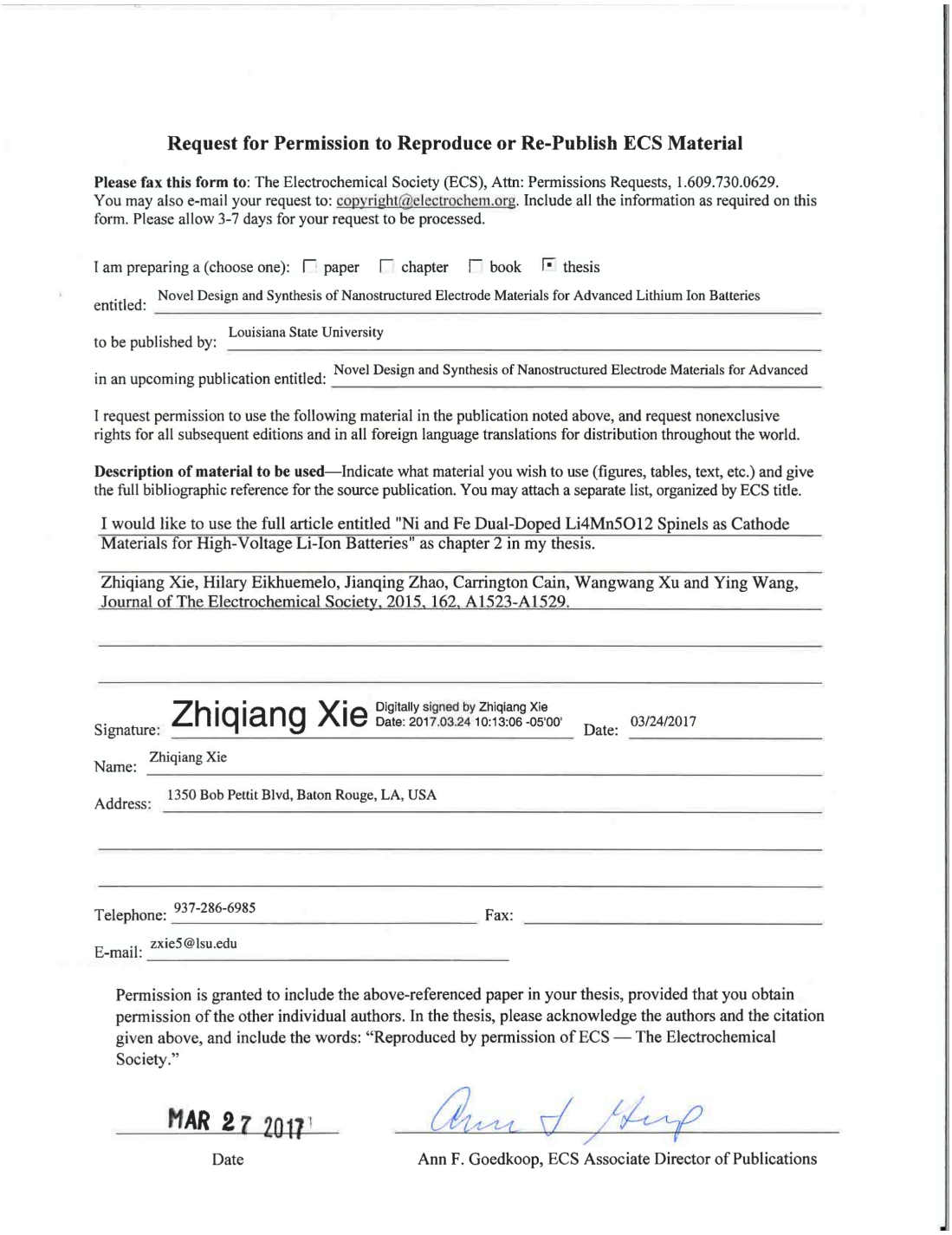

**Request for Permission to Reproduce or Re-Publish ECS Material**

**Please fax this form to**: The Electrochemical Society (ECS), Attn: Permissions Requests, 1.609.730.0629. You may also e-mail your request to: copyright@electrochem.org. Include all the information as required on this form. Please allow 3-7 days for your request to be processed.

I am preparing a (choose one): ☐ paper ☐ chapter ☐ book ☒ thesis

entitled: Novel Design and Synthesis of Nanostructured Electrode Materials for Advanced Lithium Ion Batteries

to be published by: Louisiana State University

in an upcoming publication entitled: Novel Design and Synthesis of Nanostructured Electrode Materials for Advanced

I request permission to use the following material in the publication noted above, and request nonexclusive rights for all subsequent editions and in all foreign language translations for distribution throughout the world.

**Description of material to be used**—Indicate what material you wish to use (figures, tables, text, etc.) and give the full bibliographic reference for the source publication. You may attach a separate list, organized by ECS title.

I would like to use the full article entitled "Ni and Fe Dual-Doped Li4Mn5O12 Spinels as Cathode Materials for High-Voltage Li-Ion Batteries" as chapter 2 in my thesis.

Zhiqiang Xie, Hilary Eikhuemelo, Jianqing Zhao, Carrington Cain, Wangwang Xu and Ying Wang, Journal of The Electrochemical Society, 2015, 162, A1523-A1529.

Signature: Zhiqiang Xie Digitally signed by Zhiqiang Xie Date: 2017.03.24 10:13:06 -05'00' Date: 03/24/2017

Name: Zhiqiang Xie

Address: 1350 Bob Pettit Blvd, Baton Rouge, LA, USA

Telephone: 937-286-6985 Fax:

E-mail: zxie5@lsu.edu

Permission is granted to include the above-referenced paper in your thesis, provided that you obtain permission of the other individual authors. In the thesis, please acknowledge the authors and the citation given above, and include the words: "Reproduced by permission of ECS — The Electrochemical Society."

MAR 27 2017

Date

Ann F. Goedkoop, ECS Associate Director of Publications

2. Permission of Using Published Material from *Chemical Communication*:

**Reproduced by permission of The Royal Society of Chemistry (RSC) for the following paper:**
Zhiqiang Xie, Sarah Ellis, Wangwang Xu, Dara Dye, Jianqing Zhao and Ying Wang, ″A novel preparation of core-shell electrode materials via evaporation-induced self-assembly of nanoparticles for advanced Li-ion batteries", Chemical Communication, 2015, **51**, 15000-15003.
DOI: 10.1039/C5CC05577F
http://pubs.rsc.org/en/Content/ArticleLanding/2015/CC/c5cc05577f#!divAbstract

From: "CONTRACTS-COPYRIGHT (shared)" <Contracts-Copyright@rsc.org>
Subject: RE: About copyright permission
Date: March 28, 2017 at 10:36:24 AM CDT
To: 'Zhiqiang Xie' <zxie5@lsu.edu>

Dear Zhiqiang,

The Royal Society of Chemistry (RSC) hereby grants permission for the use of your paper(s) specified below in the printed and microfilm version of your thesis. You may also make available the PDF version of your paper(s) that the RSC sent to the corresponding author(s) of your paper(s) upon publication of the paper(s) in the following ways: in your thesis via any website that your university may have for the deposition of theses, via your university's Intranet or via your own personal website. We are however unable to grant you permission to include the PDF version of the paper(s) on its own in your institutional repository. The Royal Society of Chemistry is a signatory to the STM Guidelines on Permissions (available on request).

Please note that if the material specified below or any part of it appears with credit or acknowledgement to a third party then you must also secure permission from that third party before reproducing that material.

Please ensure that the thesis states the following:

Reproduced by permission of The Royal Society of Chemistry and include a link to the paper on the Royal Society of Chemistry's website.

Please ensure that your co-authors are aware that you are including the paper in your thesis.

Regards,

Antonella

**From:** Zhiqiang Xie [mailto:zxie5@lsu.edu]
**To:** CONTRACTS-COPYRIGHT (shared) <Contracts-Copyright@rsc.org>

**Subject:** About copyright permission

To Whom it May Concern,

This is Zhiqiang Xie, a graduate student from Mechanical Engineering Department at Louisiana State University, and also the first author of the following paper published in *Chemical Communication.*
Zhiqiang Xie, Sarah Ellis, Wangwang Xu, Dara Dye, Jianqing Zhao and Ying Wang, ″A novel preparation of core-shell electrode materials via evaporation-induced self-assembly of nanoparticles for advanced Li-ion batteries", Chemical Communication, 2015, **51**, 15000-15003.

I would like to include the full article described above into my master thesis as Chapter 3.
I would really appreciate it if I could receive the copyright permission before April 1, 2017.
If you have any question or need any further information, please let me know soon.

Sincerely,

Zhiqiang (Andrew) Xie
Department of Mechanical & Industrial Engineering
Louisiana State University, Baton Rouge, LA 70803
Email: zxie5@lsu.edu, andrewxie1020@gmail.com

3. Permission of Using Published Material from *Electrochimica Acta*:

**ELSEVIER LICENSE**
**TERMS AND CONDITIONS**

Mar 27, 2017

This Agreement between Zhiqiang Xie ("You") and Elsevier ("Elsevier") consists of your license details and the terms and conditions provided by Elsevier and Copyright Clearance Center.

| | |
|---|---|
| License Number | 4077260651457 |
| License date | |
| Licensed Content Publisher | Elsevier |
| Licensed Content Publication | Electrochimica Acta |
| Licensed Content Title | One-step solvothermal synthesis of Sn nanoparticles dispersed in ternary manganese-nickel-cobalt carbonate as superior anode materials for lithium ion batteries |
| Licensed Content Author | Zhiqiang Xie,Jianqing Zhao,Ying Wang |
| Licensed Content Date | 20 August 2015 |
| Licensed Content Volume | 174 |
| Licensed Content Issue | n/a |
| Licensed Content Pages | 7 |
| Start Page | 1023 |
| End Page | 1029 |
| Type of Use | reuse in a thesis/dissertation |
| Intended publisher of new work | other |
| Portion | full article |
| Format | both print and electronic |
| Are you the author of this Elsevier article? | Yes |
| Will you be translating? | No |
| Order reference number | |
| Title of your thesis/dissertation | NOVEL DESIGN AND SYNTHESIS OF NANOSTRUCTURED ELECTRODE MATERIALS FOR ADVANCED LITHIUM ION BATTERIES |
| Expected completion date | May 2017 |
| Estimated size (number of pages) | 109 |
| Elsevier VAT number | GB 494 6272 12 |
| Requestor Location | Zhiqiang Xie<br>1350 Bob Pettit Blvd<br>Baton Rouge, LA<br><br>BATON ROUGE, LA 70820<br>United States |

4. Permission of Using Published Material from *ACS Applied Materials & Interfaces*:

**Reproduced by permission of American Chemical Society for the following paper:**

Zhiqiang Xie, Ziyang He, Xuhui Feng, Wangwang Xu, Xiaodan Cui, Jiuhong Zhang, Cheng Yan, Moises A Carreon, Zheng Liu, and Ying Wang, "Hierarchical sandwich-like structure of ultrafine N-rich porous carbon nanospheres grown on graphene sheets as superior lithium-Ion battery anodes", ACS Appl. Mater. Interfaces, 2016, 8, 10324–10333.


**PERMISSION/LICENSE IS GRANTED FOR YOUR ORDER AT NO CHARGE**

This type of permission/license, instead of the standard Terms & Conditions, is sent to you because no fee is being charged for your order. Please note the following:

- Permission is granted for your request in both print and electronic formats, and translations.
- If figures and/or tables were requested, they may be adapted or used in part.
- Please print this page for your records and send a copy of it to your publisher/graduate school.
- Appropriate credit for the requested material should be given as follows: "Reprinted (adapted) with permission from (COMPLETE REFERENCE CITATION). Copyright (YEAR) American Chemical Society." Insert appropriate information in place of the capitalized words.
- One-time permission is granted only for the use specified in your request. No additional uses are granted (such as derivative works or other editions). For any other uses, please submit a new request.

## VITA

Zhiqiang Xie was born in Yuncheng, Shanxi, China. He received his Bachelor's degree in materials science and engineering from Kunming University of Science and Technology in China and Master's degree in materials engineering from the University of Dayton, Ohio. He became a graduate student in Mechanical Engineering department at Louisiana State University at 2014. His current research focuses on the synthesis of various nanostructured electrode materials for rechargeable lithium-ion batteries, solar cells, and environmental cleaning.